



**NAVAL  
POSTGRADUATE  
SCHOOL**

**MONTEREY, CALIFORNIA**

**THESIS**

**SIMULATING TSUNAMIS IN THE INDIAN OCEAN  
WITH REAL BATHYMETRY BY USING A HIGH-ORDER  
TRIANGULAR DISCONTINUOUS GALERKIN  
OCEANIC SHALLOW WATER MODEL**

by

Dimitrios Alevras

March 2009

Thesis Co-Advisors:

Francis X. Giraldo  
Timour Radko

**Approved for public release; distribution is unlimited**

**THIS PAGE INTENTIONALLY LEFT BLANK**

<b>REPORT DOCUMENTATION PAGE</b>			<i>Form Approved OMB No. 0704-0188</i>
Public reporting burden for this collection of information is estimated to average 1 hour per response, including the time for reviewing instruction, searching existing data sources, gathering and maintaining the data needed, and completing and reviewing the collection of information. Send comments regarding this burden estimate or any other aspect of this collection of information, including suggestions for reducing this burden, to Washington headquarters Services, Directorate for Information Operations and Reports, 1215 Jefferson Davis Highway, Suite 1204, Arlington, VA 22202-4302, and to the Office of Management and Budget, Paperwork Reduction Project (0704-0188) Washington DC 20503.			
<b>1. AGENCY USE ONLY (Leave blank)</b>	<b>2. REPORT DATE</b> March 2009	<b>3. REPORT TYPE AND DATES COVERED</b> Master's Thesis	
<b>4. TITLE AND SUBTITLE</b> Simulating Tsunamis in the Indian Ocean with Real Bathymetry by using a High-Order Triangular Discontinuous Galerkin Oceanic Shallow Water Model.		<b>5. FUNDING NUMBERS</b>	
<b>6. AUTHOR(S)</b> Lt Dimitrios Aletras, Hellenic Navy			
<b>7. PERFORMING ORGANIZATION NAME(S) AND ADDRESS(ES)</b> Naval Postgraduate School Monterey, CA 93943-5000		<b>8. PERFORMING ORGANIZATION REPORT NUMBER</b>	
<b>9. SPONSORING /MONITORING AGENCY NAME(S) AND ADDRESS(ES)</b> N/A		<b>10. SPONSORING/MONITORING AGENCY REPORT NUMBER</b>	
<b>11. SUPPLEMENTARY NOTES</b> The views expressed in this thesis are those of the author and do not reflect the official policy or position of the Department of Defense or the U.S. Government.			
<b>12a. DISTRIBUTION / AVAILABILITY STATEMENT</b> Approved for public release; distribution is unlimited.		<b>12b. DISTRIBUTION CODE</b>	
<b>13. ABSTRACT (maximum 200 words)</b>  The discontinuous Galerkin (DG) method has been accepted in the last decade by the geosciences community as an important component of geophysical fluid dynamics. The high-order accuracy, geometric flexibility to use unstructured grids, local conservation, and monotonicity properties of the DG method make it a prime candidate for the construction of future ocean and shallow water models.  This study focuses on formattting real bathymetry data of the Indian Ocean in order to simulate the propagation stage of the Indian Ocean tsunami that occurred on December 26, 2004, by using a DG model. In order to validate this simulation the study uses real measurements. The model results are compared to tide gauge data from several stations around the Indian Ocean, satellite altimetry, and field measurements. These results show that the model gives accurate estimates of arrival times in distant locations.			
<b>14. SUBJECT TERMS</b> Tsunami Simulation, Indian Ocean Tsunami 2004, Triangular Discontinuous Galerkin Method, Propagation stage, Oceanic Shallow Water Model		<b>15. NUMBER OF PAGES</b> 113	
<b>16. PRICE CODE</b>			
<b>17. SECURITY CLASSIFICATION OF REPORT</b> Unclassified	<b>18. SECURITY CLASSIFICATION OF THIS PAGE</b> Unclassified	<b>19. SECURITY CLASSIFICATION OF ABSTRACT</b> Unclassified	<b>20. LIMITATION OF ABSTRACT</b> UU

NSN 7540-01-280-5500

Standard Form 298 (Rev. 2-89)  
Prescribed by ANSI Std. Z39-18

**THIS PAGE INTENTIONALLY LEFT BLANK**

**Approved for public release; distribution is unlimited**

**SIMULATING TSUNAMIS IN THE INDIAN OCEAN WITH REAL  
BATHYMETRY BY USING A HIGH-ORDER TRIANGULAR  
DISCONTINUOUS GALERKIN OCEANIC SHALLOW WATER MODEL**

Dimitrios Alevras  
Lieutenant, Hellenic Navy  
B.A., Hellenic Naval Academy, 1994

Submitted in partial fulfillment of the  
requirements for the degree of

**MASTER OF SCIENCE IN METEOROLOGY AND PHYSICAL  
OCEANOGRAPHY**

**And**

**MASTER OF SCIENCE IN APPLIED MATHEMATICS**

from the

**NAVAL POSTGRADUATE SCHOOL  
March 2009**

Author: Dimitrios Alevras

Approved by: Francis X. Giraldo,  
Co-Advisor

Timour Radko,  
Co-Advisor

Carlos F. Borges, Chairman  
Department of Applied Mathematics

Jeffrey D. Paduan, Chairman  
Department of Oceanography

THIS PAGE INTENTIONALLY LEFT BLANK

## ABSTRACT

The discontinuous Galerkin (DG) method has been accepted in the last decade by the geosciences community as an important component of geophysical fluid dynamics. The high-order accuracy, geometric flexibility to use unstructured grids, local conservation, and monotonicity properties of the DG method make it a prime candidate for the construction of future ocean and shallow water models.

This study focuses on formatting real bathymetry data of the Indian Ocean in order to simulate the propagation stage of the Indian Ocean tsunami that occurred on December 26, 2004, by using a DG model. In order to validate this simulation the study uses real measurements. The model results are compared to tide gauge data from several stations around the Indian Ocean, satellite altimetry, and field measurements. These results show that the model gives accurate estimates of arrival times in distant locations.

THIS PAGE INTENTIONALLY LEFT BLANK

# TABLE OF CONTENTS

I.	INTRODUCTION . . . . .	1
II.	BACKGROUND . . . . .	5
	A. GOVERNING EQUATIONS . . . . .	5
	1. Shallow Water Equations . . . . .	5
	B. TRIANGULAR DISCONTINUOUS GALERKIN METHOD . .	6
	1. Basis Functions . . . . .	6
	2. Integration . . . . .	8
	3. Semi-discrete Equations . . . . .	8
	4. Matrix Form of the Semi-discrete Equations . . . . .	9
	5. Time Integrator . . . . .	11
III.	SIMULATION OF THE INDIAN OCEAN TSUNAMI . . . . .	13
	A. MODEL DESCRIPTION . . . . .	13
	1. Boundary Conditions . . . . .	13
	2. Tides / Coriolis / Viscosity . . . . .	13
	B. REAL BATHYMETRY DATA . . . . .	14
	C. TSUNAMI SOURCE MODEL . . . . .	15
	D. REAL MEASUREMENT DATA . . . . .	17
	1. Tide Gauge Records . . . . .	17
	2. Satellite Altimetry . . . . .	25
	3. Field Measurements . . . . .	27
IV.	SIMULATIONS RESULTS . . . . .	29
	A. COMPARISON TO TIDE GAUGE RECORDS . . . . .	29
	1. Tide Gauge Stations Located at the Tropical Indian Ocean and West of India Regions . . . . .	29
	2. Tide Gauge Stations Located South-southeast of India .	51
	B. COMPARISON TO SATELLITE ALTIMETRY . . . . .	72

1.	Jason 1 . . . . .	72
2.	Topex/Poseidon . . . . .	74
3.	Envisat . . . . .	76
C.	COMPARISON TO FIELD MEASUREMENTS . . . . .	78
1.	Mercator . . . . .	78
D.	SYNOPSIS . . . . .	80
<b>V.</b>	<b>CONCLUSIONS AND RECOMMENDATIONS . . . . .</b>	<b>83</b>
<b>APPENDIX A. DERIVATION OF ANALYTIC SOLUTION FOR</b>		
<b>THE MUNK PROBLEM . . . . .</b>		<b>85</b>
<b>LIST OF REFERENCES . . . . .</b>		<b>91</b>
<b>INITIAL DISTRIBUTION LIST . . . . .</b>		<b>95</b>

## LIST OF FIGURES

1.	Mesh Grid Points Provided by AWI and Indian Ocean Bathymetry . . . . .	14
2.	Initial Conditions for the Simulation of the December 26,2004, Indian Ocean tsunami [After: [17]] . . . . .	16
3.	Locations of the Tide Gauges Where the December 26, 2004, Tsunami Waves Were Recorded [After: [22, 23, 25]] . . . . .	18
4.	Time Series of the Sea Surface Elevation in Paradip - India [After: [23]]	20
5.	Results From De-tidal Procedure for Colombo - Sri Lanka Tide Gauge Records. [After: [25],[29],[30]] . . . . .	21
6.	Results From De-tidal Procedure for Hanimaadhoo - Maldives Tide Gauge Records. [After: [25],[29],[30]] . . . . .	22
7.	Results From De-tidal Procedure for Male - Maldives Tide Gauge Records. [After: [25],[29],[30]] . . . . .	22
8.	Results From De-tidal Procedure for Gan - Maldives Tide Gauge Records. [After: [25],[29],[30]] . . . . .	23
9.	Results From De-tidal Procedure for Diego Garcia - UK Tide Gauge Records. [After: [25],[29],[30]] . . . . .	23
10.	Results From De-tidal Procedure for Port Louis - Mauritius Tide Gauge Records. [After: [25],[29],[30]] . . . . .	24
11.	Results From De-tidal Procedure for Salalah - Oman Tide Gauge Records. [After: [25],[29],[30]] . . . . .	24
12.	Results From De-tidal Procedure for Pointe La Rue - Seycelles Tide Gauge Records. [After: [25],[29],[30]] . . . . .	25
13.	Satellites Crosses During the 2004 Indian Ocean Tsunami . . . . .	26
14.	The Mercator's Anchored Location . . . . .	27
15.	Male Tide Gauge Position . . . . .	30
16.	Comparison of arrival times - Male Tide Gauge vs. Model . . . . .	31

17.	Gan Tide Gauge Position . . . . .	33
18.	Comparison of arrival times - Gan Tide Gauge vs. Model . . . . .	34
19.	Diego Garcia Tide Gauge Position . . . . .	35
20.	Comparison of arrival times - Diego Garcia Tide Gauge vs. Model . . .	36
21.	Port Louis Tide Gauge Position . . . . .	37
22.	Comparison of arrival times - Port Louis Tide Gauge vs. Model . . .	38
23.	Salalah Tide Gauge Position . . . . .	40
24.	Comparison of arrival times - Salalah Tide Gauge vs. Model . . . .	41
25.	Pointe La Rue Tide Gauge Position . . . . .	42
26.	Comparison of arrival times - Pointe La Rue Tide Gauge vs. Model .	43
27.	Mormugao Tide Gauge Position . . . . .	44
28.	Comparison of arrival times - Mormugao Tide Gauge vs. Model . . . .	45
29.	Okha Tide Gauge Position . . . . .	47
30.	Comparison of arrival times - Okha Tide Gauge vs. Model . . . . .	48
31.	Time Series of the Sea Surface Elevation in Okha - India [After: [23]] .	49
32.	Paradip Tide Gauge Position . . . . .	52
33.	Comparison of arrival times - Paradip Tide Gauge vs. Model . . . .	53
34.	Model's Sea Surface Elevation Two Hours After the Earthquake . . . .	54
35.	Model's Sea Surface Elevation Three Hours After the Earthquake . . .	55
36.	Vishakhapatnam Tide Gauge Position . . . . .	57
37.	Comparison of arrival times - Vishakhapatnam Tide Gauge vs. Model .	58
38.	Chennai Tide Gauge Position . . . . .	59
39.	Comparison of arrival times - Chennai Tide Gauge vs. Model . . . .	60
40.	Tuticorin Tide Gauge Position . . . . .	62
41.	Comparison of arrival times - Tuticorin Tide Gauge vs. Model . . . .	63
42.	Kochi Tide Gauge Position . . . . .	64
43.	Comparison of arrival times - Kochi Tide Gauge vs. Model . . . . .	65
44.	Colombo Tide Gauge Position . . . . .	67

45.	Comparison of arrival times - Colombo Tide Gauge vs. Model . . . . .	68
46.	Hanimaadhoo Tide Gauge Position . . . . .	69
47.	Comparison of Arrival Times Hanimaadhoo Tide Gauge vs. Model . .	70
48.	Model's Sea Surface Elevation Two Hours After the Earthquake . . . .	72
49.	Comparison of Jason 1 vs. Model . . . . .	73
50.	Model's Sea Surface Elevation Two Hours and Five Minutes After the Earthquake . . . . .	74
51.	Comparison of Topex/Poseidon vs. Model . . . . .	75
52.	Model's Sea Surface Elevation Three Hours and Fifteen Minutes After the Earthquake . . . . .	76
53.	Comparison of Envisat vs. Model . . . . .	77
54.	Comparison of arrival times - Mercator's fishfinder vs. Model . . . .	79
55.	Energy Propagation of the Simulated Tsunami Waves . . . . .	81

THIS PAGE INTENTIONALLY LEFT BLANK

## LIST OF TABLES

I.	Coefficients for the Strong Stability Preserving - Third Order Runge-Kutta Method. . . . .	11
II.	Properties of the Used Mercator Projection . . . . .	15
III.	Points That Form the Two Fault Segments [After: [17]] . . . . .	16
IV.	Tsunami Characteristics Estimated From the Indian Tide Gauge Records [After: [22]] . . . . .	19
V.	Profiles of Sea Surface Height Obtained by Satellites During the 2004 Indian Ocean Tsunami [After: [27]] . . . . .	26
VI.	Summary of Results for Tide Gauge Stations Located at the Tropical Indian Ocean and west of India regions . . . . .	50
VII.	Summary of Results for the Tide Gauge Stations Located at the Southeast of India regions . . . . .	71

THIS PAGE INTENTIONALLY LEFT BLANK

## ACKNOWLEDGMENTS

I gratefully acknowledge the Alfred-Wegener Institute for Polar and Marine Research (tsunami modeling group) for providing the real bathymetry data of the Indian Ocean region.

I acknowledge the NOAA for providing satellite altimetry data used to compare model results. I would also like to acknowledge the University of Hawaii Sea Level Center, Honolulu, Hawaii, the Survey of India, Delhi, and the National Institute of Oceanography, Goa, India for providing the sea level records of the 2004 Indian Ocean tsunami.

I would like to thank Mike Cook from the Oceanography Department of NPS whose knowledge in MATLAB was inestimable. I acknowledge Rich Pawlowicz's MATLAB codes (m map and t tide) which I used in order to convert the longitude / latitude coordinates to cartesian and remove the tidal effect from the real sea level records.

I would like to thank my two advisors, Prof. Frank Giraldo and Prof. Timour Radko, whom without their guidance this thesis would not have been possible. I would also like to thank the Naval Postgraduate School, the Oceanography and Mathematics departments at NPS, and the Hellenic Navy.

THIS PAGE INTENTIONALLY LEFT BLANK

# I. INTRODUCTION

The 9.3 magnitude Sumatra-Andaman undersea earthquake occurred at 00:58:53 UTC (07:58:53 local Indonesian time) on December 26, 2004. This earthquake generated a megatsunami that was among the deadliest disasters in modern history, killing more than 226,000 people [1] and is known as the 2004 Indian Ocean tsunami.

The modern science triggered by this and other similar disasters aimed to predict when and where an earthquake would occur and where a tsunami might be initiated. While the accurate prediction of an earthquake itself remains a major challenge, simulating the propagation and inundation of a tsunami wave is now a distinct possibility. Knowing where the faults are through the use of real bathymetry data, numerical simulations can be used to identify the regions that are likely to be affected by tsunami waves and establish seismic criteria for issuing tsunami warnings in the case of actual tsunamis. Furthermore, by using the existing technology of monitoring seismic activity, the simulation of the generated tsunami can give sufficient warning to the regions that are in the path of the wave.

Tsunami simulation, as well as any other numerical modeling, requires the discretization of the physical space. The two major strategies used are *regular* and *unstructured* discretizations [2]. Models that are based on regular meshes and have been successfully applied to the 2004 Indian Ocean tsunami are as follows: the MOST (Method of Splitting Tsunami) propagation model by Titov and Synolakis [3, 4], which is based on a finite-difference numerical approximation to the nonlinear shallow water wave equations, and the fully nonlinear and dispersive Boussinesq model (FUNWAVE) by Watts [5]. An example of a model based on unstructured grids is the TsunAWI model by the tsunami modeling group of the Alfred-Wegener Institute [2].

The discontinuous Galerkin (DG) method, because of the high-order accuracy, geometric flexibility to use unstructured grids, local conservation, and monotonicity

properties, has been accepted in the last decade by the geosciences community as a critical component of the computational geophysical fluid dynamics and specifically, in the construction of future ocean and shallow water models [6]. Schwanenberg and Kongeter [7] first used the DG method for the planar shallow water equations followed by the works of Li and Liu [8] as well as Ainzinger and Dawson [9]. Later, Dupont and Lin [10], Eskilsson and Sherwin [11], Remacle et al. [12], and Kubatko et al. [13] constructed shallow water models on triangles using a collapsed local coordinate (modal) discontinuous Galerkin method. Giraldo et al. [14], first used the DG method for the shallow water equations on the sphere and later by construction on triangular domains [15]. Giraldo and Warburton et al. [6] also applied the method to the two-dimensional oceanic shallow water equations. Motivation for the choice to use unstructured grids is related to its ability to better represent the continental coastlines and simulate wave processes on different scales. A tsunami's motion is characterized by relatively fast speed and low amplitude in the deep ocean, and when it reaches shallow waters the speed decreases and the amplitude increases. Near the shoreline, the tsunami steepens and may break.

Giraldo and Warburton [6] DG formulation used high-order Langrange polynomials on the triangle using nodal sets up to the 15th order. By using six test cases (three of which had analytic solutions) they showed that the high-order triangular DG method exhibits exponential convergence.

According to [16] the evolution of earthquake-generated tsunamis has three distinctive stages: *generation*, *propagation*, and *run-up*. This study, as being part of a research in regards to the development of a triangular discontinuous Galerkin oceanic shallow water model, focuses on formatting real bathymetry data of the Indian Ocean in order to simulate the *propagation* stage of the Indian Ocean tsunami of December 26, 2004, by using this DG model. The initial conditions (i.e., the tsunami's generation) are taken from the reconstruction of the rupture as described in [17] and based on [18], while the run-up stage is out of the scope for this thesis. Real measure-

ments are used for the validation of this simulation. The model results are compared to tide gauge data from several stations around the Indian Ocean, satellite altimetry (Jason-1, Topex-Poseidon and Envisat data), and field measurements. These results show that the model gives accurate estimates of arrival times in distant locations.

This study is organized as follows. Chapter II describes the spatial discretization of the governing shallow water equations and the time integrator used in this model. Chapter III describes the real bathymetry data, the initial conditions used for the simulation, and the real measurement data used for comparisons. Chapter IV presents the results from the comparison and Chapter V discusses the conclusions and recommendations. Appendix A describes the derivation of the analytic solution for the Munk problem. This solution is given in order for the validation of the lateral diffusion operators in future studies.

THIS PAGE INTENTIONALLY LEFT BLANK

## II. BACKGROUND

### A. GOVERNING EQUATIONS

#### 1. Shallow Water Equations

The oceanic shallow water equations are a system of nonlinear partial differential equations which govern the motion of a viscous incompressible fluid in a shallow depth. The underlying assumption is that the depth of the fluid is small compared to the wave length of the disturbance. The Indian Ocean is not shallow since the depth is several kilometers, but the devastating tsunami on December 26, 2004, involved waves that were tens or hundreds of kilometers long, so the shallow water approximation provides a reasonable model in this situation. A tsunami is the ideal shallow water flow problem because of the barotropic motion of the water column.

The shallow water equations in conservation form are:

$$\frac{\partial \mathbf{q}}{\partial t} + \nabla \cdot \mathbf{F}(\mathbf{q}) = S(\mathbf{q}) \quad (\text{II.1})$$

where  $\mathbf{q} = (\phi, \phi \mathbf{u}^T)^T$  are the conservation variables,

$$\mathbf{F}(\mathbf{q}) = \begin{pmatrix} \phi \mathbf{u} \\ \phi \mathbf{u} \otimes \mathbf{u} + \frac{1}{2} \phi^2 \boldsymbol{\mathcal{I}}_2 - \nu \nabla (\phi \mathbf{u}) \end{pmatrix} \quad (\text{II.2})$$

is the flux tensor, and

$$S(\mathbf{q}) = - \begin{pmatrix} 0 \\ f(\mathbf{k} \times \phi \mathbf{u}) + \phi \nabla \phi^b - \frac{\boldsymbol{\tau}}{\rho} + \gamma \phi \mathbf{u} \end{pmatrix} \quad (\text{II.3})$$

is the source function where:

- the nabla operator is defined as  $\nabla = (\partial_x, \partial_y)^T$
- $\otimes$  denotes the tensor product operator
- $\phi = gh$  is the geopotential height

(where  $g$  is the gravitational constant and  $h$  is the free surface height of the fluid),

- $\phi^b$  is the bathymetry

- $\mathbf{u} = (u, v)^T$  is the velocity vector
- $f = f_0 + \beta(y - y_m)$  is the Coriolis parameter
- $k = (0, 0, 1)^T$  is the unit normal vector of the x - y plane
- the vector  $\boldsymbol{\tau}$  is the wind stress
- the constant  $\gamma$  is the bottom friction
- the term  $\mathcal{I}_2$  is the rank-2 identity matrix

## B. TRIANGULAR DISCONTINUOUS GALERKIN METHOD

This section describes the discretization of the shallow water equations by the discontinuous Galerkin method on triangles, as defined by Giraldo and Warburton [6].

### 1. Basis Functions

This method demands the decomposition of the domain  $\Omega$  into  $N_e$  non-overlapping triangular elements  $\Omega_e$  such that

$$\Omega = \bigcup_{e=1}^{N_e} \Omega_e$$

and the introduction of a nonsingular mapping  $\mathbf{x} = \Psi(\boldsymbol{\xi})$  which defines a transformation from the physical Cartesian coordinate system  $\mathbf{x} = (x, y)^T$  to the local reference coordinate system  $\boldsymbol{\xi} = (\xi, \eta)^T$ , defined on the reference triangle

$$\Omega_e = \{(\xi, \eta), -1 \leq \xi, \eta \leq 1, \xi + \eta \leq 0\}.$$

The local element-wise solution  $\mathbf{q}$  can be represented by an  $N$ th order polynomial in  $\boldsymbol{\xi}$  as

$$\mathbf{q}_N(\boldsymbol{\xi}) = \sum_{i=1}^{M_N} \psi_i(\boldsymbol{\xi}) \mathbf{q}_N(\boldsymbol{\xi}_i) \quad (\text{II.4})$$

where  $\boldsymbol{\xi}_i$  represents  $M_N = \frac{1}{2}(N+1)(N+2)$  interpolation points and  $\psi_i(\boldsymbol{\xi})$  are the associated multivariate Lagrange polynomials.

The Lagrange polynomials (nodal basis functions),  $\psi_k(\xi, \eta)$ , on the reference triangle are defined as

$$\varphi_k(\xi, \eta) = \sqrt{\frac{(2i+1)(i+j+1)}{2}} P_i^{0,0} \left( \frac{2\xi + \eta + 1}{1 - \eta} \right) \left( \frac{1 - \eta}{2} \right)^i P_j^{2i+1,0}(\eta) \quad (\text{II.5})$$

where  $P_n^{\alpha, \beta}(\xi)$  represents the nth order Jacobi polynomial in the interval  $-1 \leq \xi \leq 1$ ,  $k = i + j(N+1) + 1$ , and the indices vary as  $0 \leq i, j; i+j \leq N$ , and  $k = 1, \dots, M_N$ .

An explicit formula for the Lagrange basis is

$$\psi_i(\xi, \eta) = \sum_{k=1}^{M_N} A_{ik} \varphi_k(\xi, \eta) \quad (\text{II.6})$$

where the indices are defined as  $i, j, k = 1, \dots, M_N$ . By using the cardinal property of the Lagrange polynomials

$$\delta_{ij} = \sum_{k=1}^{M_N} A_{ik} \varphi_k(\xi_j, \eta_j),$$

where  $\delta$  is the Kronecker delta function, it can be written as

$$A_{ik} = \left( \varphi_k^{-1}(\xi_i, \eta_i) \right)^T. \quad (\text{II.7})$$

Recognizing that

$$V_{jk} = \varphi_k(\xi_j, \eta_j) \quad (\text{II.8})$$

is the generalized Vandermonde matrix and using Equations (II.6), (II.7), and (II.8), the Lagrange polynomials can be constructed as follows:

$$\psi_i(\xi, \eta) = \sum_{k=1}^{M_N} \left( V^{-1} \right)_{ik}^T \varphi_k(\xi, \eta) \quad (\text{II.9})$$

## 2. Integration

For any two functions ( $f$ ) and ( $g$ ), the 2D (area) integration  $\mathcal{I}_A$  that is required by the weak formulation of Galerkin methods is given by

$$\mathcal{I}_A [f, g] = \int_{\Omega_e} f(\mathbf{x}) g(\mathbf{x}) d\mathbf{x} = \sum_{i=1}^{M_C} w_i^e | J^e(\boldsymbol{\xi}_i) | f(\boldsymbol{\xi}_i) g(\boldsymbol{\xi}_i)$$

where  $M_C$  is a function of  $C$  which represents the order of the cubature approximation. For  $w_i$  and  $\boldsymbol{\xi}_i$  the high-order cubature rules for the triangle are used.

The DG method requires the evaluation of boundary integrals. This is the mechanism by which the fluxes across element edges are evaluated and allows the discontinuous elements to communicate. According to [6], the 1D (boundary) integration  $\mathcal{I}_B$  is given by

$$\mathcal{I}_B [f, g] = \int_{\Gamma_e} f(\mathbf{x}) g(\mathbf{x}) d\mathbf{x} = \sum_{i=0}^Q w_i^s | J^s(\boldsymbol{\xi}_i) | f(\boldsymbol{\xi}_i) g(\boldsymbol{\xi}_i)$$

where  $Q$  represents the order of the quadrature approximation. The use of  $Q = N$  gives order  $2N - 1$  accuracy.

## 3. Semi-discrete Equations

The use of the discontinuous Galerkin discretization in Equation (II.1) gives the weak form of the DG method

$$\int_{\Omega_e} \left( \frac{\partial \mathbf{q}_N}{\partial t} - \mathbf{F}_N \cdot \nabla - S_N \right) \psi_i(\mathbf{x}) d\mathbf{x} = - \int_{\Gamma_e} \psi_i(\mathbf{x}) \mathbf{n} \cdot \mathbf{F}_N^* d\mathbf{x} \quad (\text{II.10})$$

where  $F_N = F(\mathbf{q}_N)$  and  $S_N = S(\mathbf{q}_N)$  with  $\mathbf{F}$  and  $S$  given by Equations (II.2) and (II.3), respectively.

In the boundary integral of Equation (II.10)  $\mathbf{n}$  is the outward pointing unit normal vector of the element edge  $\Gamma_e$  and  $\mathbf{F}_N^*$  is the Rusanov numerical flux as given by the following equation:

$$\mathbf{F}_N^* = \frac{1}{2} \left[ \mathbf{F}_N \left( \mathbf{q}_N^L \right) + \mathbf{F}_N \left( \mathbf{q}_N^R \right) - |\lambda| \left( \mathbf{q}_N^R - \mathbf{q}_N^L \right) \mathbf{n} \right] \quad (\text{II.11})$$

where  $\lambda = \max(|U^L| + \sqrt{\phi^L}, |U^R| + \sqrt{\phi^R})$  with  $U^{L,R} = \mathbf{u}^{L,R} \cdot \mathbf{n}$  being the normal component of velocity with respect to the edge  $\Gamma_e$ , and the superscripts  $L$  and  $R$

represent the left and right sides of the element edge. The normal vector  $\mathbf{n}$  is defined as pointing outward from left to right.

Integrating Equation (II.10) by parts once more yields the *strong* form

$$\int_{\Omega_e} \psi_i(\mathbf{x}) \left( \frac{\partial \mathbf{q}_N}{\partial t} + \nabla \cdot \mathbf{F}_N - S_N \right) d\mathbf{x} = \int_{\Gamma_e} \psi_i(\mathbf{x}) \mathbf{n} \cdot (\mathbf{F}_N - \mathbf{F}_N^*) d\mathbf{x}. \quad (\text{II.12})$$

#### 4. Matrix Form of the Semi-discrete Equations

Using the polynomial approximation

$$\mathbf{q}_N = \sum_{i=1}^{M_N} \psi_i \mathbf{q}_i$$

the semi-discrete system can be written as

$$\int_{\Omega_e} \psi_i \psi_j d\mathbf{x} \frac{\partial \mathbf{q}_j}{\partial t} + \int_{\Omega_e} \psi_i \nabla \psi_j d\mathbf{x} \cdot \mathbf{F}_j - \int_{\Omega_e} \psi_i \psi_j d\mathbf{x} S_j = \int_{\Gamma_e} \psi_i \psi_j \mathbf{n} d\mathbf{x} \cdot (\mathbf{F} - \mathbf{F}^*)_j. \quad (\text{II.13})$$

Next, the elemental matrices  $M_{ij}^e$  are defined as follows:

$$M_{ij}^e = \int_{\Omega_e} \psi_i \psi_j d\mathbf{x}, \quad \mathbf{M}_{ij}^s = \int_{\Gamma_e} \psi_i \psi_j \mathbf{n} d\mathbf{x}, \quad \mathbf{D}_{ij}^e = \int_{\Omega_e} \psi_i \nabla \psi_j d\mathbf{x},$$

which makes it possible to write Equation (II.13) in the matrix form:

$$M_{ij}^e \frac{\partial \mathbf{q}_j^e}{\partial t} + (\mathbf{D}_{ij}^e)^T \mathbf{F}_j^e - M_{ij}^e S_j = (\mathbf{M}_{ij}^s)^T (\mathbf{F} - \mathbf{F}^*)_j^e \quad (\text{II.14})$$

where the superscript  $e$  denotes an element-based evaluation and  $s$  denotes a side-based (or edge-based) evaluation.

The elemental matrices can be written, in terms of the computational variables  $(\xi)$ , as follows:

$$M_{ij}^e = |J^e| \int_{\widehat{\Omega}_e} \psi_i \psi_j d\xi \equiv |J^e| M_{ij}$$

$$\mathbf{D}_{ij}^e = |J^e| \int_{\widehat{\Omega}_e} \psi_i \nabla_{\xi} \psi_j \frac{\partial \xi}{\partial \mathbf{x}} d\xi \equiv |J^e| (D_{ij}^{\xi} \xi_x^e + D_{ij}^{\eta} \eta_x^e) \mathbf{i} + |J^e| (D_{ij}^{\xi} \xi_y^e + D_{ij}^{\eta} \eta_y^e) \mathbf{j}$$

$$\mathbf{M}_{ij}^s = |J^s| \int_{\widehat{\Gamma}_e} \psi_i \psi_j \mathbf{n} d\xi \equiv |J^s| M_{ij}^s (n_x^s \mathbf{i} + n_y^s \mathbf{j})$$

where the metric terms are defined as  $|J^e| = 2\Delta^e$  and  $|J^s| = 2\Delta^s$ . The  $\Delta^e$  and  $\Delta^s$  denote the area of element  $e$  and the length of edge  $s$  respectively. Note that the gradient operator in these integrals,  $\nabla_{\xi}$ , is defined in the local reference coordinate system  $\xi$ , and  $\hat{\Omega}_e$  and  $\hat{\Gamma}_e$  denote the area and boundary domains in the computational space, namely the bounds of integration for the master element. Thus, Equation (II.14) can be written in the following way:

$$\begin{aligned} & |J^e|M_{ij}\frac{\partial \mathbf{q}_j^e}{\partial t} + |J^e|\left(D_{ij}^\xi\xi_x^e + D_{ij}^\eta\eta_x^e\right)\mathbf{f}_j^e + |J^e|\left(D_{ij}^\xi\xi_y^e + D_{ij}^\eta\eta_y^e\right)\mathbf{g}_j^e - |J^e|M_{ij}S_j^e \\ = & |J^s|M_{ij}^s\left[n_x^s(\mathbf{f}^e - \mathbf{f}^*)_j + n_y^s(\mathbf{g}^e - \mathbf{g}^*)_j\right] \end{aligned} \quad (\text{II.15})$$

where  $\mathbf{F}^e = \mathbf{f}^e\mathbf{i} + \mathbf{g}^e\mathbf{j}$ .

By dividing Equation (II.15) by  $|J^e|$  and left multiplying by  $M_{ij}^{-1}$  the following is obtained

$$\begin{aligned} & \frac{\partial \mathbf{q}_i^e}{\partial t} + \left(\widehat{D}_{ij}^\xi\xi_x^e + \widehat{D}_{ij}^\eta\eta_x^e\right)\mathbf{f}_j^e + \left(\widehat{D}_{ij}^\xi\xi_y^e + \widehat{D}_{ij}^\eta\eta_y^e\right)\mathbf{g}_j^e - S_i^e = \\ & = \frac{|J^s|}{|J^e|}\widehat{M}_{ij}^s\left[n_x^s(\mathbf{f}^e - \mathbf{f}^*)_j + n_y^s(\mathbf{g}^e - \mathbf{g}^*)_j\right], \end{aligned} \quad (\text{II.16})$$

where the matrices are defined as

$$\widehat{D}_{ij}^\xi = M_{ik}^{-1}D_{kj}^\xi, \quad \widehat{D}_{ij}^\eta = M_{ik}^{-1}D_{kj}^\eta, \quad \widehat{M}_{ij}^s = M_{ik}^{-1}M_{kj}^s \quad (\text{II.17})$$

where

$$M_{ij} = \sum_{k=1}^{M_C} w_k \psi_{ik} \psi_{jk}, \quad M_{ij}^s = \sum_{k=1}^{M_Q} w_k \psi_{ik} \psi_{jk}, \quad (\text{II.18})$$

$$D_{ij}^\xi = \sum_{k=1}^{M_C} w_k \psi_{ik} \frac{\partial \psi_{jk}}{\partial \xi}, \quad D_{ij}^\eta = \sum_{k=1}^{M_C} w_k \psi_{ik} \frac{\partial \psi_{jk}}{\partial \eta}. \quad (\text{II.19})$$

The  $M_C$  and  $M_Q$  denote the number of cubature (two-dimensional) and quadrature (one-dimensional) integration points required to achieve order  $2N - 1$  accuracy, and  $\psi_{ik}$  represents the function  $\psi$  at the  $i = 1, \dots, M_N$  interpolation points evaluated at the integration point  $k$ .

Since the mass matrix is constant (i.e., not a function of  $\boldsymbol{x}$ ) then the use of Equations (II.18) and (II.19) gives the following:

$$\widehat{M}_{ij}^s = \sum_{k=1}^{M_Q} w_k \widehat{\psi}_{ik} \psi_{jk}, \quad \widehat{D}_{ij}^\xi = \sum_{k=1}^{M_C} w_k \widehat{\psi}_{ik} \frac{\partial \psi_{jk}}{\partial \xi}, \quad \widehat{D}_{ij}^\eta = \sum_{k=1}^{M_C} w_k \widehat{\psi}_{ik} \frac{\partial \psi_{jk}}{\partial \eta}$$

where

$$\widehat{\psi}_i = M_{ik}^{-1} \psi_k$$

is the basis function premultiplied by the inverse mass matrix. Absorbing the mass matrix within the test function  $\widehat{\psi}$  completely eliminates the mass matrix from Equation (II.16) without making any approximations.

## 5. Time Integrator

In order to advance the solution in time while retaining high-order accuracy, the strong stability preserving (SSP) Runge-Kutta third-order RK3 method (see [6]) is used. The semi-discrete (in space) equations are written as follows:

$$\frac{\partial \mathbf{q}}{\partial t} = S(\mathbf{q}).$$

The SSP temporal discretization of this vector equation is

for  $k = 1, \dots, 3$  :

$$\mathbf{q}^k = \alpha_0^k \mathbf{q}^n + \alpha_1^k \mathbf{q}^{k-1} + \beta^k \Delta t S(\mathbf{q}^{k-1})$$

where  $\mathbf{q}^0 = \mathbf{q}^n$ ,  $\mathbf{q}^3 = \mathbf{q}^{n+1}$ , and the coefficients  $\alpha$  and  $\beta$  are given in Table I.

	$k=1$	$k=2$	$k=3$
$\alpha_0$	1	3/4	1/3
$\alpha_1$	0	1/4	2/3
$\beta$	1	1/4	2/3

Table I. Coefficients for the Strong Stability Preserving - Third Order Runge-Kutta Method.

THIS PAGE INTENTIONALLY LEFT BLANK

### III. SIMULATION OF THE INDIAN OCEAN TSUNAMI

#### A. MODEL DESCRIPTION

##### 1. Boundary Conditions

As was mentioned above, this thesis study focuses on the simulation of the propagation stage of the Indian Ocean tsunami while the inundation modeling is out of its scope. For this reason, the shoreline is being treated as a fixed-wall boundary. These no-flux boundary conditions are enforced at all land boundaries by virtue of the statement

$$\mathbf{n} \cdot \mathbf{u} = 0 \quad (\text{III.1})$$

which eliminates the normal component of the velocity to the no-flux boundary without altering the tangential component (also known as free slip boundary conditions). Furthermore, the points near the coastlines with depth less than 11 meters are considered to have 11 meters depth.

Since the model does not currently have inundation algorithms, it only makes sense to compare observations with the model results using arrival times and heights of the first waves. This way the model results will not be affected by the errors associated with representation of boundary conditions along the coastlines.

##### 2. Tides / Coriolis / Viscosity

This study is based on two experiments. Each experiment had ten hours of simulations with time steps of 1.5 seconds. During the simulations, tidal forcing and the Coriolis effect were not included. In the first experiment, the value of the horizontal viscosity coefficient was  $\nu = 1000$ , while in the second the value was zero. Both simulations yielded the same results. This can be explained by using scale analysis for the shallow water momentum equations, which indicates that the relation of the horizontal viscosity to the rest of the forces is  $10^{-8}$ , on the order of machine single precision.

## B. REAL BATHYMETRY DATA

For this study, real bathymetry data of the Indian Ocean was provided by the Alfred-Wegener Institute for Polar and Marine Research (tsunami modeling group). The unstructured mesh was produced with the mesh generator TRIANGLE by Jonathan Shewchuk [20]. As described in [2], the resulting meshes were smoothed to improve the overall mesh quality. The coarsest resolution of the mesh is 14 kilometers in the deep ocean, 500 meters in the coastal areas and in areas with high bathymetry gradients (canyons), and less than 100 meters in the northern tip of Sumatra. The total number of elements used was 130,445 created by 66,715 grid points. Figure 1 presents the grid points used for this simulation study and the Indian Ocean bathymetry in meters.

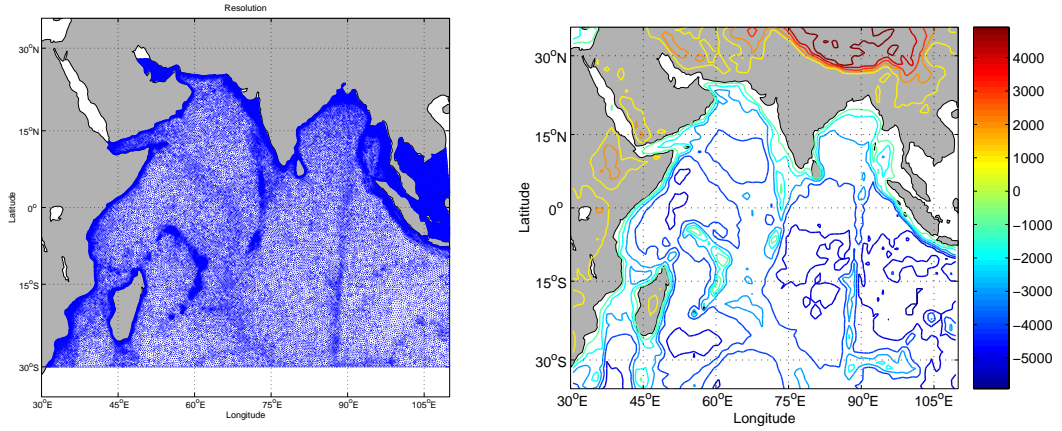


Figure 1. Mesh Grid Points Provided by AWI and Indian Ocean Bathymetry

The conversion of the above real bathymetry data from latitude/longitude coordinates into Cartesian coordinates ( $x,y$ ) was made by using the MATLAB function  $m_ll2xy$  as described in [21]. The used projection was a Mercator projection with the properties given in Table II.

<b>Min Longitude</b>	<b>Max Longitude</b>	<b>Min Latitude</b>	<b>Max Latitude</b>
$030^{\circ}E$	$110^{\circ}E$	$35^{\circ}S$	$35^{\circ}N$

Table II. Properties of the Used Mercator Projection

### C. TSUNAMI SOURCE MODEL

The main cause of tsunami waves is the abruptly motion of converging or destructive plate boundaries which vertically displace the overlying water. The Indian Ocean tsunami was generated by the static sea floor uplift caused by an abrupt slip of the India/Burma plate interface. This permanent, vertical sea floor displacement can be computed using the static dislocation formulae from [18]. Inputs for this computation are the fault plane location, its depth, strike, dip, slip, length, width, seismic moment, and rigidity. The initial conditions for the tsunami simulation were taken from the reconstruction of the rupture as described in [17]. According to this study, the fault extent constrained by observed tsunami arrival time to the northwest, east and south of the slip zone indicates a fault zone of approximately 1000 kilometers by 200 kilometers. The epicenter location lies on the southern end of the fault zone. To accommodate trench curvature, this fault plane was broken into two segments as depicted in Figure 2. The points that form these planes and used for this study are presented in Table III.

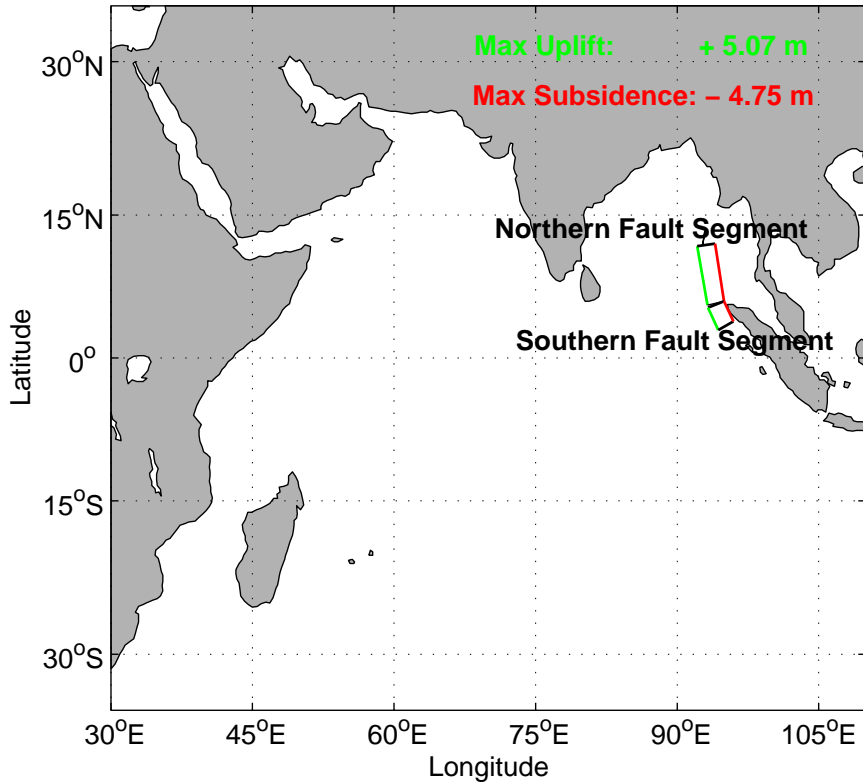


Figure 2. Initial Conditions for the Simulation of the December 26, 2004, Indian Ocean tsunami [After: [17]]

Fault Segment	Corner	Latitude	Longitude	Sea surface elevation
Northern Fault Segment	NW	11.78°N	092.12°E	+5.07 m
Northern Fault Segment	SW	5.6°N	093.22°E	+5.07 m
Northern Fault Segment	NE	12.05°N	094.02°E	-4.75 m
Northern Fault Segment	SE	6.0°N	094.97°E	-4.75 m
Southern Fault Segment	NW	5.33°N	093.25°E	+5.07 m
Southern Fault Segment	SW	2.97°N	094.35°E	+5.07 m
Southern Fault Segment	NE	6.0°N	094.97°E	-4.75 m
Southern Fault Segment	SE	3.88°N	095.97°E	-4.75 m

Table III. Points That Form the Two Fault Segments [After: [17]]

## D. REAL MEASUREMENT DATA

### 1. Tide Gauge Records

Tide gauge records are often used to provide valuable information on the tsunami **arrival times** and the **changes in sea level** due to tsunamis. After removing the tidal effect these data provide the changes in water level due to tsunamis alone.

The Indian Ocean tsunami was recorded on all the tide gauges located in the Indian Ocean. A comprehensive overview of these stations and an analysis of the tsunami records is published in [22]. For this thesis study tide gauge records from fifteen stations in the Indian Ocean were used. The locations of these stations are shown in Figure 3. In order to increase the accuracy of the results, each station's location was interpolated using the three grid points of the triangular element in which the station belongs. The tsunami characteristics of each station's records are shown in Table IV.

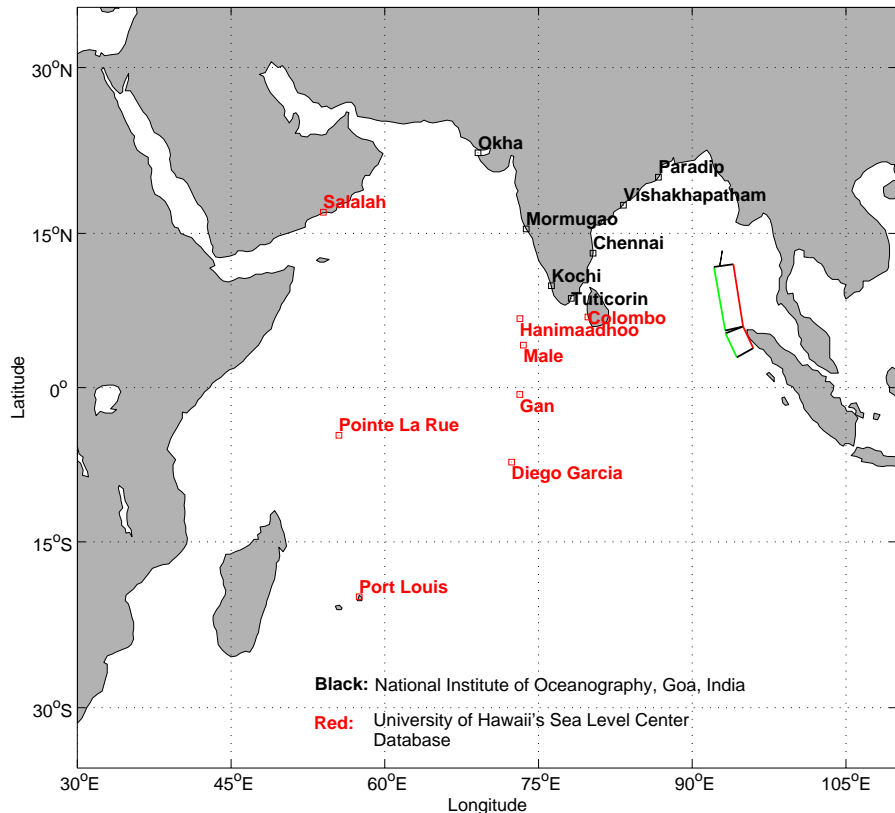


Figure 3. Locations of the Tide Gauges Where the December 26, 2004, Tsunami Waves Were Recorded [After: [22, 23, 25]]

No	Station	Coordi-nates	Sampling interval (min)	First arrival time (UTC)	wave
1	Paradip	$20.26^{\circ}N$ $086.70^{\circ}E$	6	03 : 27	2 hrs 28 min
2	Vishakhapatnam	$17.65^{\circ}N$ $083.28^{\circ}E$	5	03 : 35	2 hrs 36 min
3	Chennai	$13.10^{\circ}N$ $080.32^{\circ}E$	5	03 : 33	2 hrs 34 min
4	Tuticorin	$08.75^{\circ}N$ $078.20^{\circ}E$	6	04 : 24	3 hrs 25 min
5	Kochi (Cochin)	$09.97^{\circ}N$ $076.27^{\circ}E$	6	05 : 41	4 hrs 42 min
6	Mormugao	$15.42^{\circ}N$ $073.80^{\circ}E$	5	06 : 53	5 hrs 54 min
7	Okha	$22.50^{\circ}N$ $069.10^{\circ}E$	6	09 : 03	8 hrs 04 min
8	Colombo	$06.93^{\circ}N$ $079.83^{\circ}E$	2	03 : 49	2 hrs 50 min
9	Hanimaadhoo	$06.77^{\circ}N$ $073.18^{\circ}E$	2	04 : 30	3 hrs 31 min
10	Male	$04.18^{\circ}N$ $073.52^{\circ}E$	4	04 : 14	3 hrs 15 min
11	Gan	$00.68^{\circ}S$ $073.17^{\circ}E$	4	04 : 16	3 hrs 17 min
12	Diego Garcia	$07.30^{\circ}S$ $072.38^{\circ}E$	6	04 : 45	3 hrs 46 min
13	Port Louis	$20.15^{\circ}S$ $057.50^{\circ}E$	2	07 : 46	6 hrs 47 min
14	Salalah	$17.00^{\circ}N$ $054.00^{\circ}E$	4	08 : 08	7 hrs 09 min
15	Pointe La Rue	$04.68^{\circ}S$ $055.53^{\circ}E$	4	08 : 16	7 hrs 17 min

Table IV. Tsunami Characteristics Estimated From the Indian Tide Gauge Records  
[After: [22]]

The records of the first seven stations of Table IV (these stations are depicted with their names in black color in Figure 3) were obtained from the National Institute of Oceanography (NIO), Goa, India [23]. These tide gauges are part of the network maintained by the Survey of India (SOI) agency along the coast of India. According to [24], SOI tide gauges were either mechanical float-type analog gauges or pressure-sensor gauges. The analog records from Vishakhapatnam, Chennai, and Mormugao were digitized by SOI at an interval of 5 minutes, while those from Okha at an interval of 6 minutes. The pressure-sensor gauges from Paradip, Tuticorin, and Kochi had sampling intervals of 6 minutes. All these are high-quality, de-tided records. Some extensive gaps in the data were due to instruments and transmission problems. A typical example of these records is presented in Figure 4.

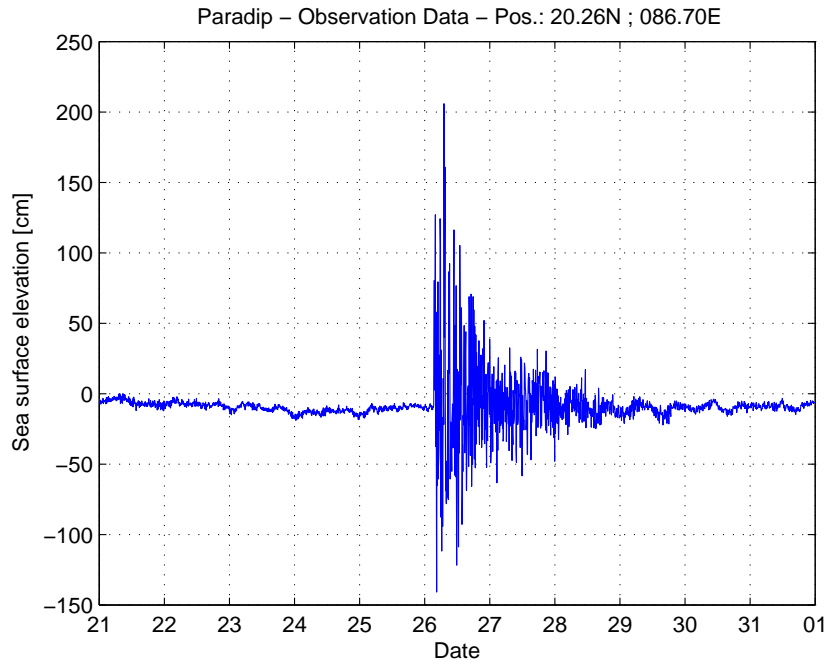


Figure 4. Time Series of the Sea Surface Elevation in Paradip - India [After: [23]]

The records of the next eight stations of Table IV (these stations are depicted with their names in red color in Figure 3) were obtained from the University of Hawaii's Sea Level Center database (Honolulu) [25]. These are digital Global Sea Level Observing System (GLOSS) stations with 2 minutes sampling intervals for Colombo, Hanimaadhoo, and Port Louis; 4 minutes for Male, Gan, Salalah, and Pointe La Rue; and 6 minutes for Diego Garcia. Most of these stations are located on isolated islands and therefore the records were not significantly affected by reflections [22]. These records were real-time sea level measurements (that included tides) and were de-tided by using the *t\_tide* program as described in [29] and [30]. Two problems during this procedure were the extensive gaps in the data due to instruments and transmission problems and the limited total record time (only one week). The results are presented in Figures 5 through 12. In all the above cases, except for Diego Garcia, the tidal effect was significantly reduced.

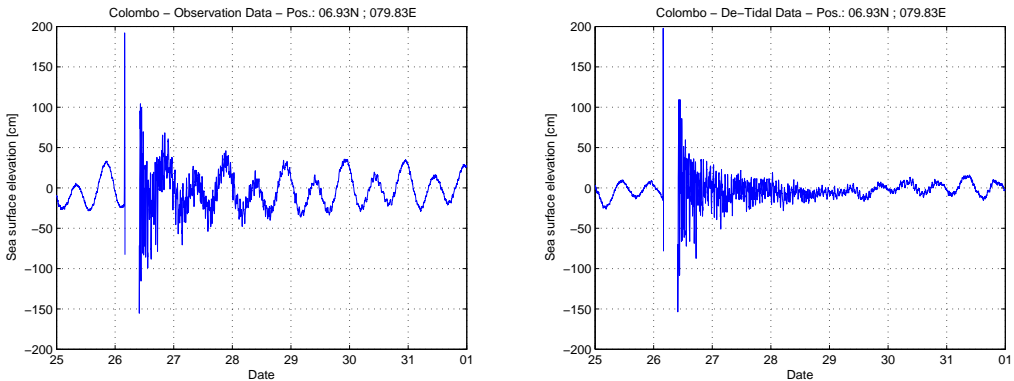


Figure 5. Results From De-tidal Procedure for Colombo - Sri Lanka Tide Gauge Records. [After: [25],[29],[30]]

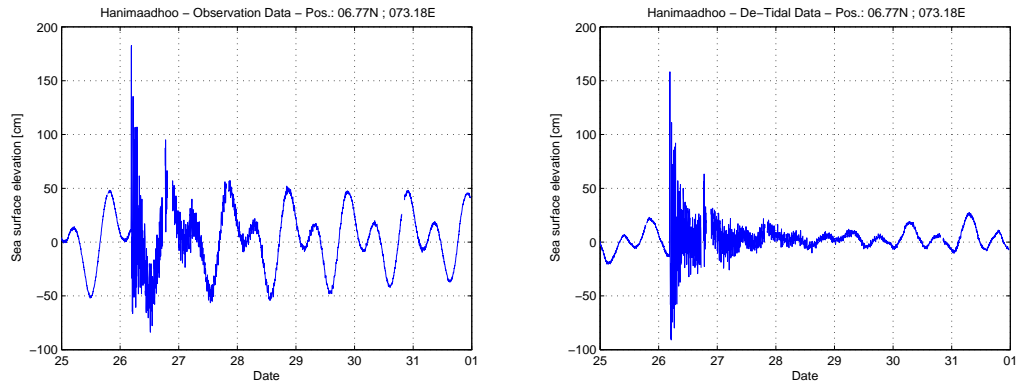


Figure 6. Results From De-tidal Procedure for Hanimaadhoo - Maldives Tide Gauge Records. [After: [25],[29],[30]]

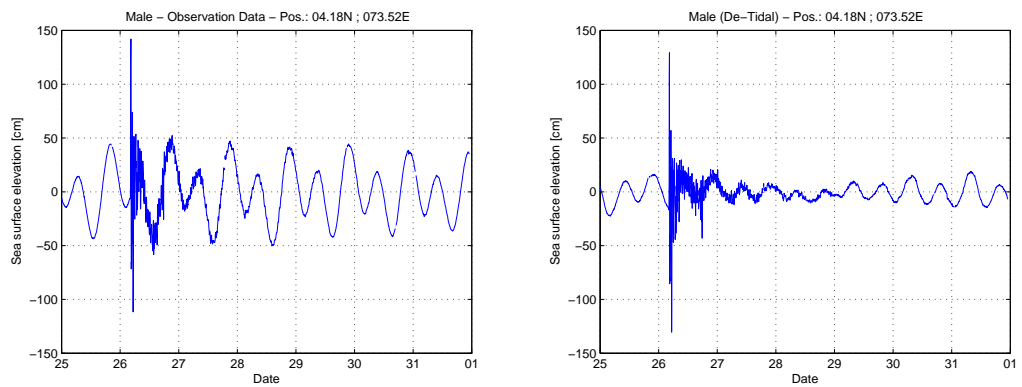


Figure 7. Results From De-tidal Procedure for Male - Maldives Tide Gauge Records. [After: [25],[29],[30]]

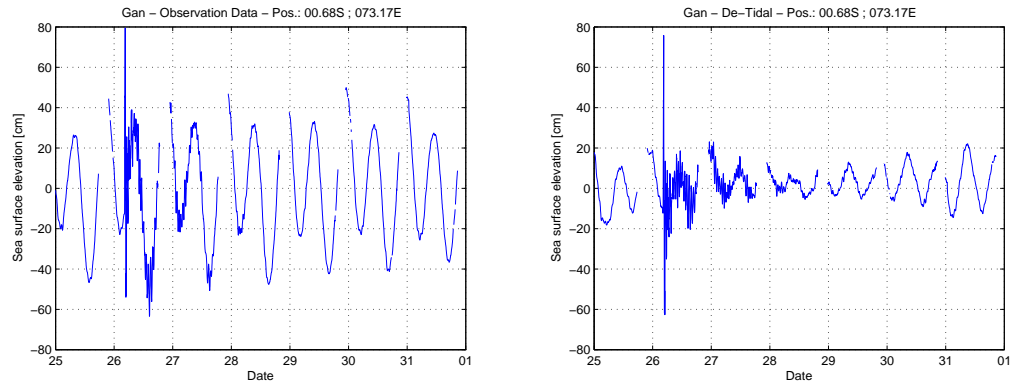


Figure 8. Results From De-tidal Procedure for Gan - Maldives Tide Gauge Records.  
[After: [25],[29],[30]]

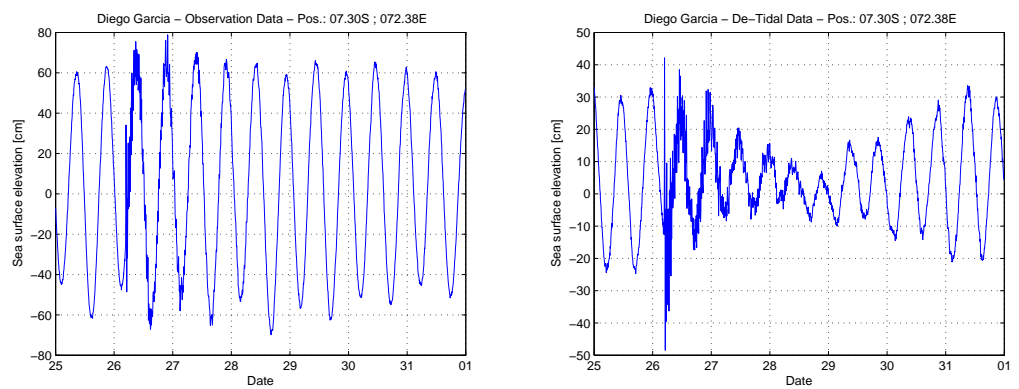


Figure 9. Results From De-tidal Procedure for Diego Garcia - UK Tide Gauge Records. [After: [25],[29],[30]]

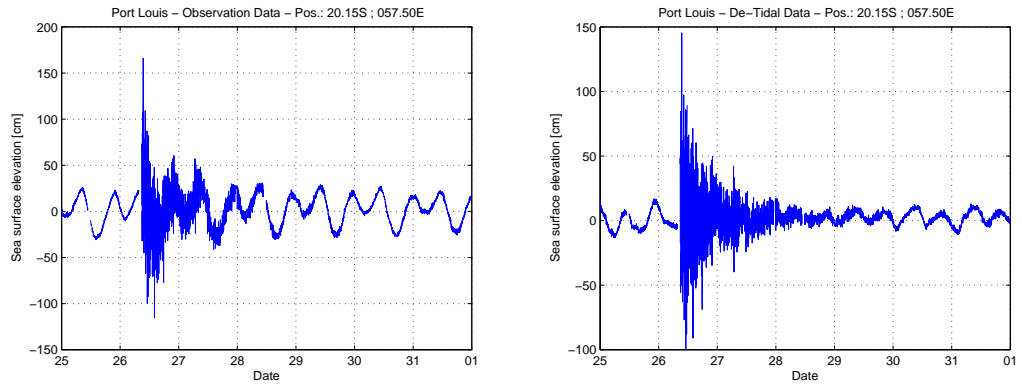


Figure 10. Results From De-tidal Procedure for Port Louis - Mauritius Tide Gauge Records. [After: [25],[29],[30]]

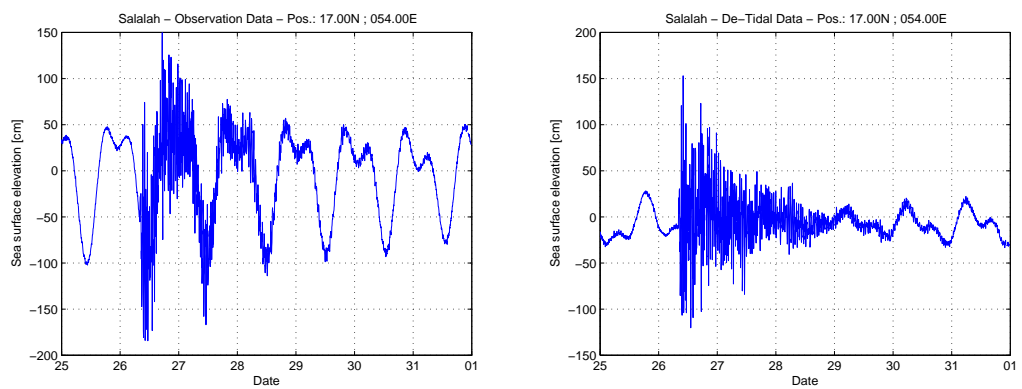


Figure 11. Results From De-tidal Procedure for Salalah - Oman Tide Gauge Records. [After: [25],[29],[30]]

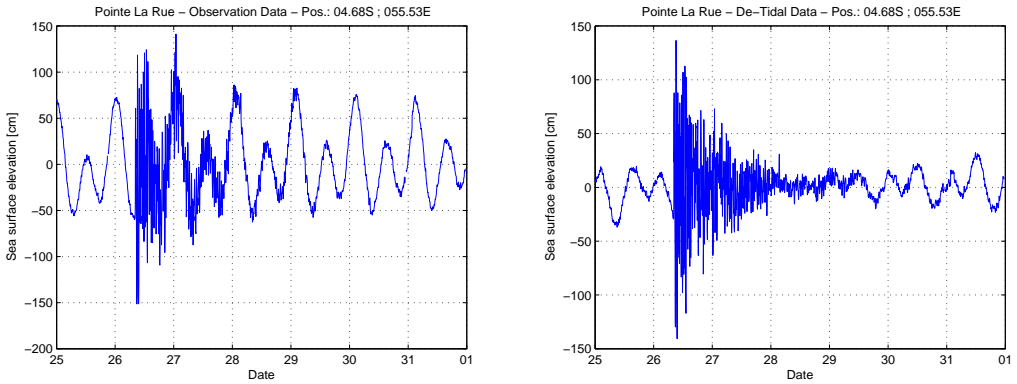


Figure 12. Results From De-tidal Procedure for Pointe La Rue - Seycelles Tide Gauge Records. [After: [25],[29],[30]]

## 2. Satellite Altimetry

Radar altimeters on board the Jason-1, TOPEX/Poseidon, and Envisat satellites obtained profiles of sea surface height on trajectories across the Indian Ocean between two and four hours after the Sumatra earthquake on December 26, 2004.

Jason-1 crossed the equator at 2:55 UTC, approximately two hours after the earthquake [26]. The data were received hours to days after "real time" so it was too late to detect and warn about the upcoming tsunami, but it can be used to validate new models. The data used for this study were obtained from NOAA [27] and originated from the satellite crossings of Figure 13 and Table V.

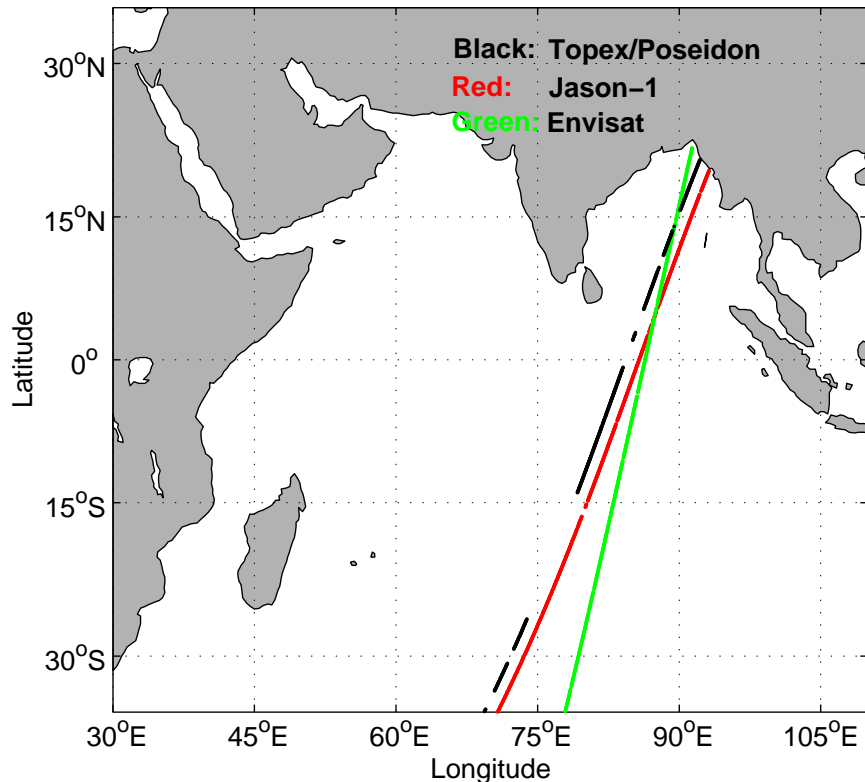


Figure 13. Satellites Crosses During the 2004 Indian Ocean Tsunami

No	Satellite	Time after the Earthquake	Color in Figure 13
1	<i>Jason1</i>	02 hrs 00 min	Red
2	TOPEX / Poseidon	02 hrs 05 min	Black
3	Envisat	03 hrs 15 min	Green

Table V. Profiles of Sea Surface Height Obtained by Satellites During the 2004 Indian Ocean Tsunami [After: [27]]

### 3. Field Measurements

During the Indian Ocean tsunami a Belgian yacht, the Mercator, was anchored about 1.6 kilometers off the Phuket coast (Thailand) at  $07.715^{\circ}N$ ,  $098.28^{\circ}E$  (Figure 14). The yacht's depth gauge was operational and measured changing wave heights during the tsunami [28]. Based on these measurements, the three main tsunami waves had trough-to-crest wave heights of 6.6, 2.2 and 5.5 meters. The first wave (trough) struck the yacht's location at 02:38 UTC (1 hour and 39 minutes).

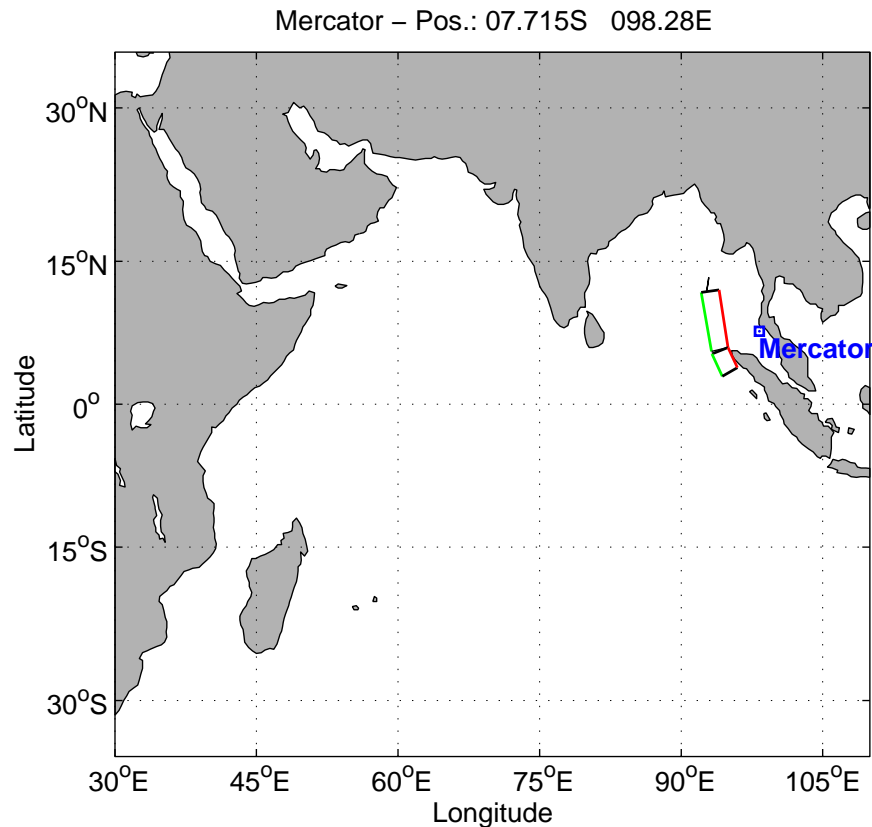


Figure 14. The Mercator's Anchored Location

THIS PAGE INTENTIONALLY LEFT BLANK

## IV. SIMULATIONS RESULTS

### A. COMPARISON TO TIDE GAUGE RECORDS

The simulation results are separated into the following two groups. The first group represents simulations of sea surface height measurements at the tropical Indian Ocean (Male, Gan, Diego Garcia, Port Louis, and Pointe La Rue), Oman (Salalah) and west India tide gauge stations (Okha and Mormugao). The second group represents simulations of sea surface height measurements at the east Indian tide gauge stations (Paradip, Vishakhapatnam, Chennai, Tuticorin, Kochi, and Colombo) as well as at Hanimaadhoo (Maldives).

#### 1. Tide Gauge Stations Located at the Tropical Indian Ocean and West of India Regions

All these stations, because of their position, were directly affected by the tsunami waves emanating from the source area.

##### a. *Male Station (Maldives)*

This station was located at  $04.18^{\circ}N, 073.52^{\circ}E$  and was approximately 1,180 nautical miles from the west side of the north fault segment (Figure 15). The GLOSS tide gauge of this station was sampled in 4 minutes intervals.

Figure 16 illustrates the agreement between the tide gauge record and the model results about the arrival time (3 hours and 15 minutes after the earthquake) and the sign (positive - wave crest) of the first wave. There is a difference (100 instead of 125 centimeters) on its maximum amplitude.

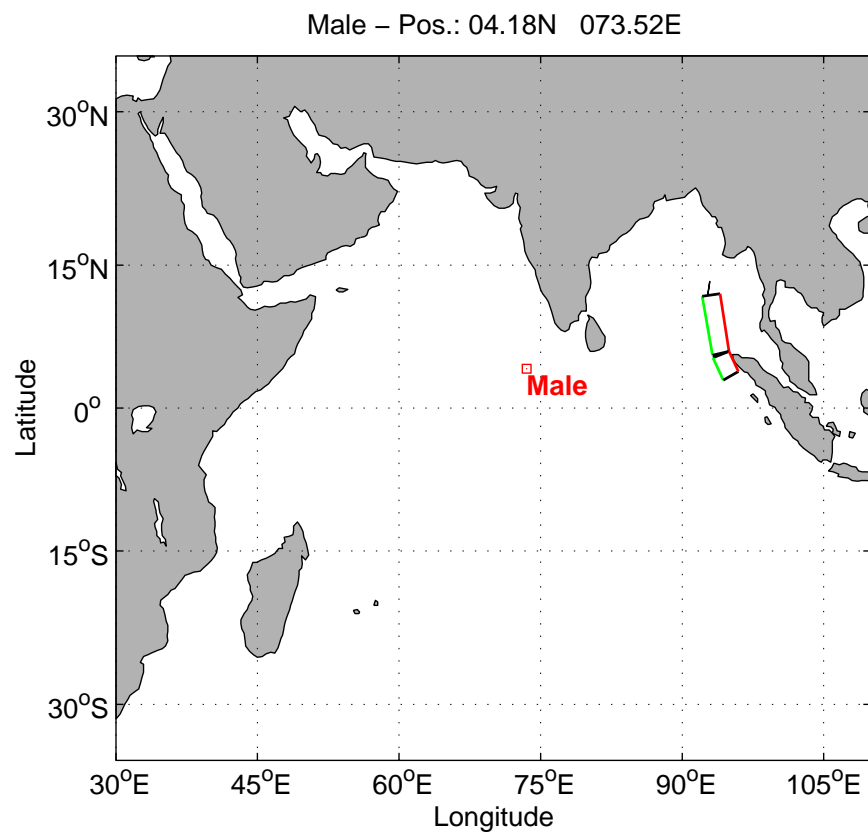


Figure 15. Male Tide Gauge Position

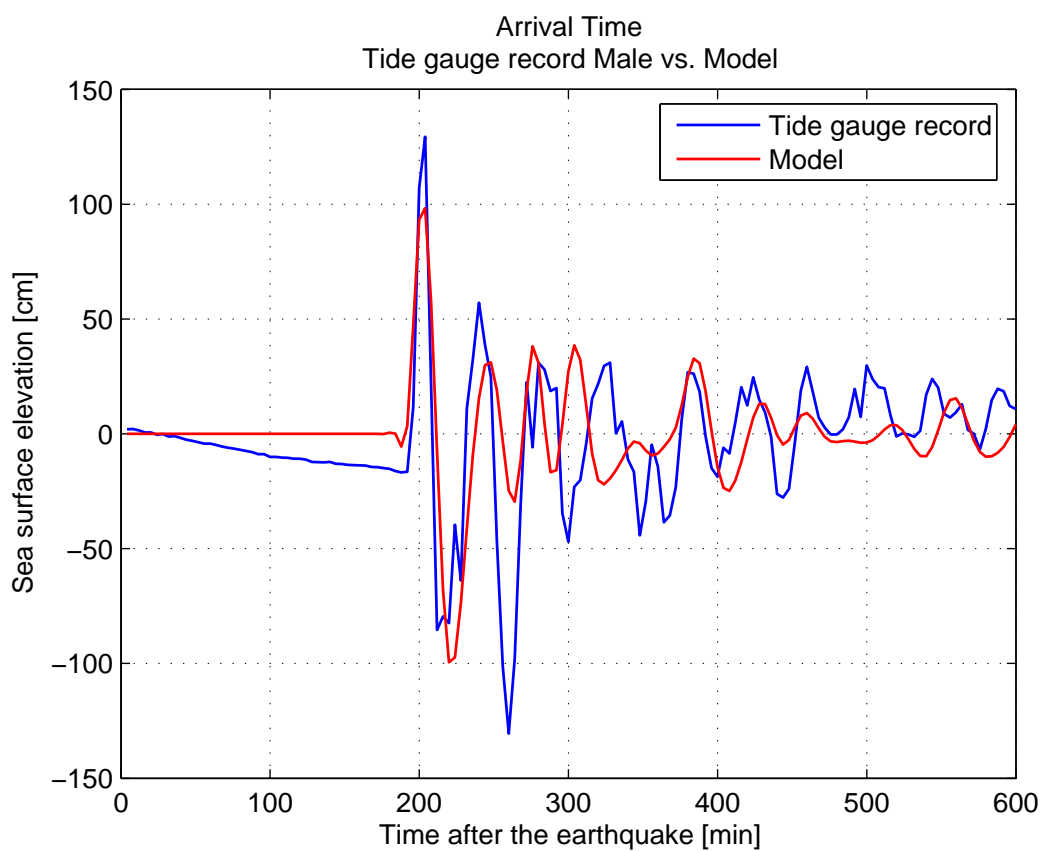


Figure 16. Comparison of arrival times - Male Tide Gauge vs. Model

*b. Gan Station (Maldives)*

This station was located at  $00.68^{\circ}S$ ,  $073.17^{\circ}E$  and was approximately 1,260 nautical miles from the west side of the south fault segment (Figure 17). The GLOSS tide gauge of this station was sampled in 4 minutes intervals.

From Figure 18 it is obvious that the model correctly predicts the arrival time (3 hours and 17 minutes after the earthquake), the sign (positive - wave crest), and almost the amplitude of the first wave (60 instead of 75 centimeters).

*c. Diego Garcia Station (UK)*

This station was located at  $07.30^{\circ}S$ ,  $072.38^{\circ}E$  and was approximately 1,460 nautical miles from the west side of the south fault segment (Figure 19). The GLOSS tide gauge of this station was sampled in 6 minutes intervals.

Figure 20 documents the agreement between the tide gauge record and the model results about the arrival time (3 hours and 46 minutes after the earthquake) and the sign (positive - wave crest) of the first wave, although there is a small difference (35 instead of 42 centimeters) on its maximum amplitude.

*d. Port Louis Station (Mauritius)*

This station was located at  $20.15^{\circ}S$ ,  $057.50^{\circ}E$  and was approximately 2,600 nautical miles from the west side of the south fault segment (Figure 21). The GLOSS tide gauge of this station was sampled in 2 minutes intervals, ceased to operate for 1 hour [22], and the sign of the first wave was unknown.

Figure 22 depicts the agreement between the tide gauge record and the model on the arrival time (6 hours and 47 minutes after the earthquake) of the first wave. According to the model, the first wave was positive (wave crest).

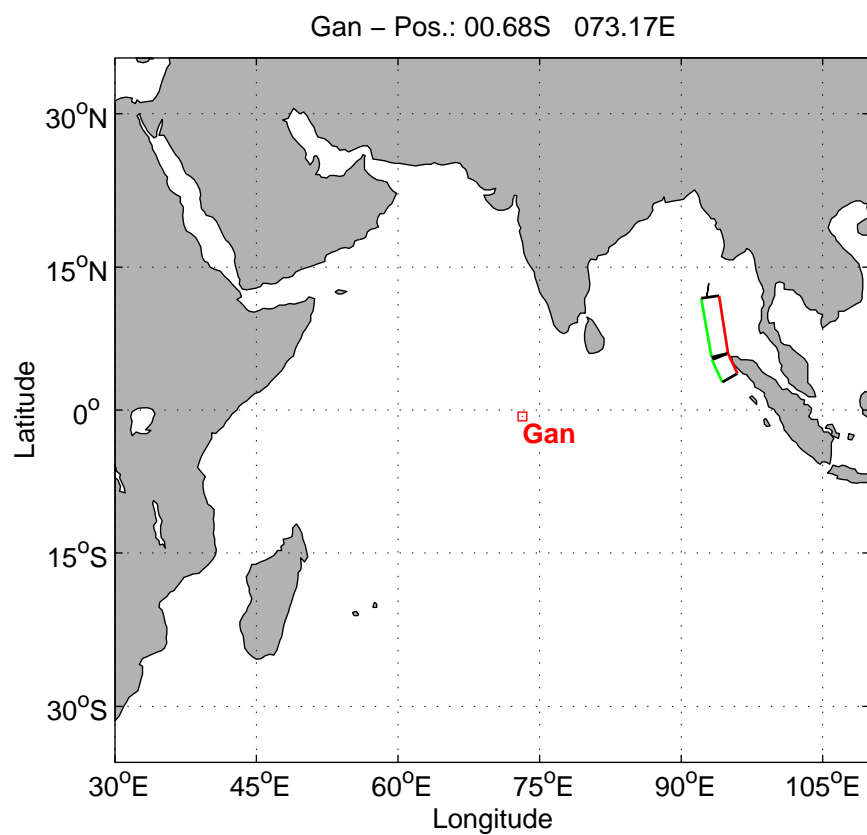


Figure 17. Gan Tide Gauge Position

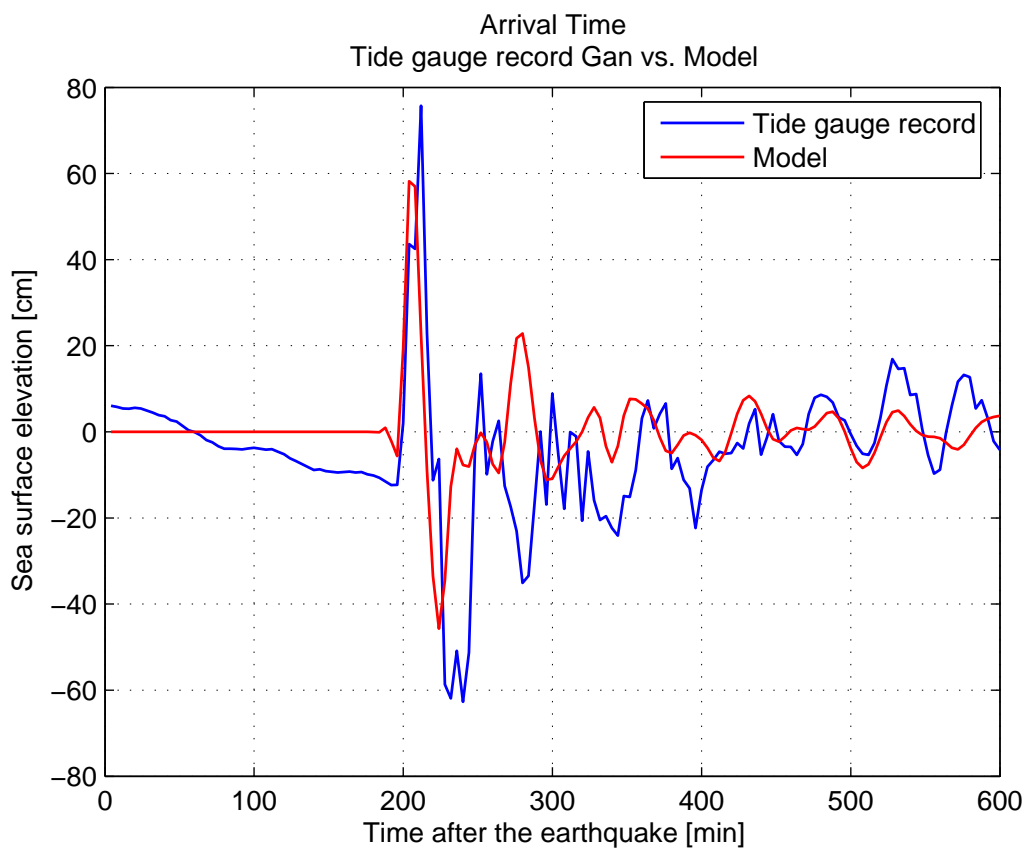


Figure 18. Comparison of arrival times - Gan Tide Gauge vs. Model

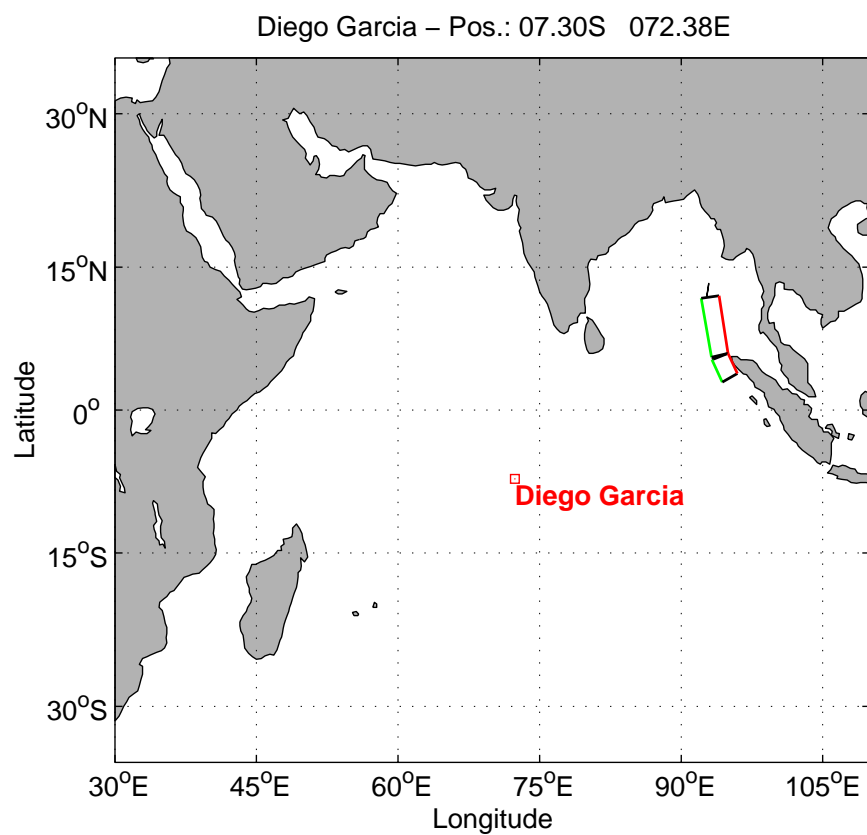


Figure 19. Diego Garcia Tide Gauge Position

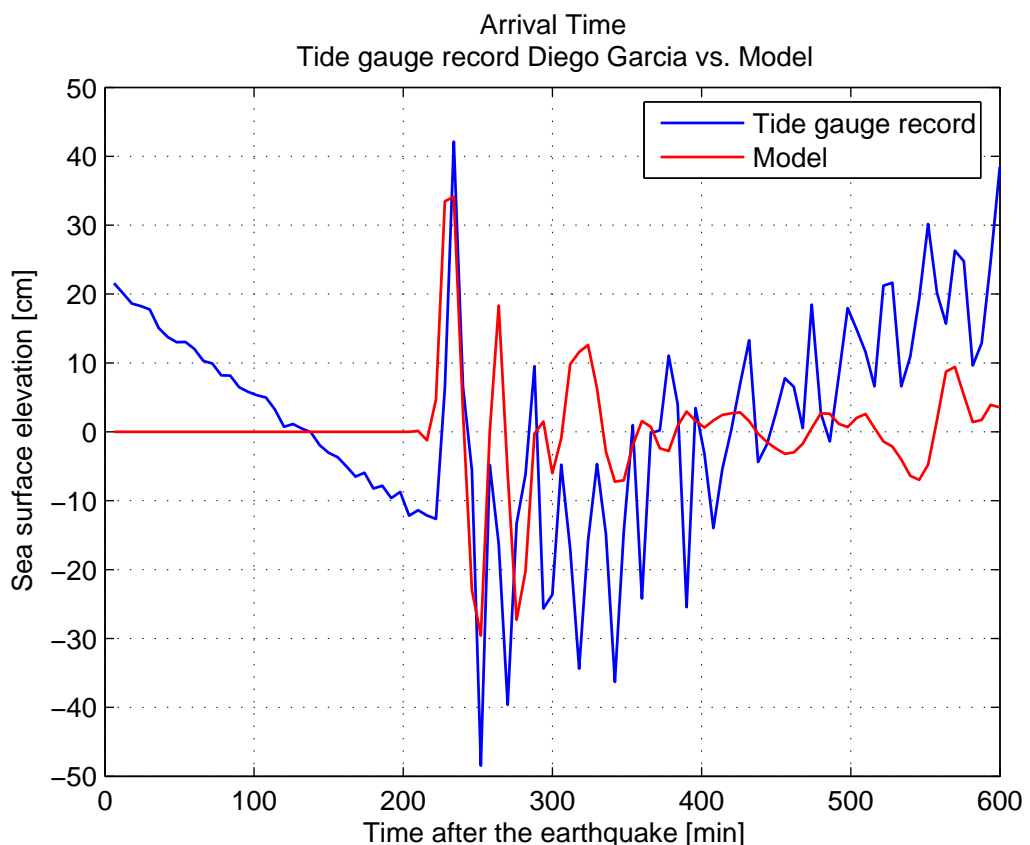


Figure 20. Comparison of arrival times - Diego Garcia Tide Gauge vs. Model

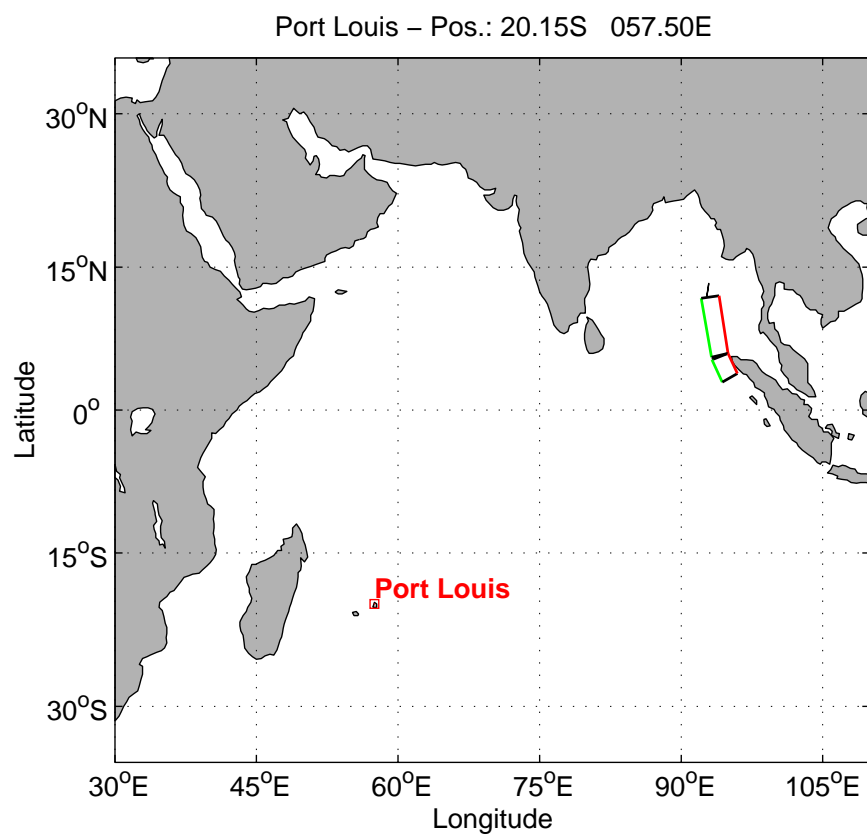


Figure 21. Port Louis Tide Gauge Position

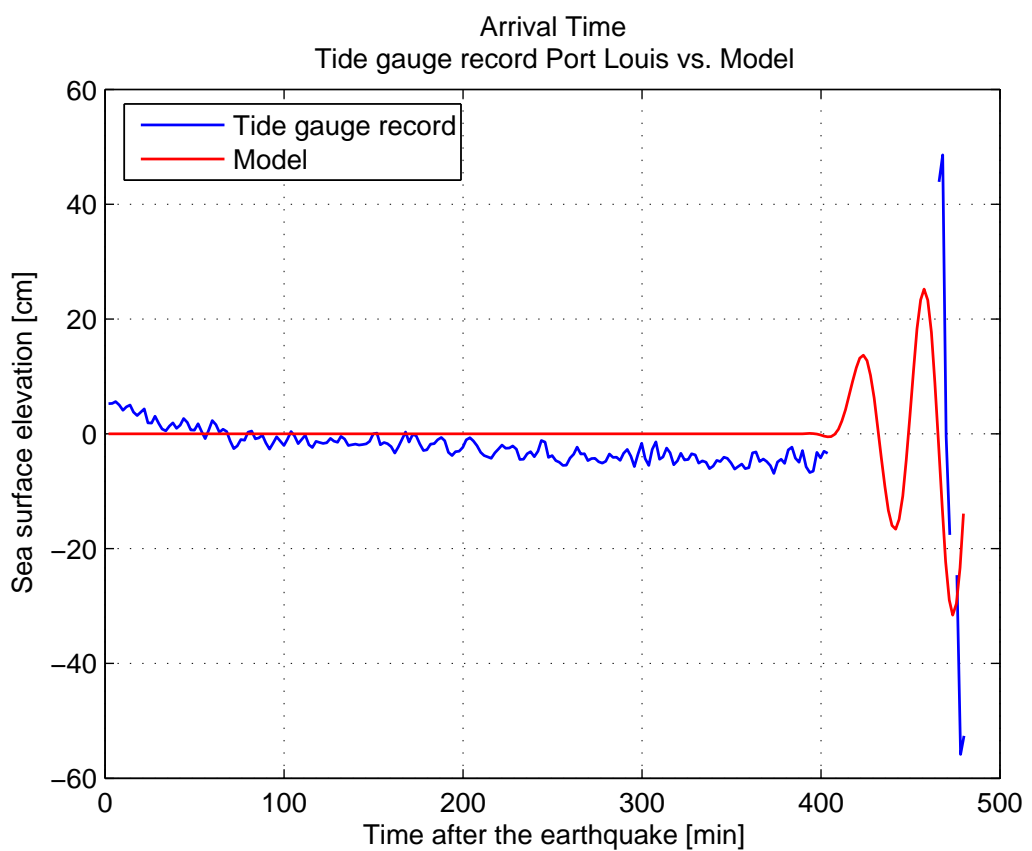


Figure 22. Comparison of arrival times - Port Louis Tide Gauge vs. Model

*e. Salalah Station (Oman)*

This station was located at  $17.00^{\circ}N, 054.00^{\circ}E$  and was approximately 2,550 nautical miles from the west side of the north fault segment (Figure 23). The GLOSS tide gauge of this station was sampled in 4 minutes intervals.

Figure 24 depicts the general agreement between the tide gauge records and the model.

*f. Pointe La Rue Station (Seychelles)*

This station was located at  $04.68^{\circ}S, 055.53^{\circ}E$  and was approximately 2,350 nautical miles from the west side of the south fault segment (Figure 25). The GLOSS tide gauge of this station was sampled in 4 minutes intervals.

From Figure 26 it is obvious that the model correctly predicts the arrival time (7 hours and 04 minutes after the earthquake), the sign (positive - wave crest), and nearly the amplitude of the first wave (50 instead of 80 centimeters).

*g. Mormugao Station (India)*

This station was located at  $15.42^{\circ}N - 073.80^{\circ}E$  and was approximately 1,300 nautical miles from the west side of the north fault segment (Figure 27). The GLOSS tide gauge of this station was sampled in 5 minutes intervals.

Figure 28 depicts the agreement on the arrival time (5 hours and 54 min after the earthquake) and the sign (positive - wave crest) of the first wave between the tide gauge record and the model. Also, the maximum amplitude of the first arrival wave (almost 55 centimeters) was accurately predicted.

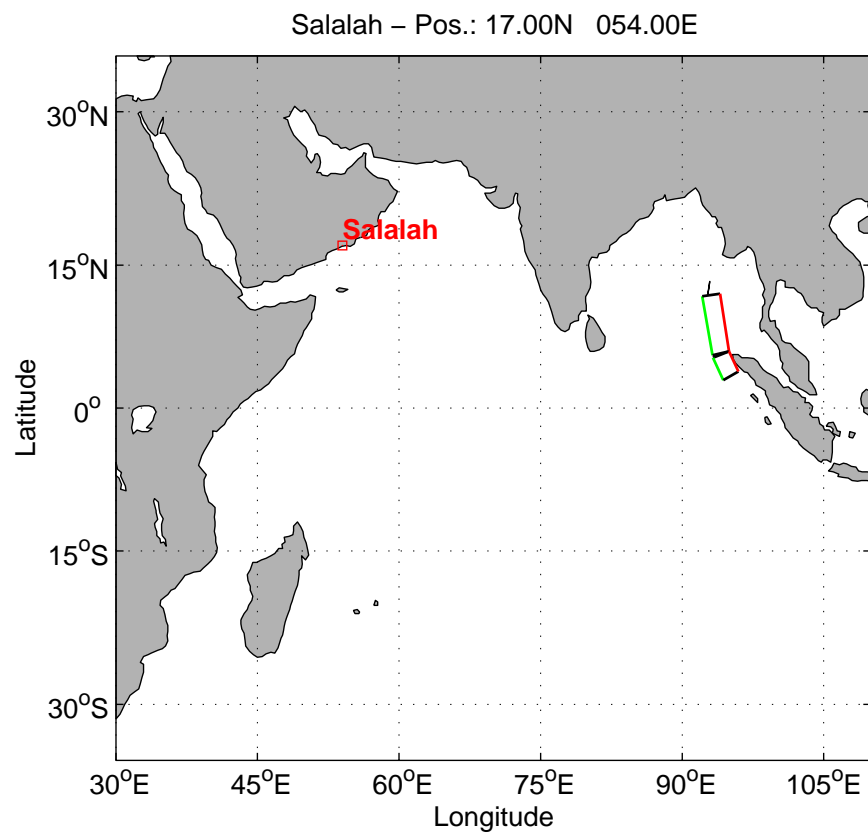


Figure 23. Salalah Tide Gauge Position

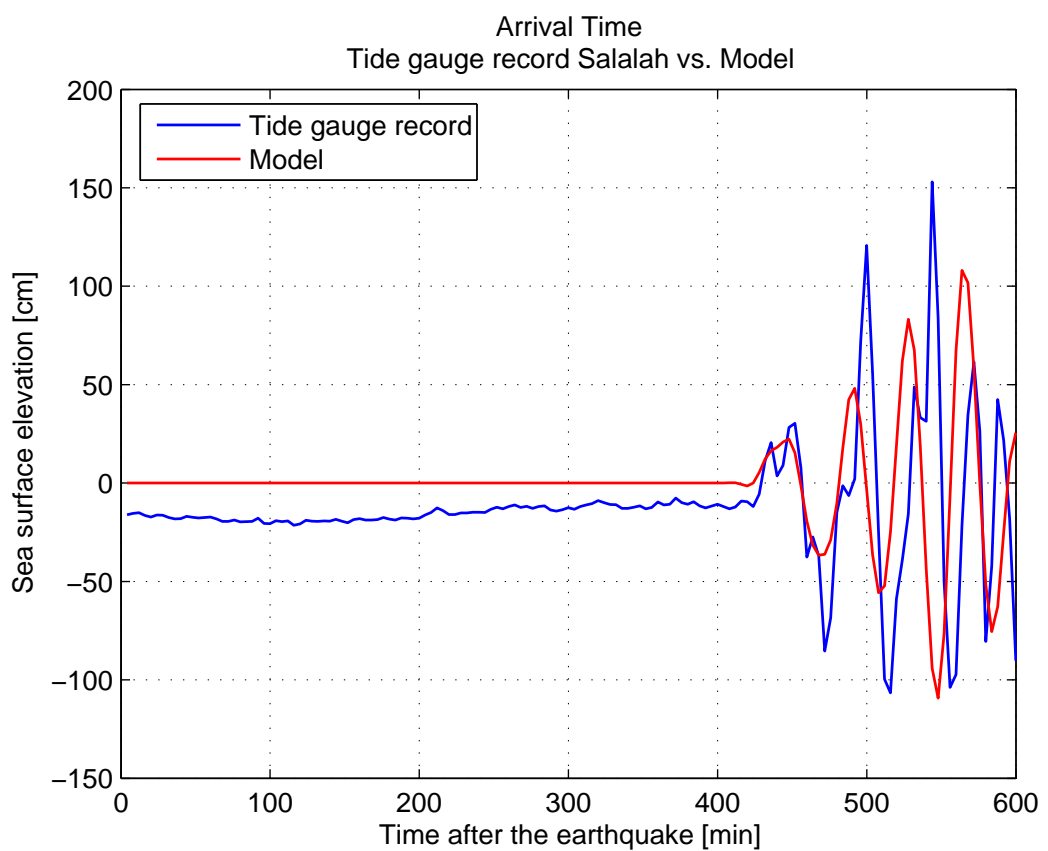


Figure 24. Comparison of arrival times - Salalah Tide Gauge vs. Model

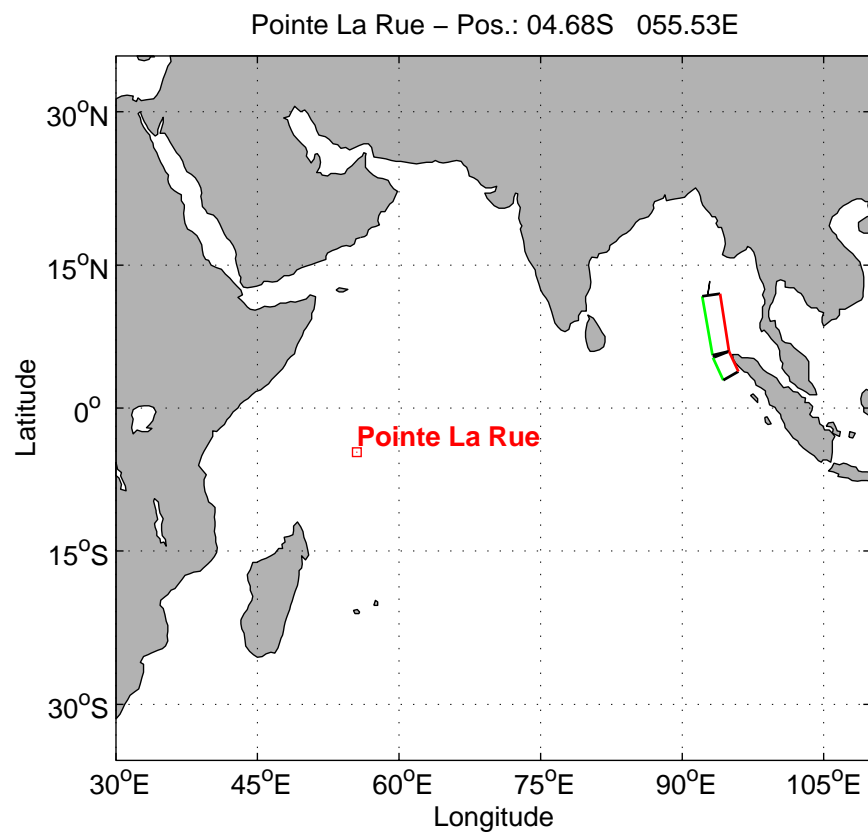


Figure 25. Pointe La Rue Tide Gauge Position

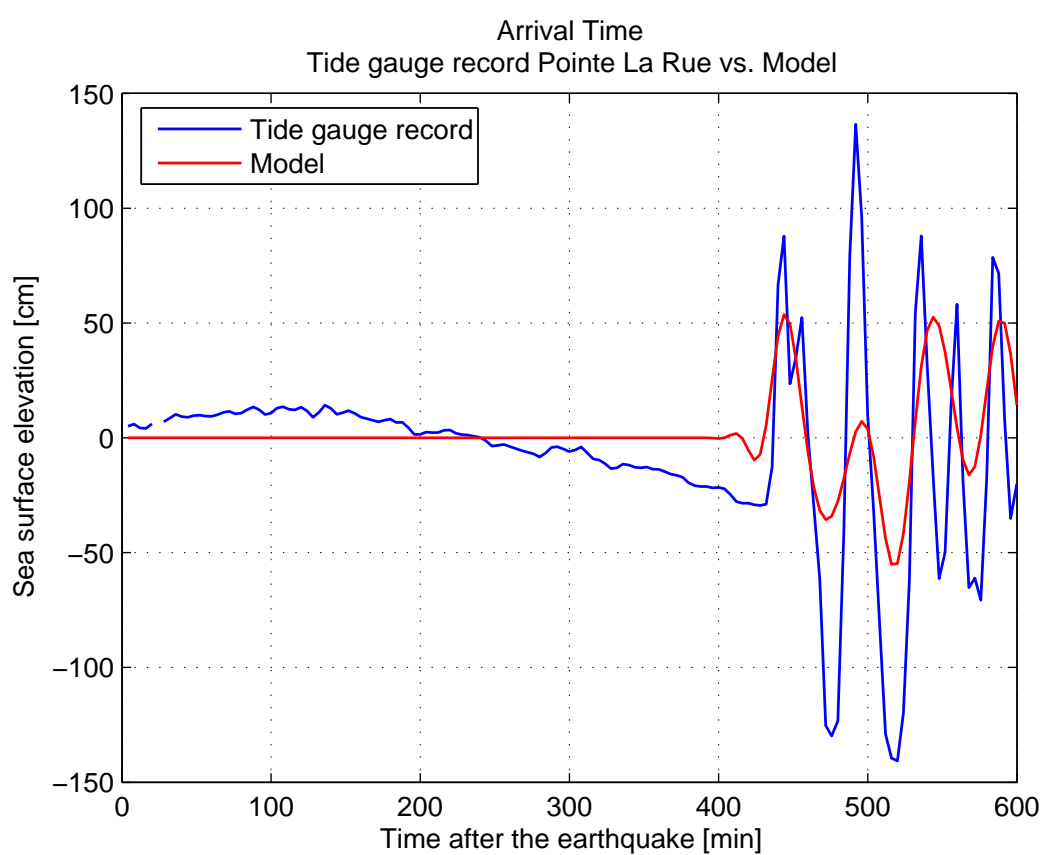


Figure 26. Comparison of arrival times - Pointe La Rue Tide Gauge vs. Model

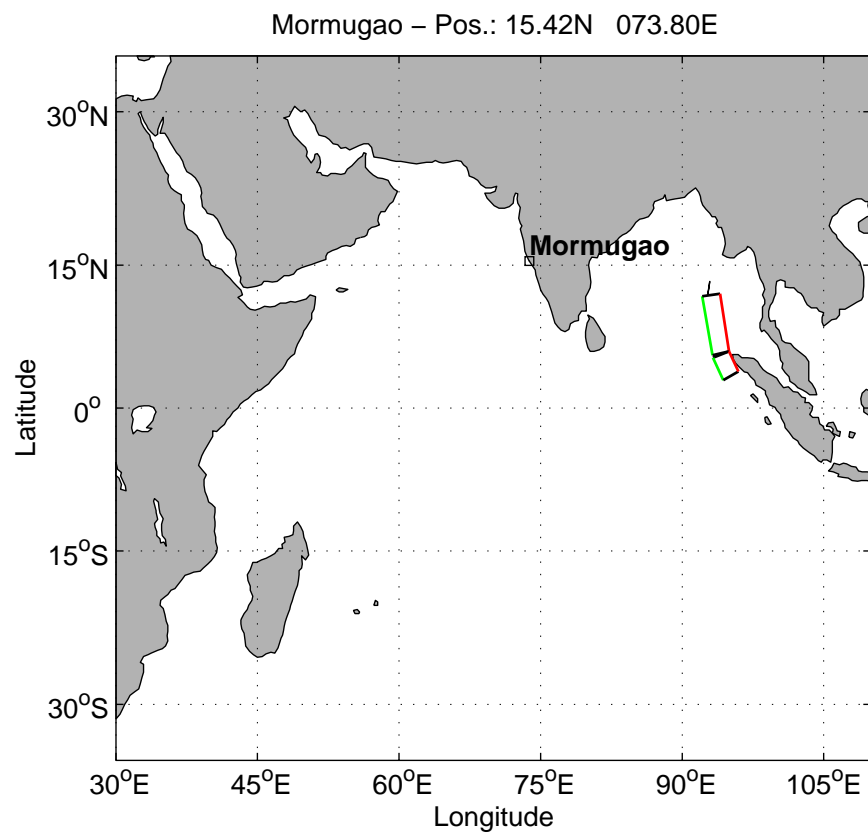


Figure 27. Mormugao Tide Gauge Position

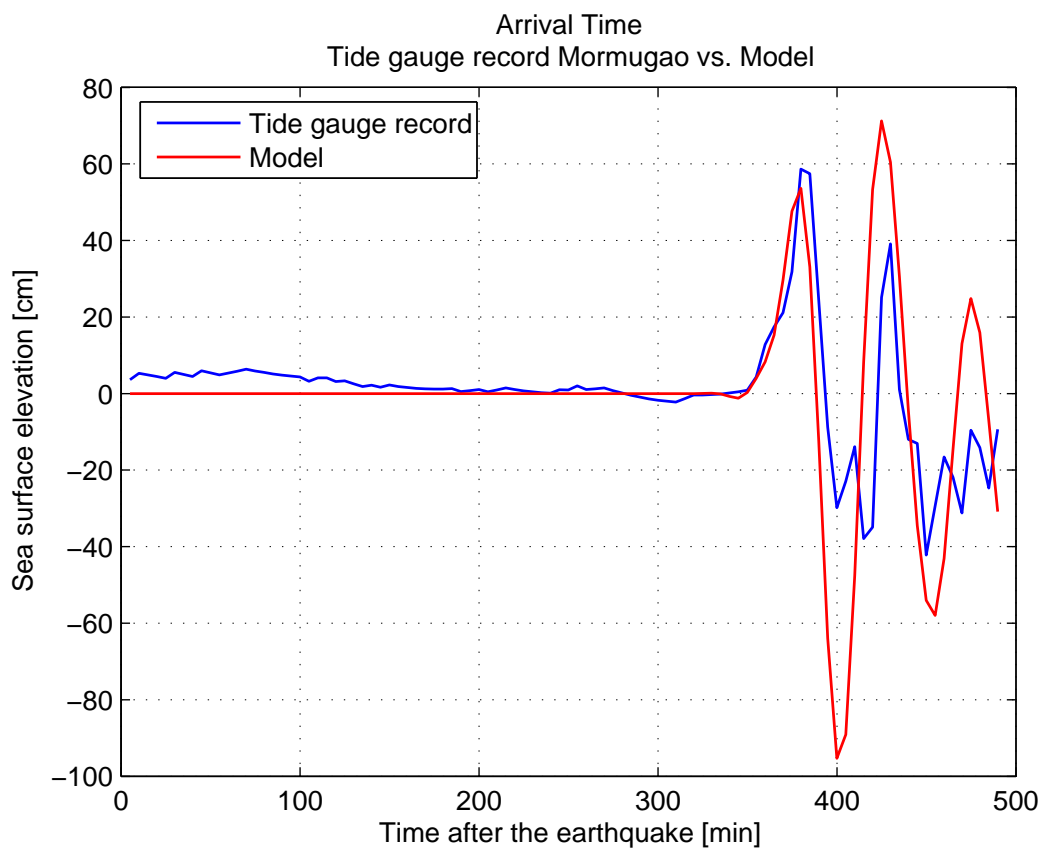


Figure 28. Comparison of arrival times - Mormugao Tide Gauge vs. Model

*h. Okha Station (India)*

This station was located at  $22.50^{\circ}N, 069.10^{\circ}E$  and was approximately 1,900 nautical miles from the west side of the north fault segment (Figure 29). The GLOSS tide gauge of this station was sampled in 6 minutes intervals.

The negative values of the observations in Figure 30 can be attributed to the tidal effect, which was not completely removed (see Figure 31). Taking into account this deficiency of data, the model correctly predicts the sign (positive - wave crest), arrival time (8 hours and 04 minutes) and amplitude of the first wave (8 centimeters).

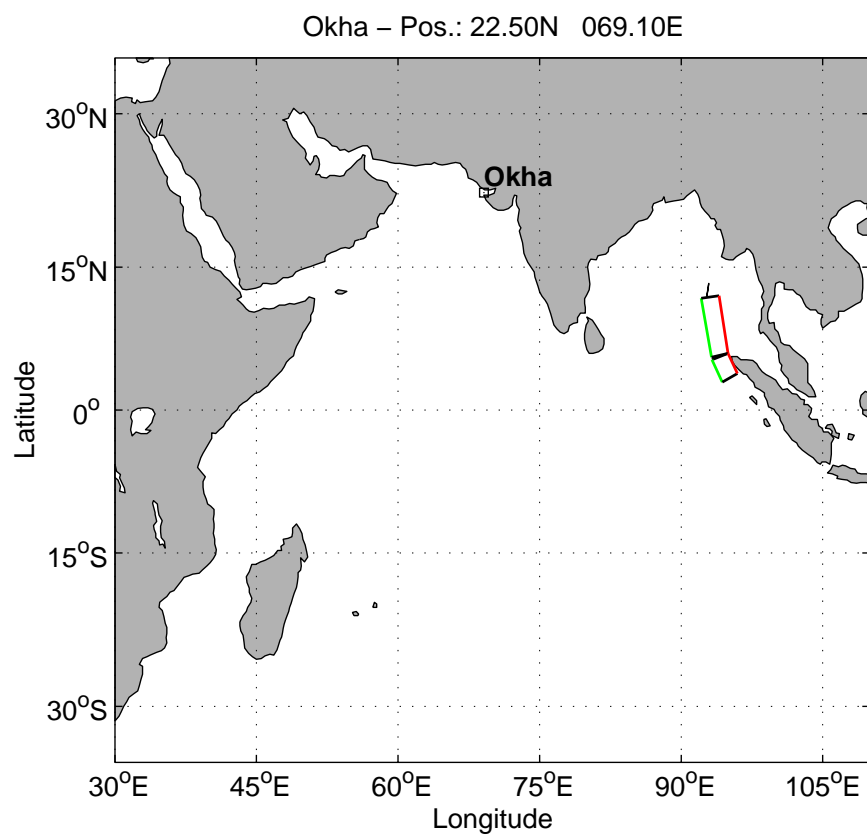


Figure 29. Okha Tide Gauge Position

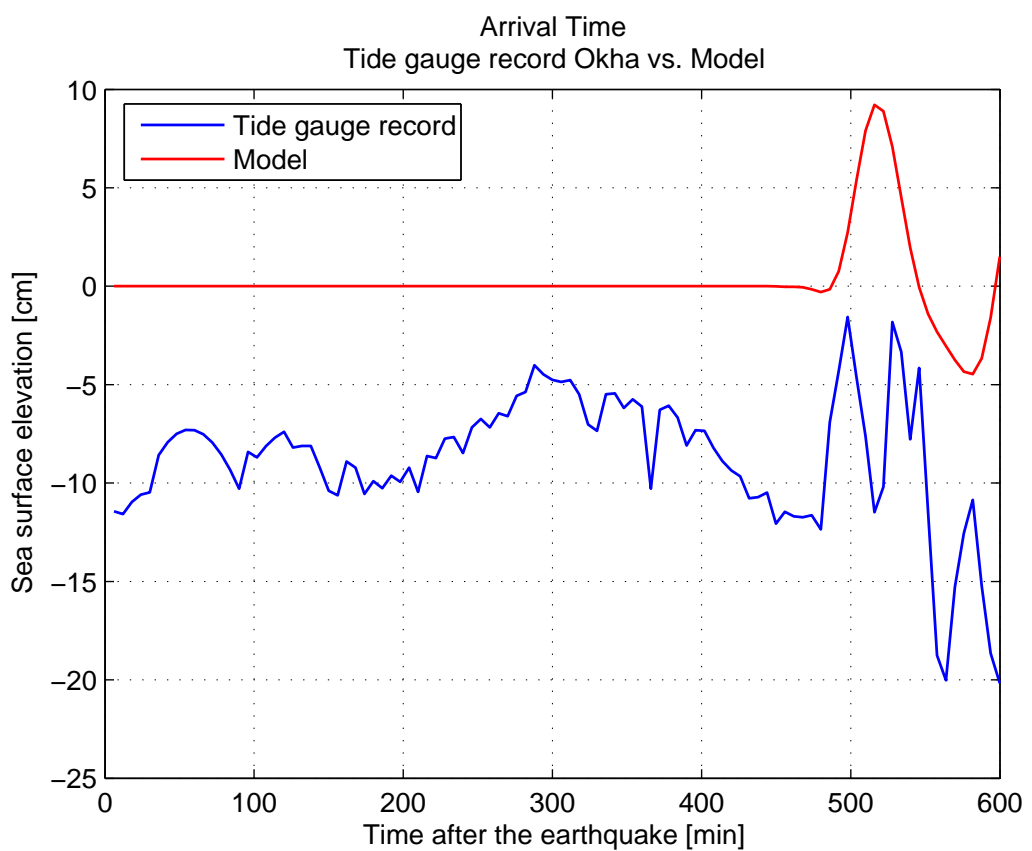


Figure 30. Comparison of arrival times - Okha Tide Gauge vs. Model

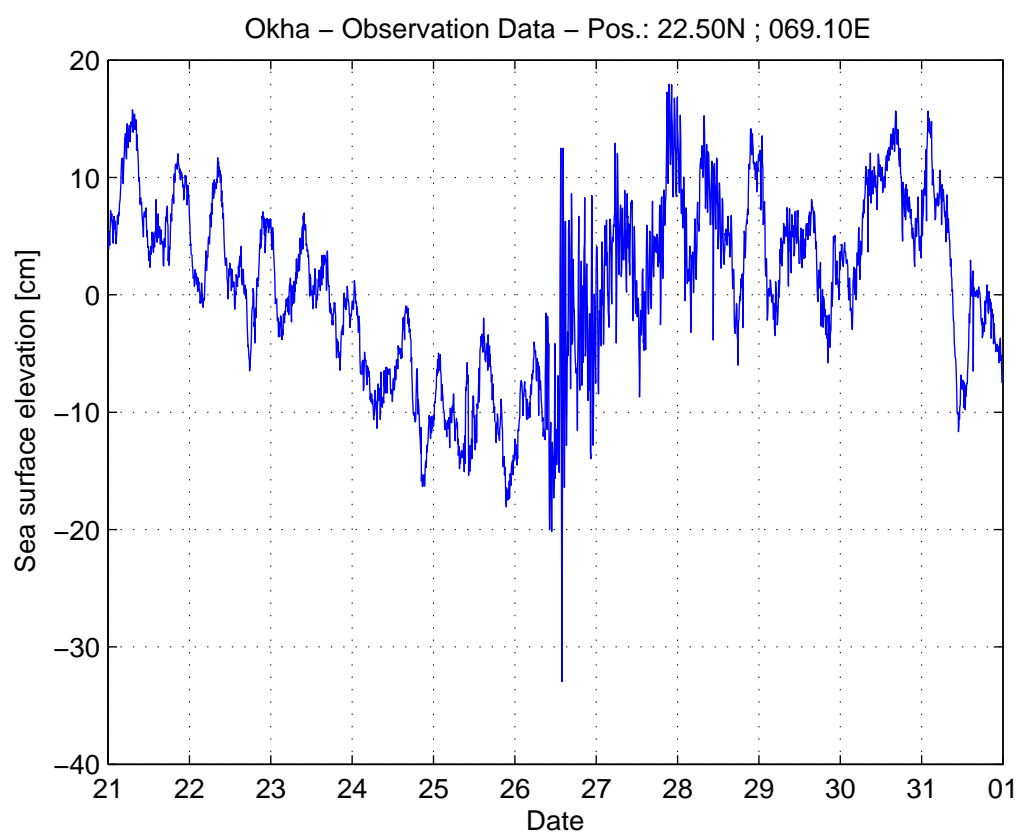


Figure 31. Time Series of the Sea Surface Elevation in Okha - India [After: [23]]

A summary of the simulation results for the tide gauge stations located at tropical Indian Ocean and west of India regions are presented in Table VI.

No	Tide Gauge Station/ Field measurement	Coordinates	Arrival Time Difference (min)	Max wave's height Relative error
1	Male	04.18 <sup>0</sup> N 073.52 <sup>0</sup> E	0	-0.2
2	Gan	00.68 <sup>0</sup> S 073.17 <sup>0</sup> E	0	-0.2
3	Diego Garcia	07.30 <sup>0</sup> S 072.38 <sup>0</sup> E	0	-0.16
4	Port Louis	20.15 <sup>0</sup> S 057.50 <sup>0</sup> E	0	(?)
5	Salalah	17.00 <sup>0</sup> N 054.00 <sup>0</sup> E	0	-0.1
6	Pointe La Rue	04.68 <sup>0</sup> S 055.53 <sup>0</sup> E	0	-0.35
7	Mormugao	15.42 <sup>0</sup> N 073.80 <sup>0</sup> E	0	-0.09
8	Okha	22.50 <sup>0</sup> N 069.10 <sup>0</sup> E	0	0

Table VI. Summary of Results for Tide Gauge Stations Located at the Tropical Indian Ocean and west of India regions

Comments:

- (1) The tide gauge at Port Louis ceased to operate for one hour [22]
- (2) The relative error is evaluated as follows:  $Error = \frac{h_{model} - h_{obs}}{h_{obs}}$

## **2. Tide Gauge Stations Located South-southeast of India**

The tsunami waves that arrived at the region of these stations emanating from the source (traveled in a parallel direction to the earthquake rupture) and to the influence of tsunami waves reflected from the southwestern coasts of the Indonesian Islands.

### **a. *Paradip Station (India)***

This station was located at  $20.26^{\circ}N, 086.70^{\circ}E$  and was approximately 600 nautical miles from the north side of the north fault segment (Figure 32). The GLOSS tide gauge of this station was sampled in 6 minutes intervals.

Figure 33 illustrates the agreement with respect to the arrival time (2 hours and 28 minutes after the earthquake) and the positive sign (wave crest) of the first wave between the tide gauge record and the model. However, there is a significant difference (25 instead of 125 centimeters) in the maximum amplitudes between the observed height and those predicted by the model. The waves that arrived at this region represent a combination of waves emanated from the source (traveling parallel to the earthquake rupture) and waves reflected from the southwestern coasts of the Indonesian Islands. Figures 34 and 35 are snapshots of the model's sea surface elevation two and three hours after the earthquake, respectively. These figures depict the waves generated by reflections from the southwestern coasts of the Indonesian Islands. Since this model does not have inundation algorithms, it cannot be expected to accurately reproduce the maximum height of the tide gauge records.

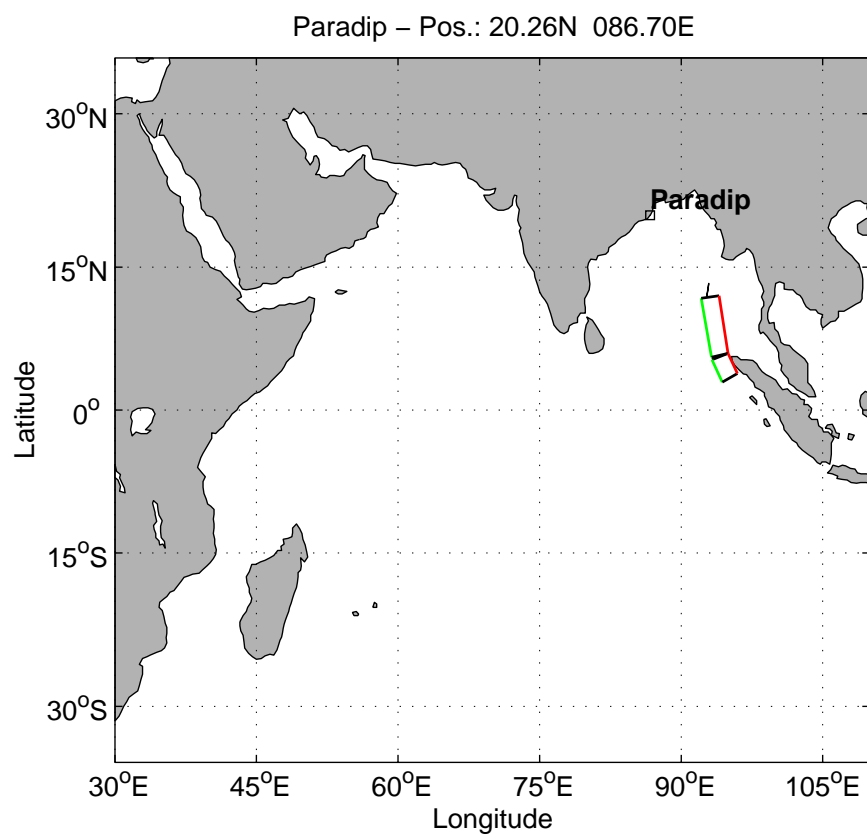


Figure 32. Paradip Tide Gauge Position

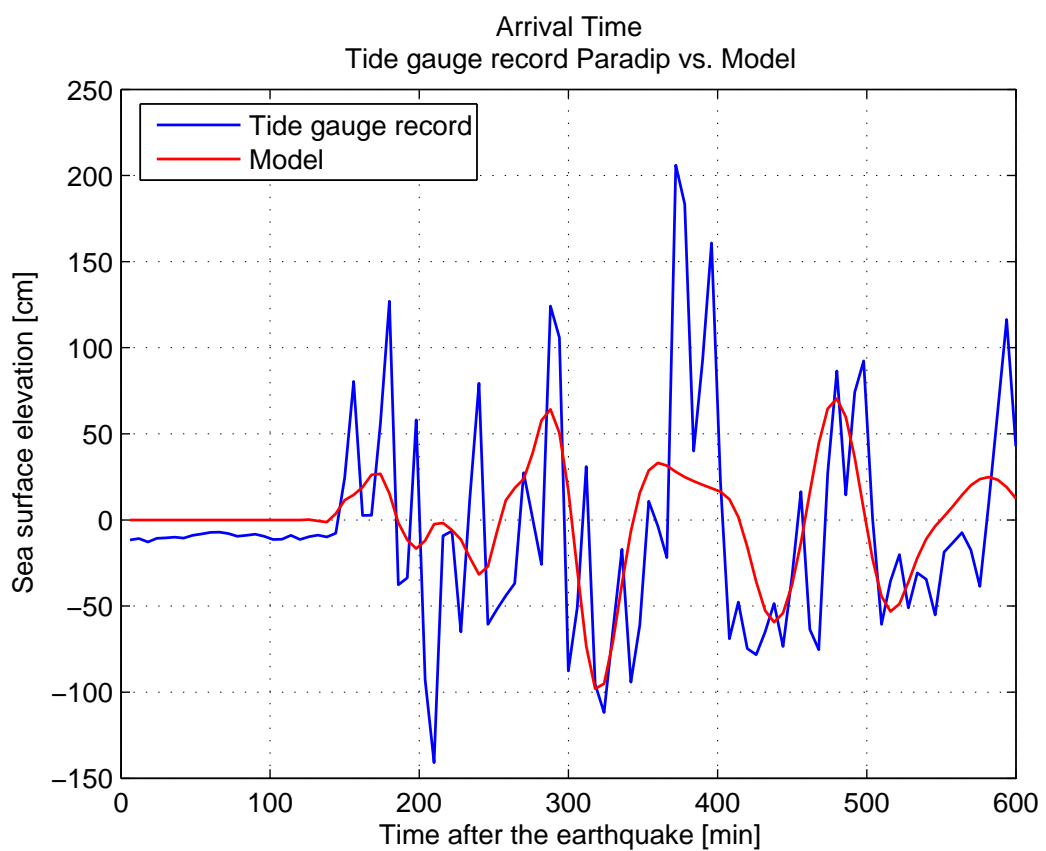


Figure 33. Comparison of arrival times - Paradip Tide Gauge vs. Model

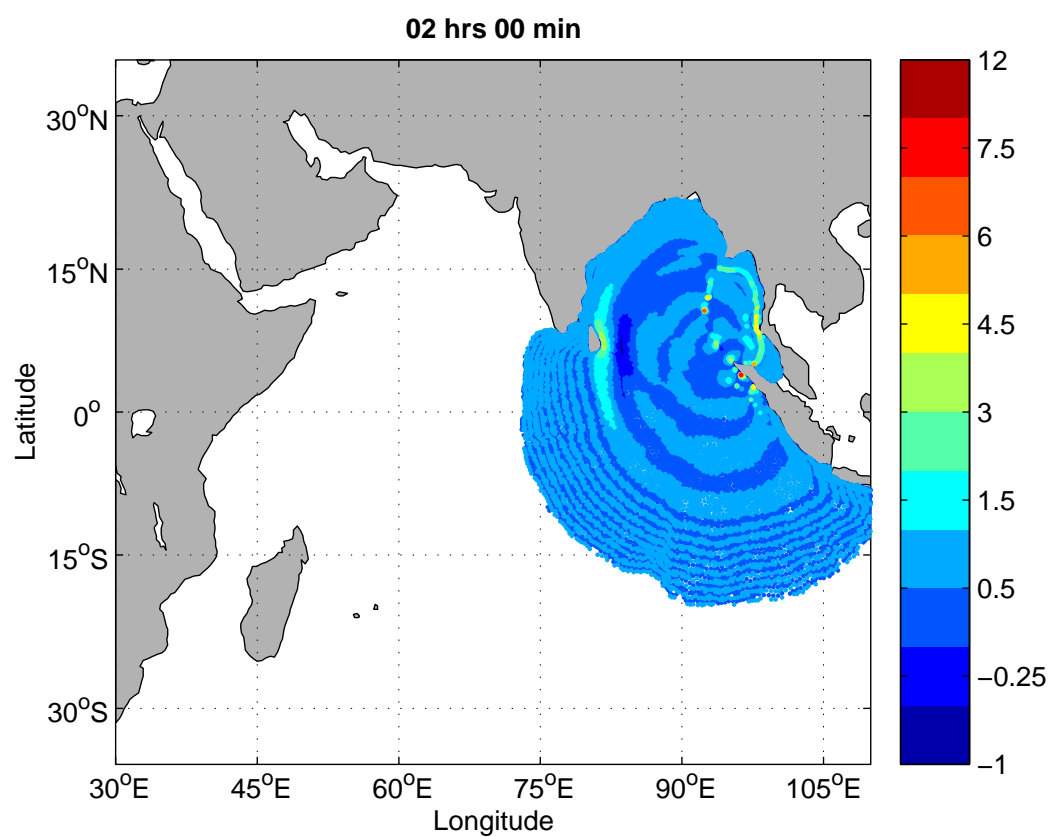


Figure 34. Model's Sea Surface Elevation Two Hours After the Earthquake

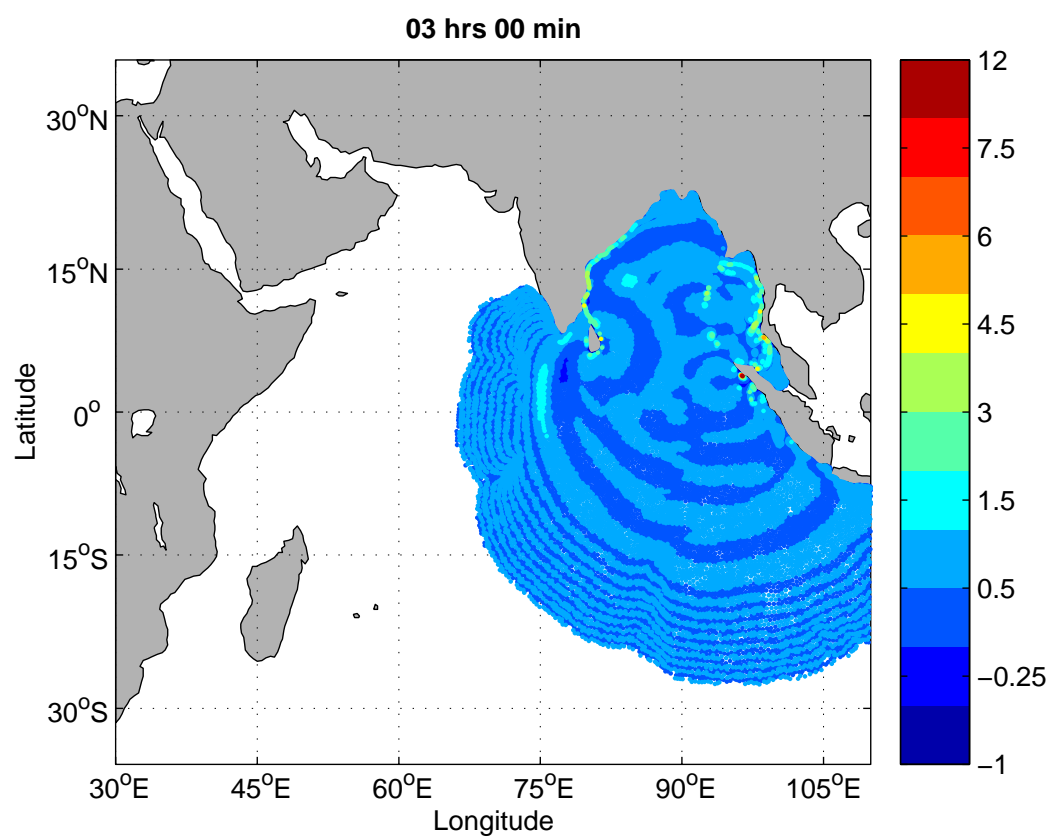


Figure 35. Model's Sea Surface Elevation Three Hours After the Earthquake

*b. Vishakapatnam Station (India)*

This station was located at  $17.65^{\circ}N, 083.28^{\circ}E$  and was approximately 700 nautical miles from the north side of the north fault segment (Figure 36). The GLOSS tide gauge of this station was sampled in 5 minutes intervals.

From Figure 37 it is obvious that the model correctly predicts the positive sign (wave crest) of the first wave but an earlier arrival time (2 hours and 26 minutes instead of 2 hours and 36 minutes after the earthquake), and underestimates the amplitude of the first wave (75 instead of 125 centimeters). As in Paradip case, this region was affected by a combination of waves from the source and waves reflected from the southwestern coasts of the Indonesian Islands.

*c. Chennai Station (India)*

This station was located at  $13.10^{\circ}N, 080.32^{\circ}E$  and was approximately 750 nautical miles from the west side of the north fault segment (Figure 38). The GLOSS tide gauge of this station was sampled in 5 minutes intervals.

Figure 39 illustrates the agreement on the arrival time (2 hours and 34 minutes after the earthquake) and the positive sign (wave crest) of the first wave between the tide gauge record and the model. The model, however, overestimates the maximum amplitude (125 instead of 70 centimeters).

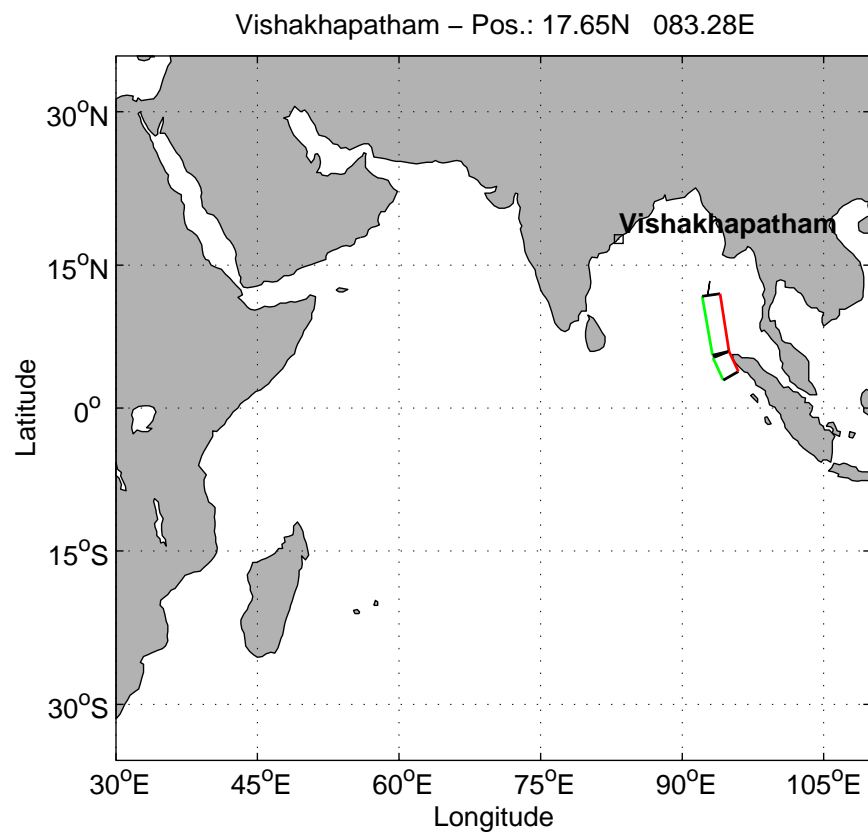


Figure 36. Vishakhapatnam Tide Gauge Position

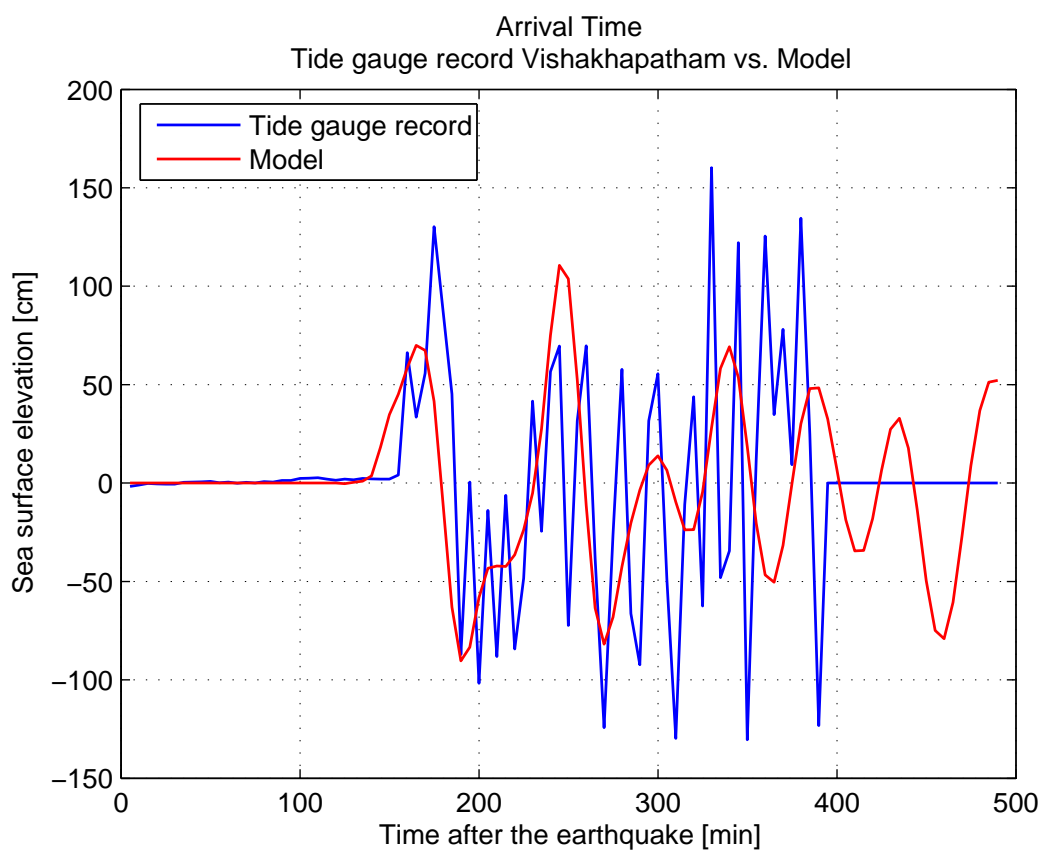


Figure 37. Comparison of arrival times - Vishakhapatnam Tide Gauge vs. Model

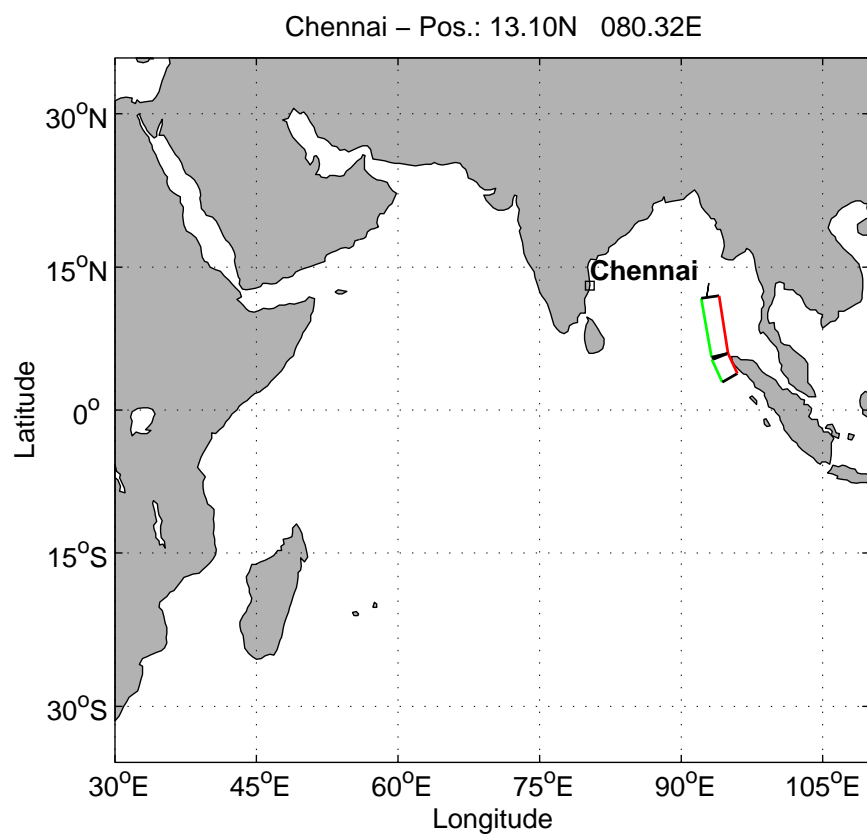


Figure 38. Chennai Tide Gauge Position

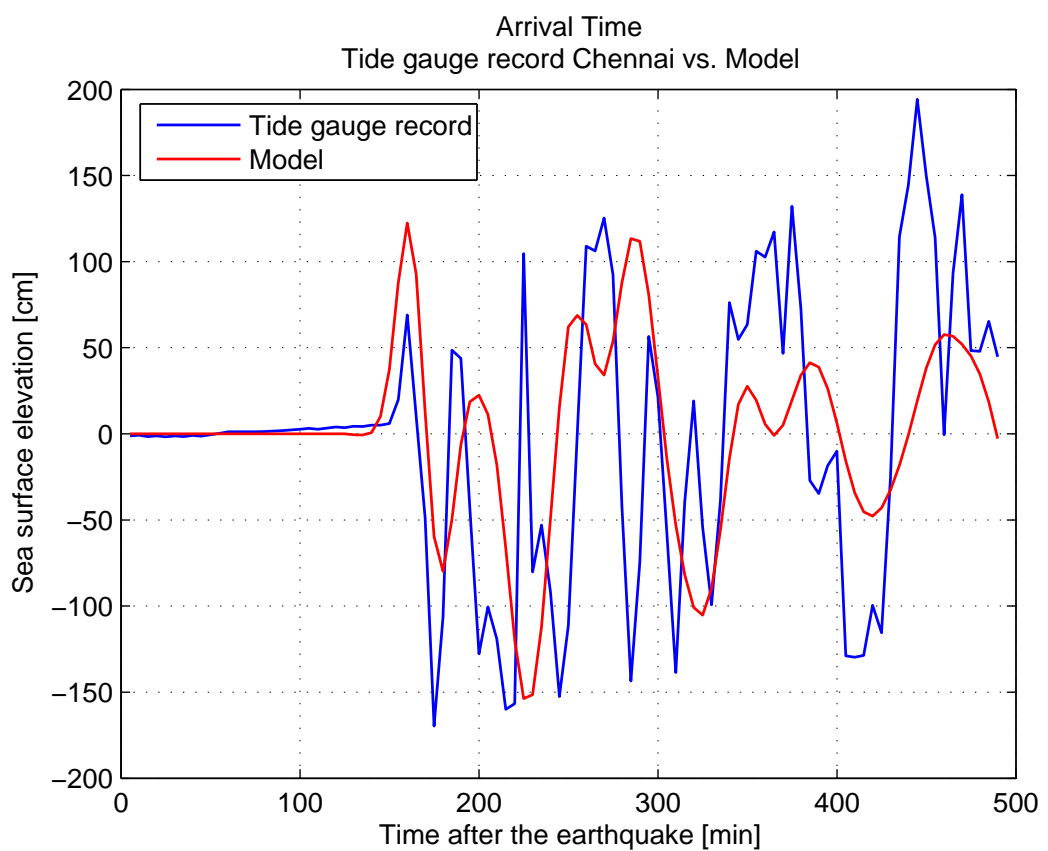


Figure 39. Comparison of arrival times - Chennai Tide Gauge vs. Model

*d. Tuticorin Station (India)*

This station was located at  $08.75^{\circ}N, 078.20^{\circ}E$  and was approximately 900 nautical miles from the west side of the north fault segment Figure(40). The GLOSS tide gauge of this station was sampled in 6 minutes intervals.

From Figure 41 it is obvious that the model correctly predicts the positive sign (wave crest) of the first wave but an earlier arrival time (3 hours and 15 minutes instead of 3 hours and 25 minutes after the earthquake), and underestimates the amplitude of the first wave (50 instead of 90 centimeters). The earlier arrival time of this case can be explained by the fact that the arrival waves, during their path from the initialization to the position of the gauge, had to pass through areas with depths less than 11 meters. Due to the boundary conditions used in the simulations (all positions with depth less than 11 meters were treated as having a depth of 11 meters in order to avoid negative water depth, this is due to the absence of inundation algorithms in the current version of the model) the model predicts earlier arrival times.

*e. Kochi Station (India)*

This station was located at  $09.97^{\circ}N, 076.27^{\circ}E$  and was approximately 1,050 nautical miles from the west side of the north fault segment (Figure 42). The GLOSS tide gauge of this station was sampled in 6 minutes intervals.

Figure 43 shows that the model correctly predicts the positive sign (wave crest) of the first wave but an earlier arrival time (4 hours and 22 minutes instead of 4 hours and 42 min after the earthquake), and overestimates the amplitude of the first wave (85 instead of 70 centimeters). The earlier arrival time can be explained again because of the no-flux boundary conditions used along the coastlines.

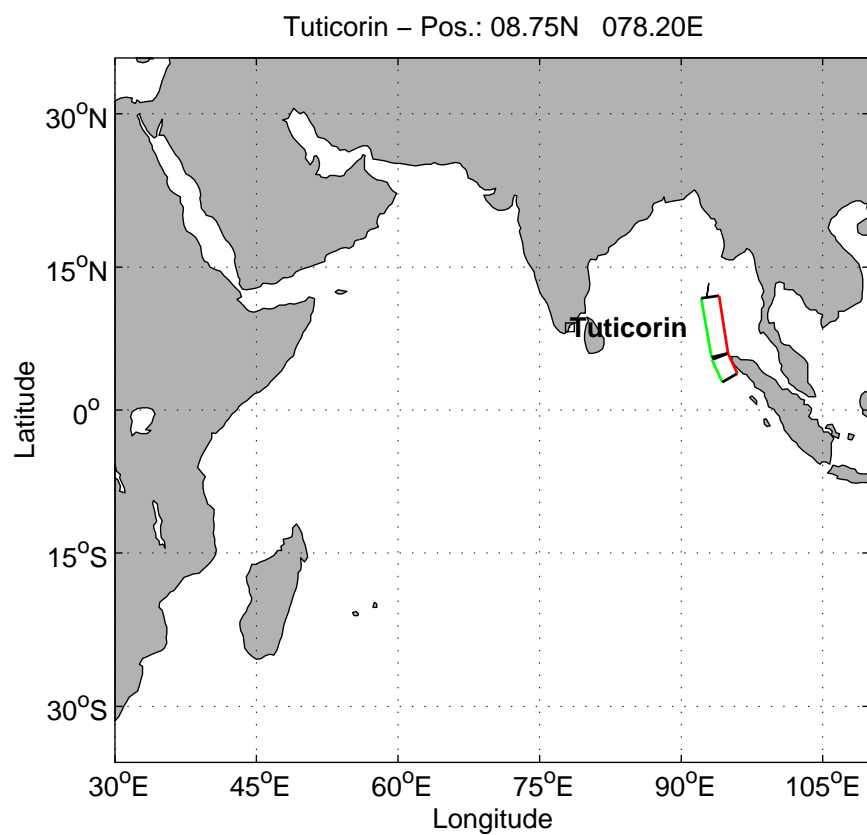


Figure 40. Tuticorin Tide Gauge Position

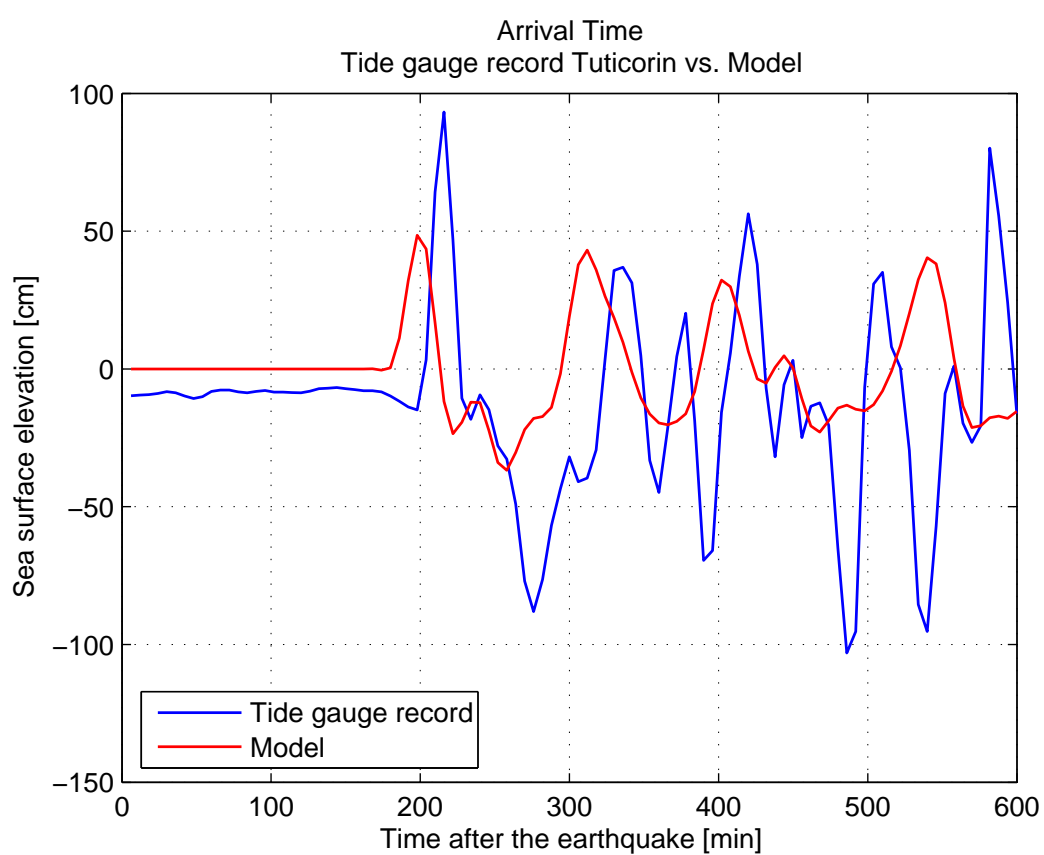


Figure 41. Comparison of arrival times - Tuticorin Tide Gauge vs. Model

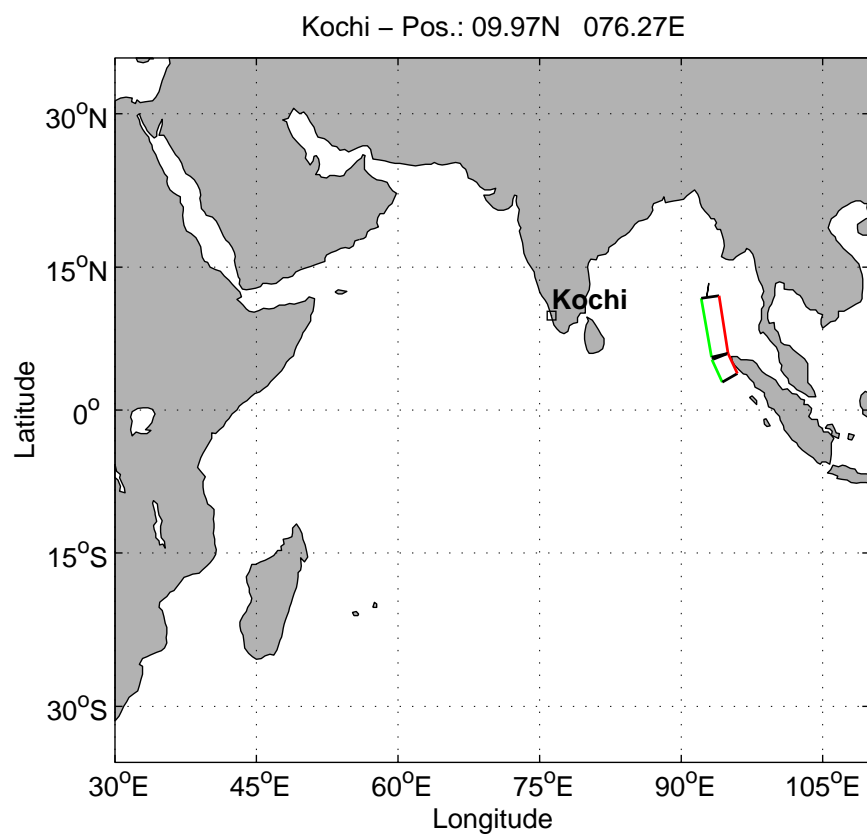


Figure 42. Kochi Tide Gauge Position

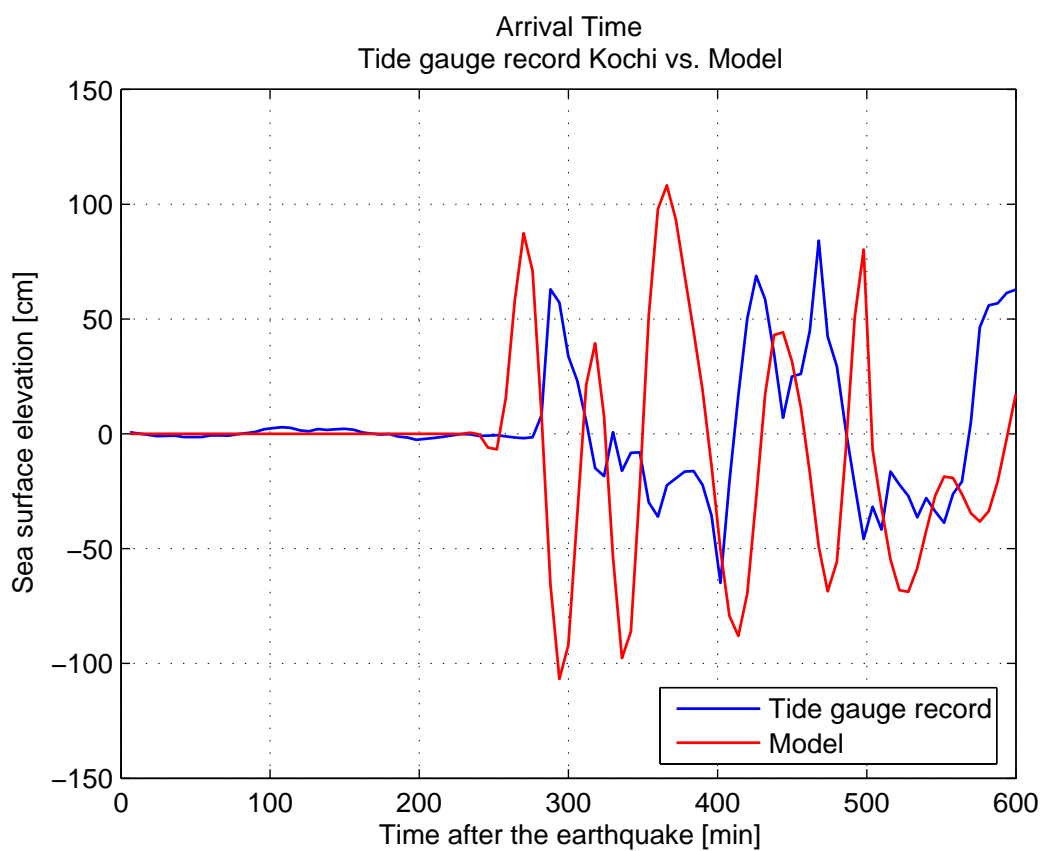


Figure 43. Comparison of arrival times - Kochi Tide Gauge vs. Model

*f. Colombo Station (Sri Lanka)*

This station was located at  $06.93^{\circ}N, 079.83^{\circ}E$  and was approximately 800 nautical miles from the west side of the north fault segment (Figure 44). The GLOSS tide gauge of this station was sampled in 2 minutes intervals, was damaged by the first tsunami wave, and did not operate for 5 hours and 40 minutes [22]. According to eyewitness accounts, the second wave was the highest.

Figure 45 depicts the agreement between the tide gauge record and the model that the first wave was positive (wave crest) and the highest wave was the second. There is a difference on the arrival time (2 hours and 35 min instead of 2 hours and 50 min after the earthquake) for the first wave and also a difference in its maximum amplitude (80 instead of 200 centimeters).

*g. Hanimaadhoo Station (Maldives)*

This station was located at  $06.77^{\circ}N, 073.18^{\circ}E$  and was approximately 1,200 nautical miles from the west side of the north fault segment (Figure 46). The GLOSS tide gauge of this station was sampled in 2 minutes intervals.

Figure 47 depicts the agreement between the tide gauge record and the model on that the first wave was positive (wave crest). There is a small difference on arrival time (3 hours and 26 minutes instead of 3 hours 31 minutes after the earthquake) for the first wave and also a difference in its maximum amplitude (60 instead of 160 centimeters).

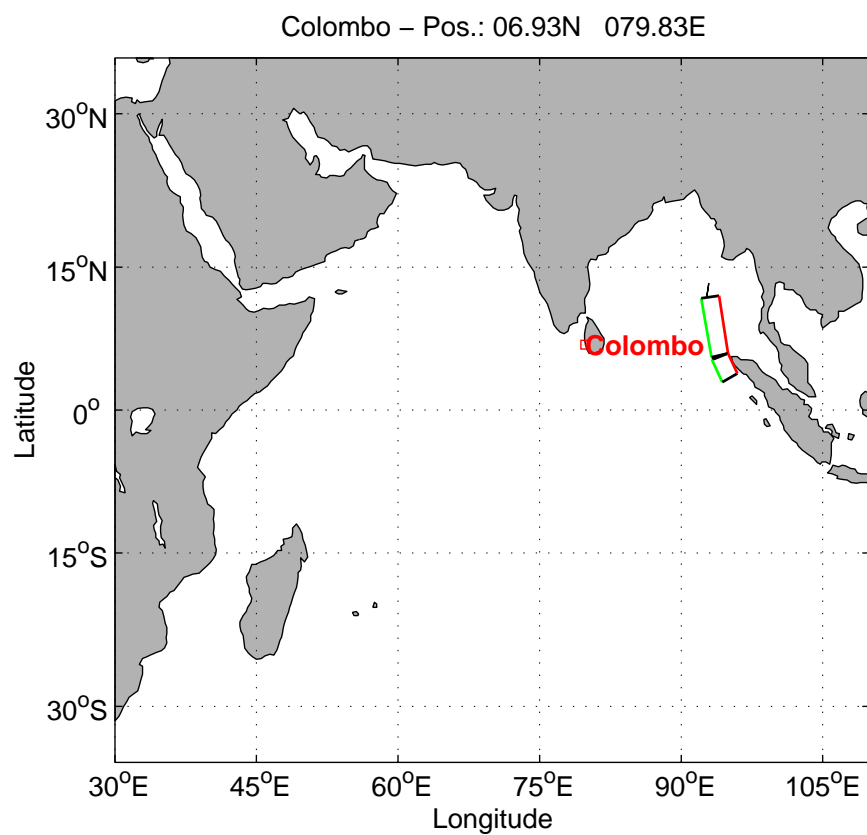


Figure 44. Colombo Tide Gauge Position

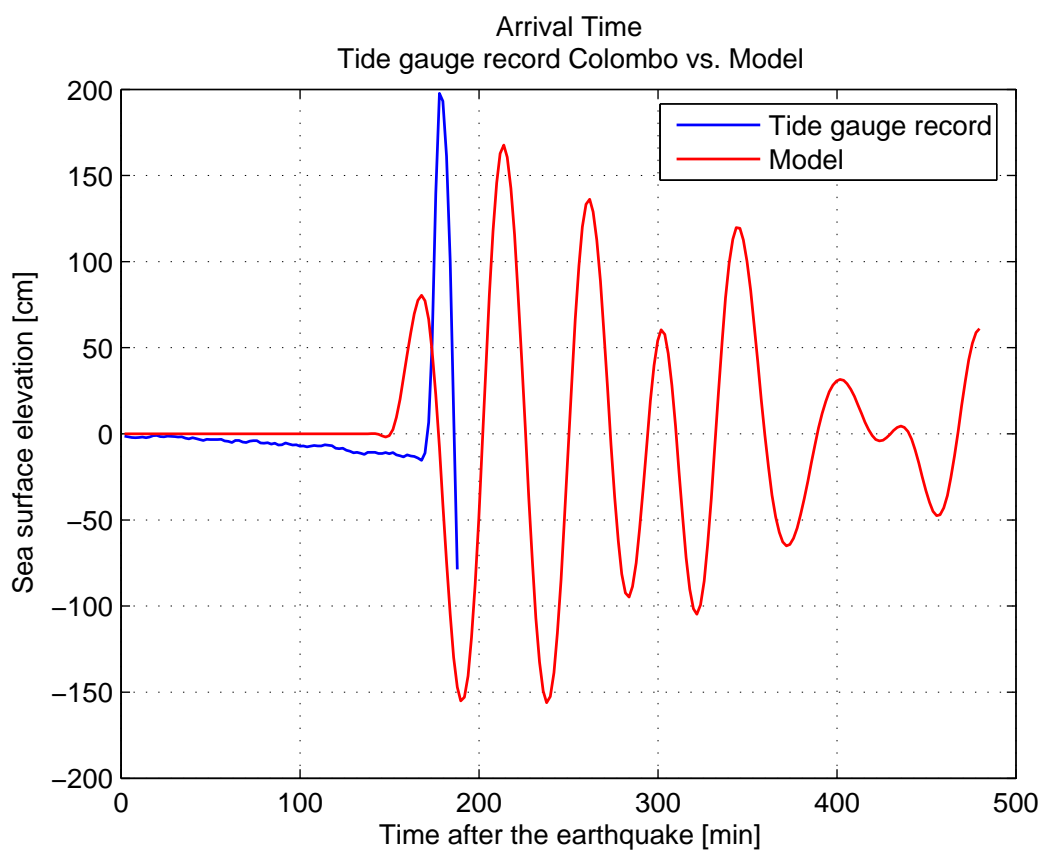


Figure 45. Comparison of arrival times - Colombo Tide Gauge vs. Model

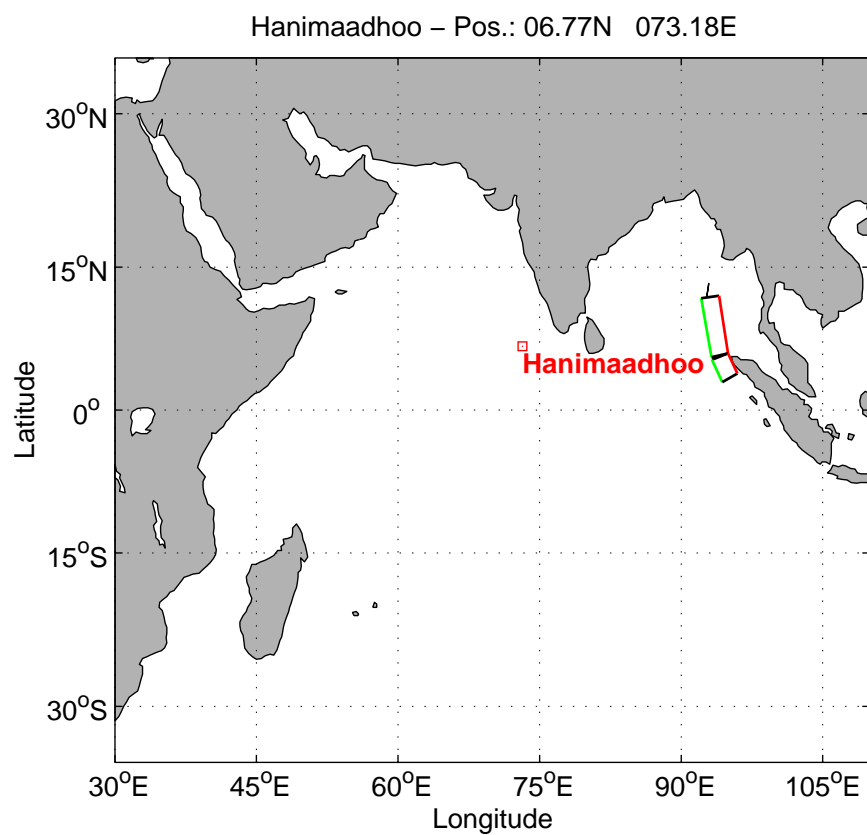


Figure 46. Hanimaadhoo Tide Gauge Position

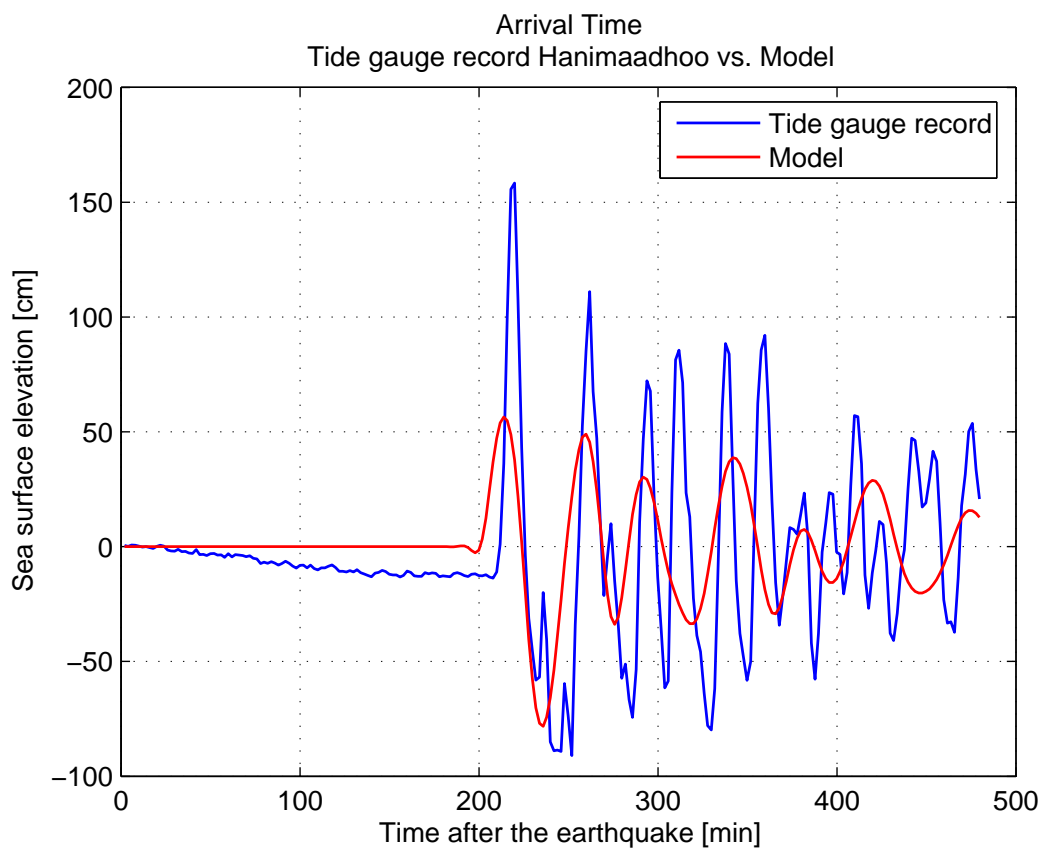


Figure 47. Comparison of Arrival Times Hanimaadhoo Tide Gauge vs. Model

A summary of simulation's results for the tide gauge stations located at South - Southeast of India is presented in Table VII.

No	Tide Gauge Station/ Field measurement	Coordinates	Arrival Time Difference (min)	Max wave's height Relative error
1	Paradip	20.26 <sup>0</sup> N 086.70 <sup>0</sup> E	0	-0.8
2	Vishakhapatnam	17.65 <sup>0</sup> N 083.28 <sup>0</sup> E	-10	-0.4
3	Chennai	13.10 <sup>0</sup> N 080.32 <sup>0</sup> E	0	0.78
4	Tuticorin	08.75 <sup>0</sup> N 078.20 <sup>0</sup> E	-10	-0.44
5	Kochi (Cochin)	09.97 <sup>0</sup> N 076.27 <sup>0</sup> E	-20	0.38
6	Colombo	06.93 <sup>0</sup> N 079.83 <sup>0</sup> E	-15	-0.6
7	Hanimaadhoo	06.77 <sup>0</sup> N 073.18 <sup>0</sup> E	-5	-0.6

Table VII. Summary of Results for the Tide Gauge Stations Located at the South-Southeast of India regions

Comment:

(1) The relative error is evaluated as follows:  $Error = \frac{h_{model} - h_{obs}}{h_{obs}}$

## B. COMPARISON TO SATELLITE ALTIMETRY

### 1. Jason 1

One of the three satellites used in this study was Jason-1. This satellite crossed the equator at 2:55 a.m. UTC, which was two hours after the earthquake [26], and its altimeter recorded the differences in the sea surface elevation in the Bay of Bengal. Figure 48 presents the model's sea surface elevation two hours after the earthquake. The black line in this figure represents the points used to compare sea surface elevation in Figure 49 between the satellite's altimetry data (blue line) and the model's data (red dots). The model estimates very accurately the leading wave crest at about  $5^{\circ}\text{S}$  and the double peak structure between this and the equator, although the heights are lower than the observations. However, between  $5^{\circ}\text{N}$  to  $12^{\circ}\text{N}$  the model's crest is in contrast to the observation's trough. Finally, between  $12^{\circ}\text{N}$  to  $20^{\circ}\text{N}$  the model and satellite data are in total agreement and specifically, the model estimates very accurately the leading wave crest at about  $20^{\circ}\text{N}$ .

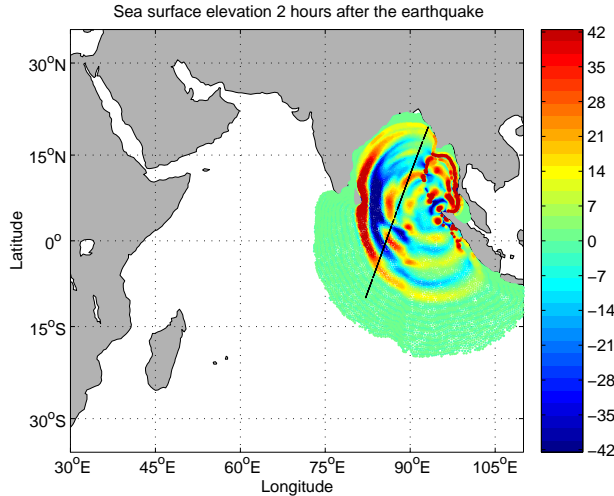


Figure 48. Model's Sea Surface Elevation Two Hours After the Earthquake

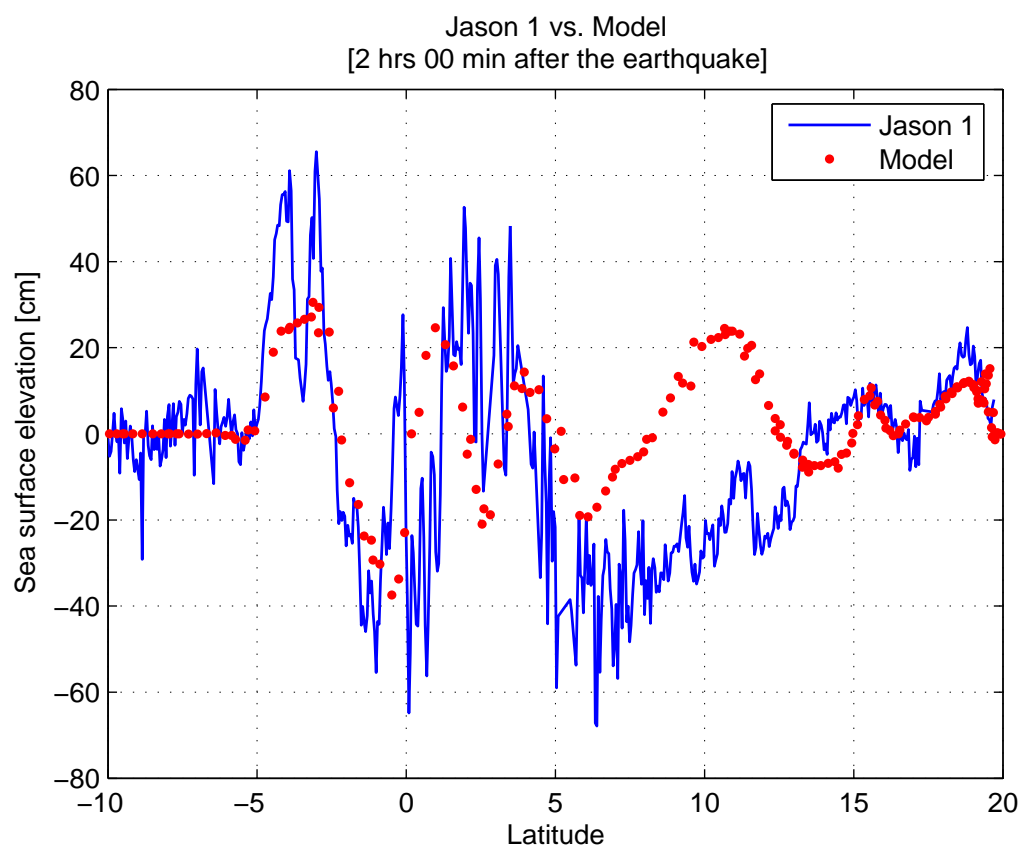


Figure 49. Comparison of Jason 1 vs. Model

## 2. Topex/Poseidon

The second satellite used in this study was Topex/Poseidon. This satellite crossed the equator at 3:00 a.m. UTC. Figure 50 presents the model's sea surface elevation two hours and five minutes after the earthquake. Again, the black line represents the points used for comparing sea surface elevation in Figure 51 between the satellite's altimetry data (blue line) and the model's data (red dots). In this case, the satellite's altimetry data contain several gaps. The model estimates very accurately the leading wave crest at about  $5^{\circ}$ S. The gaps in the satellite's data between  $5^{\circ}$ N and the equator do not show the double peak structure that was evident in Jason-1 data. Between  $12^{\circ}$ N to  $20^{\circ}$ N the model and the satellite's data are in exceptional agreement, and in particular, the model estimates very accurately the leading wave crest at about  $20^{\circ}$ N.

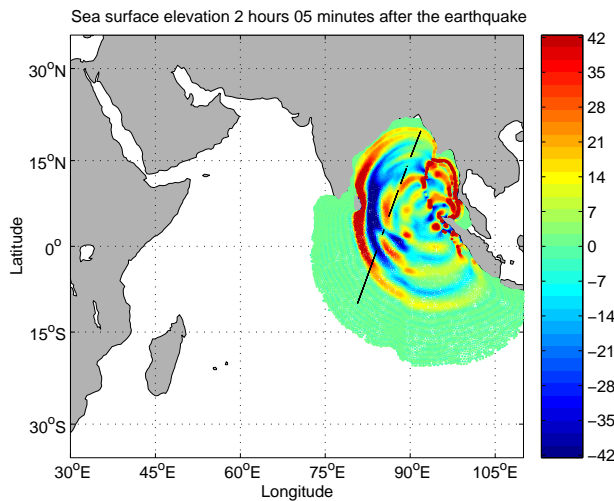


Figure 50. Model's Sea Surface Elevation Two Hours and Five Minutes After the Earthquake

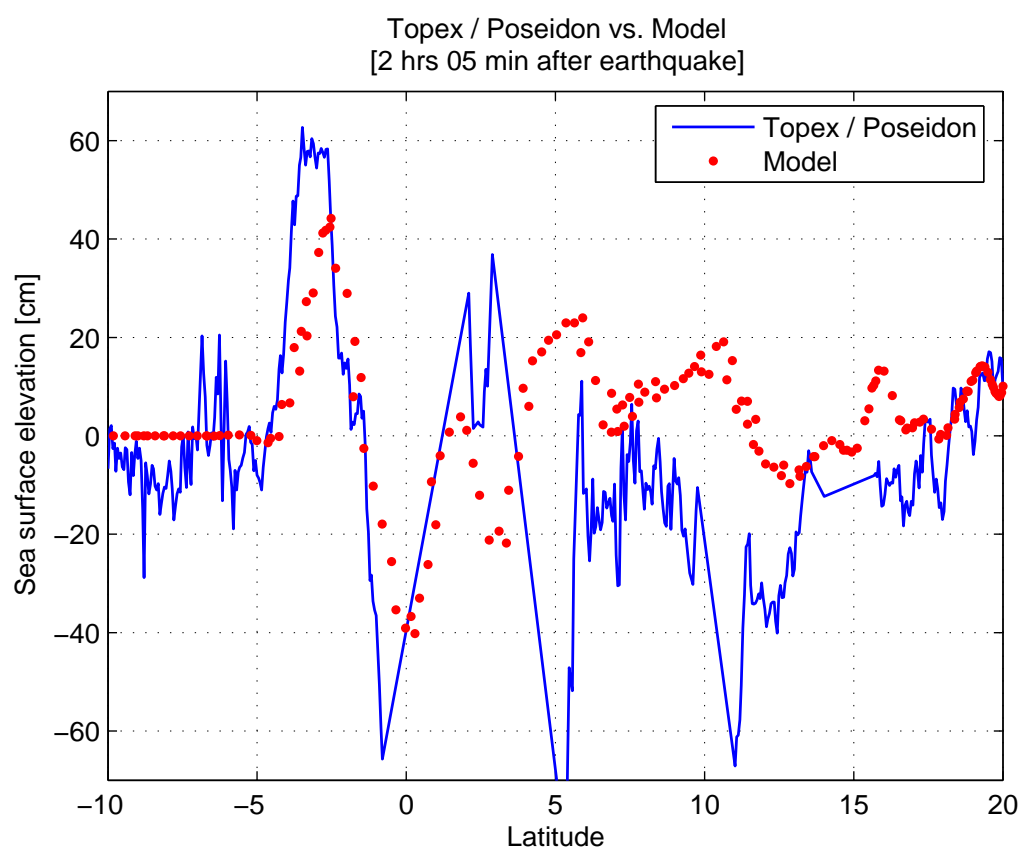


Figure 51. Comparison of Topex/Poseidon vs. Model

### 3. Envisat

Envisat's altimetry data were also used in this study. Envisat crossed the equator at 4:14 a.m. UTC. Figure 52 presents the model's sea surface elevation three hours and fifteen minutes after the earthquake. The black line, as previously, represents the points used to compare the sea surface elevation compared in Figure (53) between the satellite's altimetry data (blue line) and the model's data (red dots). In general, this comparison indicates that the simulation is very accurate in representing tsunami waves. In addition to the previous two cases, the reflected wave from Sri Lanka between  $10^0\text{N}$  to  $15^0\text{N}$  is reproduced also accurately. The height is slightly lower, due to the lack of inundation algorithms, which affects the wave heights by the introduction of artificially deep waters at the shallow depth near coastlines.

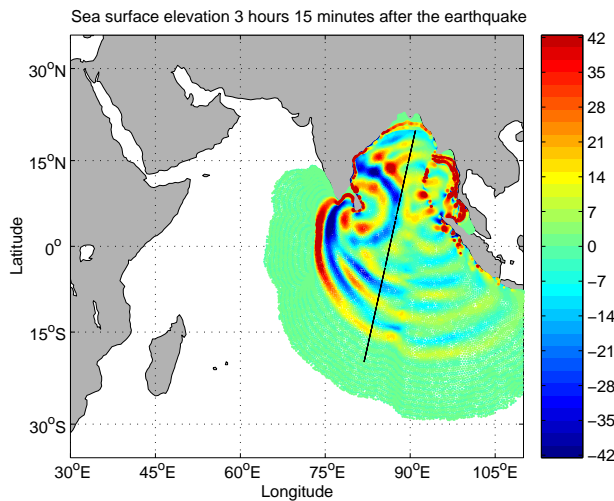


Figure 52. Model's Sea Surface Elevation Three Hours and Fifteen Minutes After the Earthquake

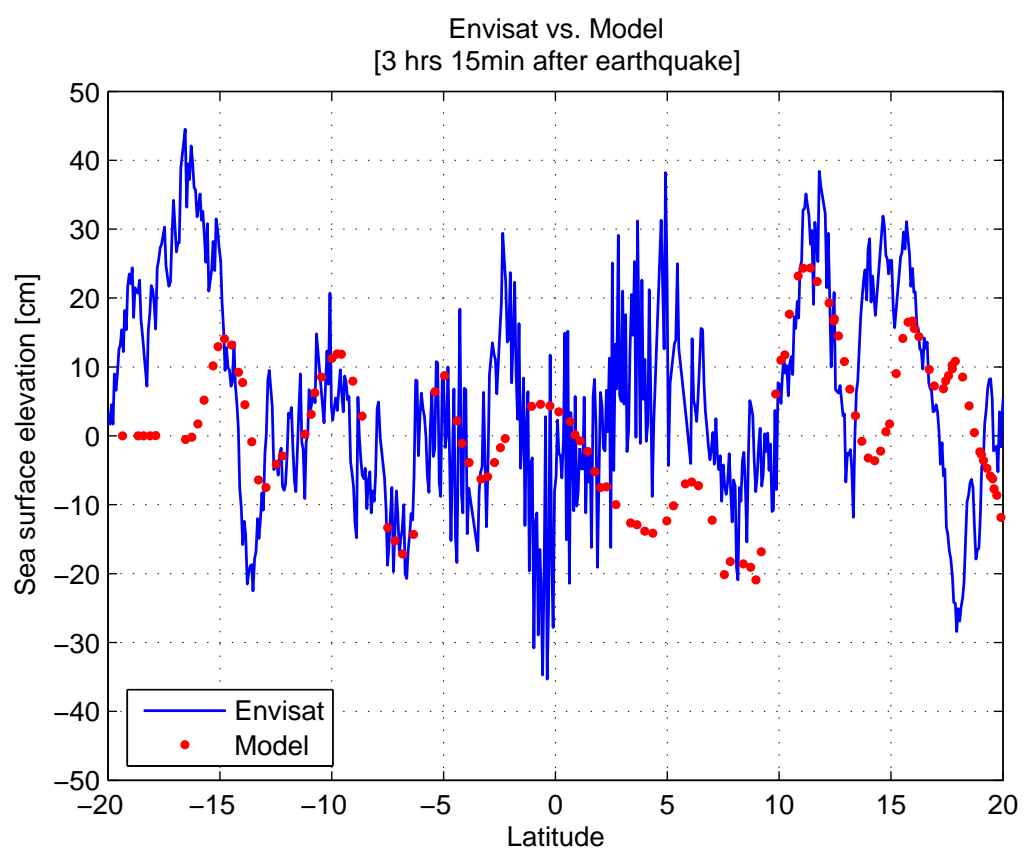


Figure 53. Comparison of Envisat vs. Model

## C. COMPARISON TO FIELD MEASUREMENTS

### 1. Mercator

During the Indian Ocean tsunami, the Mercator, was anchored about 1.6 kilometers off the Phuket coast (Thailand) and specifically at the location  $07.715^{\circ}N$ ,  $098.28^{\circ}E$ . Based on the yacht's depth gauge measurements, the first wave (trough) arrived at its location at 02:38 a.m. UTC, one hour and thirty-nine minutes after the earthquake, while the three main tsunami waves had trough-to-crest wave heights of 6.6, 2.2, and 5.5 meters. Figure 54 depicts the simulated elevations and also indicates the observed arrival time. The model appears to simulate very accurately the arrival time of the first wave at the Mercator's location and that this was negative (wave trough), indicating the subsidence on the eastern side of the initialization area. However, the amplitude is underestimated. The reason for that, by taking into account similar difficulties of other models [31], is most likely caused by misrepresentation of the water depth. The simulated water depth (grid depth) at the Mercator's location was 45 meters in comparison to an observed of 12 meters.

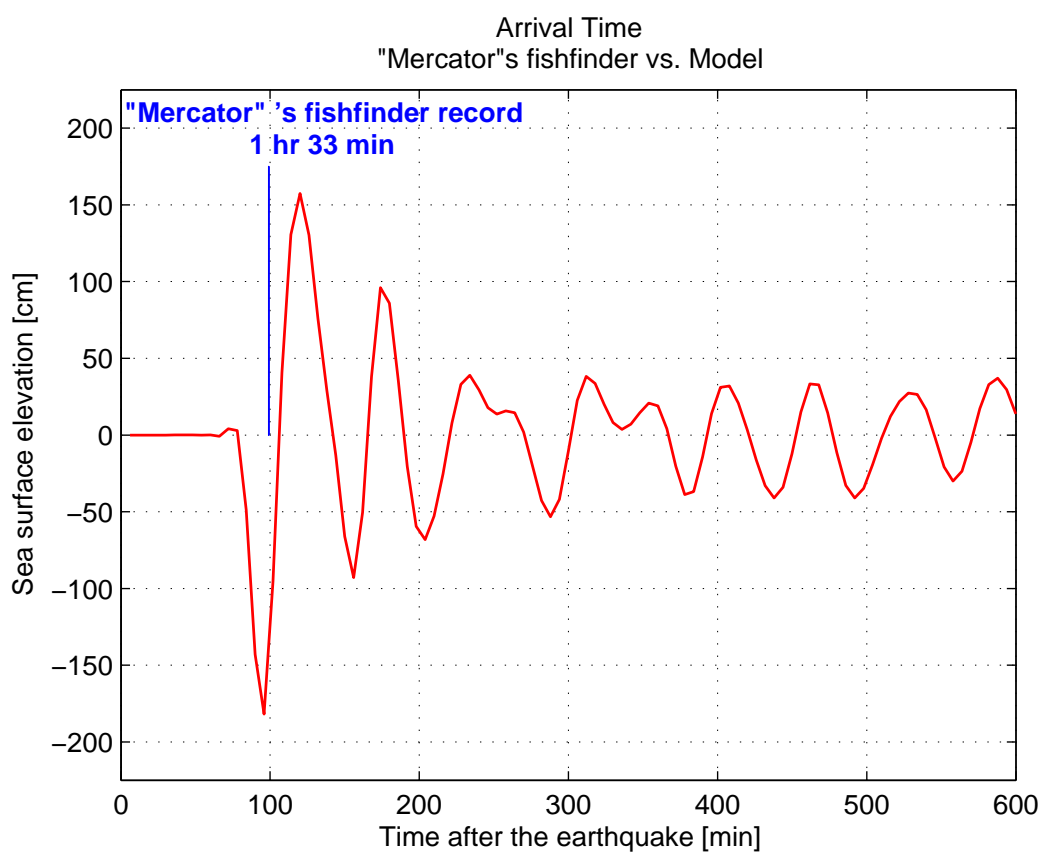


Figure 54. Comparison of arrival times - Mercator's fishfinder vs. Model

## D. SYNOPSIS

From the examination of the foregoing results it is evident that:

1. The model accurately predicts the positive (wave crest) first wave at all tide gauge stations positions due to the uplift of the western side of the initialization area, and the negative (wave trough) at the location of the Mercator due to the subsidence on the eastern side.
2. The model simulates very accurately the arrival times and the amplitudes of the first tsunami waves for the tropical Indian Ocean (Male, Gan, Diego Garcia, Port Louis, Salalah, and Pointe La Rue) and the southwest Indian tide gauge stations (Okha and Mormugao). All these stations received tsunami waves directly from the source area.
3. The differences in arrival times or in maximum amplitudes between simulation results and records from the Indian tide gauge stations (Paradip, Vishakhapatnam, Chennai, Tuticorin, Kochi, Colombo and Hanimaadhoo (Maldives)) are due to the absence of inundation algorithms. According to [22], the tsunami waves that arrived at these stations, combined of waves traveling parallel to the earthquake rupture and waves reflected from the southwestern coasts of the Indonesian Islands. Additionally, in the Hanimaadhoo, Colombo, Tuticorin, and Kochi stations' cases, the tsunami waves had to pass over areas with depths less than 11 meters. Due to the boundary conditions used at these simulations (all positions with depths less than 11 meters were treated as having depths of 11 meters) the model predicts earlier arrival times.
4. The model underestimates the amplitude of the arrived tsunami waves at the Mercator's location due to misrepresentation of the water depth by the used mesh grid.
5. By taking into account that the tsunami wave amplitude squared is proportional to the potential energy, the results depict the west and southwest propagation of most of the energy due to the orientation of the earthquake rupture (see Figure

55). Only a fraction of the energy propagated toward the south and southeast, which is in agreement with [22].

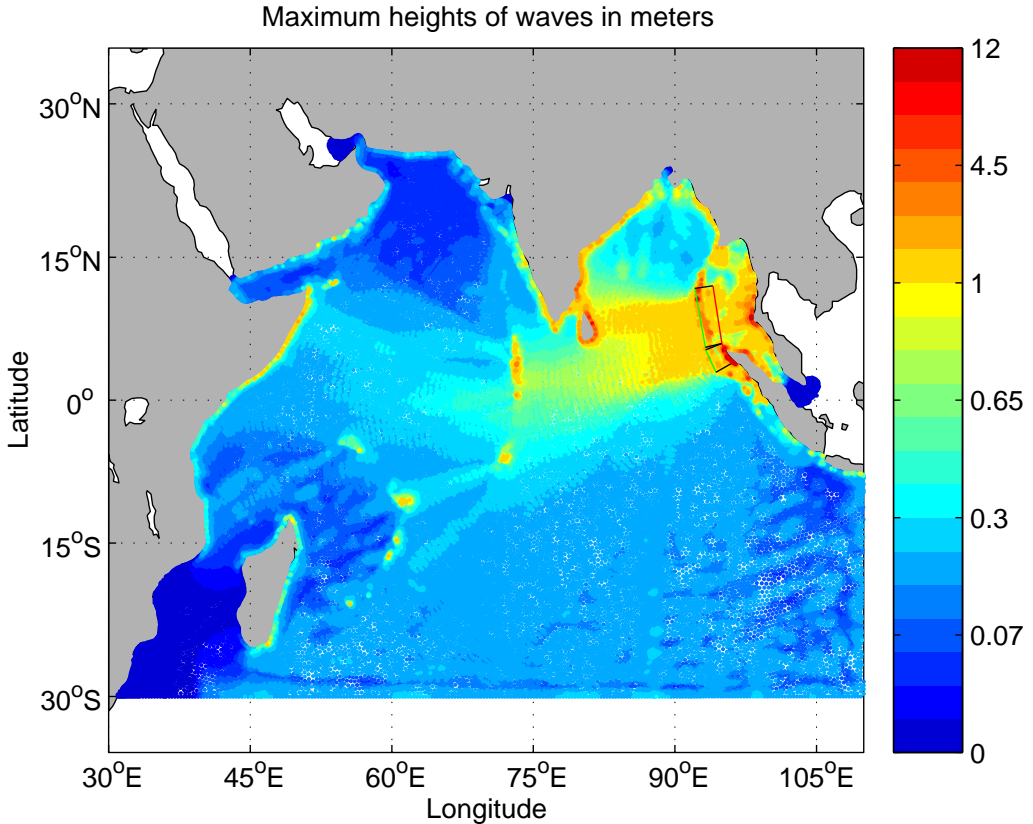


Figure 55. Energy Propagation of the Simulated Tsunami Waves

6. According to [22] the mid-ocean ridges played a major role as wave guides that transferred the tsunami energy to far-field regions outside the source area in the Indian Ocean. The model reproduced this feature very accurately as illustrated in Figure 55 in combination with Figure 1. Finally, Figure 55 presents, the areas where the tsunami focused most of its energy.

THIS PAGE INTENTIONALLY LEFT BLANK

## V. CONCLUSIONS AND RECOMMENDATIONS

This study, as part of a research effort regarding the development of a triangular discontinuous Galerkin oceanic shallow water model, formatted real bathymetry data of the Indian Ocean and simulated the propagation stage of the Indian Ocean tsunami that occurred on December 26, 2004. The model's main advantage is related to the geometric (grid) flexibility, which made it possible to represent the tsunami's propagation with different resolutions throughout the Indian Ocean.

The model's results were compared to the records of fifteen tide gauge stations around the Indian Ocean, satellite altimetry (Jason-1, Topex/Poseidon and Envisat data), and field measurements. These results showed that the model is capable of producing accurate estimates of arrival times at distant locations. Some considerable differences were noticed from the above comparisons due to influences by reflections, misrepresentation of the water depth by the mesh grid, and the no-flux boundary conditions serving as a proxy for inundation algorithms.

The thesis also derived the analytic solution of the linear Munk problem (two-dimensional problem) for future use in validating the diffusion operators that were not used in the tsunami simulations.

Future studies should involve the following:

- 1) The use of inundation algorithms in order to complete the simulation of the Indian Ocean tsunami December 26, 2004 (propagation and run-up stages), by using this DG model. These results could be compared against the already existing de-tidal records.
- 2) The simulation of the Indian Ocean tsunami December 26, 2004 (propagation and run-up stages), by using this DG model and more complicated initial conditions (for example more than two planes).
- 3) The simulation of earthquakes with different magnitude for the same region

of the Indian Ocean, or the simulation in other parts of the world, in order to identify the regions that are likely to be severely affected by tsunami waves, and to establish seismic criteria for issuing tsunami warnings in the case of actual tsunamis.

4) The effects of storm surge modeling (propagation and run-up) caused by hurricanes, cyclones and typhoons on coastal areas.

## APPENDIX A. DERIVATION OF ANALYTIC SOLUTION FOR THE MUNK PROBLEM

In Stommel's theory, the inclusion of the bottom friction raises the order of the governing equation and enables the beta effect to produce a western boundary current [19], which makes Stommel's solution not quite realistic. The ocean currents are concentrated in the upper kilometer of the ocean, they are not barotropic, and they are not independent of depth.

Walter Heinrich Munk noted that the frictional effect due to small-scale eddies is crucially important in ocean dynamics, and solved the problem by considering the lateral eddy viscosity to explain the ocean current distribution, based on the observed wind system.

Consider a flat-bottomed ocean of depth  $H$  driven by wind stress at its surface. The momentum shallow water equations in two-dimensions, where bottom drag has been neglected while the lateral eddy viscosity is included, are:

$$fu = -\frac{1}{\rho_o} \frac{\partial p}{\partial y} + \nu \left( \frac{\partial^2 v}{\partial x^2} + \frac{\partial^2 v}{\partial y^2} \right) + \frac{1}{\rho_o} \frac{\partial \tau_y}{\partial z} \quad (\text{A.1})$$

$$-fv = -\frac{1}{\rho_o} \frac{\partial p}{\partial x} + \nu \left( \frac{\partial^2 u}{\partial x^2} + \frac{\partial^2 u}{\partial y^2} \right) + \frac{1}{\rho_o} \frac{\partial \tau_x}{\partial z} \quad (\text{A.2})$$

Pressure can be eliminated by cross differentiating these equations and taking the difference  $\frac{\partial}{\partial x}(A.1) - \frac{\partial}{\partial y}(A.2)$ :

$$\begin{aligned} \frac{\partial}{\partial x}(fu) + \frac{\partial}{\partial y}(fv) &= \nu \nabla_H^2 \left( \frac{\partial v}{\partial x} - \frac{\partial u}{\partial y} \right) + \frac{1}{\rho_o} \frac{\partial}{\partial z}(\text{curl} \vec{\tau}) \Rightarrow \\ f \left( \frac{\partial u}{\partial x} + \frac{\partial v}{\partial y} \right) + \frac{\partial f}{\partial y} v &= \nu \nabla_H^2 \left( \frac{\partial v}{\partial x} - \frac{\partial u}{\partial y} \right) + \frac{1}{\rho_o} \frac{\partial}{\partial z}(\text{curl} \vec{\tau}) \end{aligned} \quad (\text{A.3})$$

The use of the continuity equation  $\frac{\partial u}{\partial x} + \frac{\partial v}{\partial y} + \frac{\partial w}{\partial z} = 0$  and beta-plane approximation  $\beta = \frac{\partial f}{\partial y}$  into Equation (A.3), gives the following:

$$\begin{aligned} f \left( -\frac{\partial w}{\partial z} \right) + \beta v &= \nu \nabla_H^2 \left( \frac{\partial v}{\partial x} - \frac{\partial u}{\partial y} \right) + \frac{1}{\rho_o} \frac{\partial}{\partial z}(\text{curl} \vec{\tau}) \Rightarrow \\ \beta v - f \frac{\partial w}{\partial z} &= \nu \nabla_H^2 \left( \frac{\partial v}{\partial x} - \frac{\partial u}{\partial y} \right) + \frac{1}{\rho_o} \frac{\partial}{\partial z}(\text{curl} \vec{\tau}) \end{aligned} \quad (\text{A.4})$$

The Equation (A.4), after multiplying by  $\rho_o$ , integrating from the bottom (-H) to the surface (zero) in the vertical with boundary conditions  $w = 0$  at  $z = 0$  and  $z = -H$ , assuming zero bottom friction, and using the definition of the streamfunction:

$$\rho_o \int_{-H}^0 u dz = M_x = -\frac{\partial \Psi}{\partial y} \quad (\text{A.5})$$

$$\rho_o \int_{-H}^0 v dz = M_y = -\frac{\partial \Psi}{\partial x} \quad (\text{A.6})$$

gives the following:

$$\underbrace{\beta \frac{\partial \Psi}{\partial x}}_{\text{Coriolis}} = \underbrace{\nu \nabla_H^4 \Psi}_{\text{Lateral Friction}} + \underbrace{\text{curl} \vec{\tau}_o}_{\text{Winds}} \quad (\text{A.7})$$

According to Munk, in the western boundary layer (WBL) Coriolis force is being balanced by the lateral friction while at the interior, Coriolis is being balanced by the wind's effect:

### Western Boundary Layer

$$\beta \frac{\partial \Psi}{\partial x} \approx \nu \nabla_H^4 \Psi$$

### Interior

$$\beta \frac{\partial \Psi}{\partial x} \approx \text{curl} \vec{\tau}_o$$

Consider the idealized model for the North Atlantic subtropical gyre, where:

- $L_x = 5000 \text{ km}$
- $L_y = 2500 \text{ km}$
- $L_m$  is the width of the WBL, ( $L_m \ll L_x$ )
- $\tau_{ox} = -A \cos \frac{\pi y}{L_y}$  is the x-component of the wind force
- $\tau_{oy} = 0$  is the y-component of the wind force
- $A = 0.1 \frac{N}{m}$ .

#### *i. Interior Solution*

The solution of the equation

$$\beta \frac{\partial \Psi}{\partial x} = \text{curl} \vec{\tau}_o$$

is as follows:

$$\Psi(x, y) = \hat{\Psi}(x) \sin\left(\frac{\pi y}{L_y}\right)$$

where

$$\hat{\Psi}(x) = \frac{A\pi}{\beta L_y} (L_x - x)$$

Thus, at the interior,  $L_m \leq x \leq L_x$  and  $0 \leq y \leq L_y$ , the streamfunction solution can be written as

$$\Psi(x, y) = \frac{A\pi}{\beta L_y} (L_x - x) \sin\left(\frac{\pi y}{L_y}\right) \quad (\text{A.8})$$

The use of Equation (A.8) and Equations (A.5) and (A.6) of the streamfunction's definition gives

$$u = -\frac{A\pi^2}{\beta L_y^2 \rho_o H} (L_x - x) \cos\left(\frac{\pi y}{L_y}\right) \quad (\text{A.9})$$

$$v = -\frac{A\pi}{\beta L_y \rho_o H} \sin\left(\frac{\pi y}{L_y}\right) \quad (\text{A.10})$$

The momentum shallow water equations in two-dimensions can also be written as follows:

$$fu = -g \frac{\partial h}{\partial y} + \nu \left( \frac{\partial^2 v}{\partial x^2} + \frac{\partial^2 v}{\partial y^2} \right) \quad (\text{A.11})$$

$$-fv = -g \frac{\partial h}{\partial x} + \nu \left( \frac{\partial^2 u}{\partial x^2} + \frac{\partial^2 u}{\partial y^2} \right) - A \cos\left(\frac{\pi y}{L_y}\right) \quad (\text{A.12})$$

where  $h(x, y)$  is the free surface elevation. The substitution of the Equations (A.9),(A.10) into (A.11),(A.12) gives the following:

$$h_{int}(x, y) = \frac{Af\pi}{g\beta L_y \rho_o H} (L_x - x) \sin\left(\frac{\pi y}{L_y}\right) - \frac{A\nu\pi^2}{g\beta L_y^2 \rho_o H} \cos\left(\frac{\pi y}{L_y}\right) + C_1 \quad (\text{A.13})$$

where  $C_1$  is an unknown constant, and multiplying by the gravitational acceleration  $g$ , gives the geopotential height solution:

$$\phi_{int}(x, y) = \frac{Af\pi}{\beta L_y \rho_o H} (L_x - x) \sin\left(\frac{\pi y}{L_y}\right) - \frac{A\nu\pi^2}{\beta L_y^2 \rho_o H} \cos\left(\frac{\pi y}{L_y}\right) + gC_1 \quad (\text{A.14})$$

### *ii. Western Boundary Layer (WBL) Solution*

The equation

$$\beta \frac{\partial \Psi}{\partial x} = \nu \nabla_H^4 \Psi$$

since ( $L_m \ll L_x$ ), it can be written as follows:

$$\beta \frac{\partial \Psi}{\partial x} = \nu \left( \frac{\partial^4 \Psi}{\partial x^4} \right)$$

and the substitution of  $\Psi(x, y) = \hat{\Psi}(x) \sin\left(\frac{\pi y}{L_y}\right)$  gives

$$\beta \frac{\partial \hat{\Psi}(x)}{\partial x} = \nu \frac{\partial^4 \hat{\Psi}(x)}{\partial x^4}$$

The solutions of the above equation are of the form

$$\hat{\Psi}(x) = c_1 e^{\lambda_1 x} + c_2 e^{\lambda_2 x} + c_3 e^{\lambda_3 x} + c_4 e^{\lambda_4 x}$$

where the  $\lambda$ 's are the roots of the characteristic equation

$$\beta \lambda = \nu \lambda^4$$

This equation gives the following roots:

$$\lambda_1 = 0$$

$$\lambda_2 = \left(\frac{\beta}{\nu}\right)^{\frac{1}{3}} = \frac{1}{L_M}$$

$$\lambda_3 = \left(\frac{\beta}{\nu}\right)^{\frac{1}{3}} \left[ -\frac{1}{2} + \frac{\sqrt{3}}{2}i \right] = \frac{-1+\sqrt{3}i}{2L_m}$$

$$\lambda_4 = \left(\frac{\beta}{\nu}\right)^{\frac{1}{3}} \left[ -\frac{1}{2} - \frac{\sqrt{3}}{2}i \right] = \frac{-1-\sqrt{3}i}{2L_m}$$

Since the WBL solution cannot grow exponentially, it must be that  $c_2 = 0$ , and the three remaining unknowns  $c_1$ ,  $c_3$ , and  $c_4$  can be evaluated by using the following conditions:

$$(1) \quad \Psi|_{x=0} = 0 \Rightarrow \hat{\Psi}|_{x=0} = 0$$

$$(2) \quad v|_{x=0} = 0 \Rightarrow \frac{\partial \Psi}{\partial x}|_{x=0} = 0 \Rightarrow \frac{\partial \hat{\Psi}}{\partial x}|_{x=0} = 0$$

(3) at distance  $L_m$  the two solutions (WBL and interior) must be the same

The use of the above three conditions gives the following:

$$\hat{\Psi}(x) = \frac{A\pi L_x}{\beta L_y} \left[ 1 - e^{-\frac{x}{2L_m}} \left( \cos \frac{\sqrt{3}x}{2L_m} + \frac{1}{\sqrt{3}} \sin \frac{\sqrt{3}x}{2L_m} \right) \right]$$

Thus, at the WBL,  $0 \leq x \leq L_m$  and  $0 \leq y \leq L_y$ , the streamfunction solution can be written as

$$\Psi(x, y) = \frac{A\pi L_x}{\beta L_y} \left[ 1 - e^{-\frac{x}{2L_m}} \left( \cos \frac{\sqrt{3}x}{2L_m} + \frac{1}{\sqrt{3}} \sin \frac{\sqrt{3}x}{2L_m} \right) \right] \sin \left( \frac{\pi y}{L_y} \right) \quad (\text{A.15})$$

As for the interior solution, the use of Equation (A.15) and Equations (A.5) and (A.6) of the streamfunction's definition gives the following:

$$u = \frac{A\pi^2 L_x}{\rho_o H \beta L_y^2} \left( -1 + e^{-\frac{x}{2L_m}} \left( \cos \frac{\sqrt{3}x}{2L_m} + \frac{\sqrt{3}}{3} \sin \frac{\sqrt{3}x}{2L_m} \right) \right) \cos \left( \frac{\pi y}{L_y} \right) \quad (\text{A.16})$$

$$v = \frac{2\sqrt{3} A\pi L_x}{3\rho_o H \beta L_y L_m} e^{-\frac{x}{2L_m}} \sin \frac{\sqrt{3}x}{2L_m} \sin \left( \frac{\pi y}{L_y} \right) \quad (\text{A.17})$$

With the same way as for the interior solution, the substitution of the Equations (A.16),(A.17) into (A.11),(A.12) gives

$$h_{wbl}(x, y) = \frac{A\pi f L_x}{g\beta L_y \rho_o H} \left[ 1 - \frac{\sqrt{3}}{3} e^{-\frac{x}{2L_m}} \left( \sin \frac{\sqrt{3}x}{2L_m} + \sqrt{3} \cos \frac{\sqrt{3}x}{2L_m} \right) \right] \sin \frac{\pi y}{L_y} + \frac{A\nu L_x}{g\beta \rho_o H} \left[ \left( \frac{2\sqrt{3}\pi^2}{3L_y^2 L_m} + \frac{\sqrt{3}}{3L_m^3} \right) \sin \frac{\sqrt{3}x}{2L_m} + \frac{1}{L_m^3} \cos \frac{\sqrt{3}x}{2L_m} \right] e^{-\frac{x}{2L_m}} \cos \frac{\pi y}{L_y} + C_2 \quad (\text{A.18})$$

where  $C_2$  is an unknown constant, and multiplying by the gravitational acceleration  $g$  gives the geopotential height solution:

$$\phi_{wbl}(x, y) = \frac{A\pi f L_x}{\beta L_y \rho_o H} \left[ 1 - \frac{\sqrt{3}}{3} e^{-\frac{x}{2L_m}} \left( \sin \frac{\sqrt{3}x}{2L_m} + \sqrt{3} \cos \frac{\sqrt{3}x}{2L_m} \right) \right] \sin \frac{\pi y}{L_y} + \frac{A\nu L_x}{\beta \rho_o H} \left[ \left( \frac{2\sqrt{3}\pi^2}{3L_y^2 L_m} + \frac{\sqrt{3}}{3L_m^3} \right) \sin \frac{\sqrt{3}x}{2L_m} + \frac{1}{L_m^3} \cos \frac{\sqrt{3}x}{2L_m} \right] e^{-\frac{x}{2L_m}} \cos \frac{\pi y}{L_y} + gC_2 \quad (\text{A.19})$$

THIS PAGE INTENTIONALLY LEFT BLANK

## LIST OF REFERENCES

- [1] International Federation of Red Cross and Red Crescent Societies, *World Disasters Report*, Kumarian Press, 2005.
- [2] S. Harig, C. Chaeroni, W. S. Pranowo, and J. Behrens, "Tsunami simulations on several scales; Comparison of approaches with unstructured meshes and nested grids", *Ocean Dynamics*, vol. 58, pp. 429-440, 2008.
- [3] E. L. Geist, V. Titov, D. Arcas, F. F. Pollitz, and S. L. Bilek, "Implications of the 26 December 2004 Sumatra-Andaman earthquake on tsunami forecast and assessment models for great subduction zone earthquakes, *Bulletin of the Seismological Society of America*, vol. 97, pp. 249-270, 2007.
- [4] V. Titov, A. B. Rabinovich, H. O. Mofjeld, R. E. Thomson, and F. I. Gonzalez, "The global reach of the December 2004 Sumatra tsunami", *Science*, vol. 309, pp. 2045-2048, 2005.
- [5] S. T. Grilli, M. Ioualalen, J. Asavanant, F. Shi, J. T. Kirby, M. Asce, and Ph. Watts, "Source constraints and model simulation of the 26 December, 2004, Indian Ocean Tsunami", *Journal of Waterway, Port, Coastal and Ocean Engineering*, vol. 133, pp. 414-428, 2007.
- [6] F. X. Giraldo and T. Warburton, "A high-order triangular discontinuous Galerkin oceanic shallow water model", *International Journal for Numerical Methods in Fluids*, vol. 56, pp. 899-925, 2008.
- [7] D. Schwanenberg and J. Kongeter, "A discontinuous Galerkin method for the shallow water equations with source terms". In *Discontinuous Galerkin Methods*, B. Cockburn, G.E. Karniadakis, C.W. Shu (eds.), *Heidelberg: Springer*, 2000, pp. 289-309.
- [8] H. Li and R. X. Liu, "The discontinuous Galerkin finite element method for the 2D shallow water equations", *Mathematics and Computer in Simulation*, vol. 56, pp. 171-184, 2001.
- [9] V. Ainzinger and C. Dawson, "A discontinuous Galerkin method for two-dimensional flow and transport in shallow water equations", *Advances in Water Resources*, vol. 25, pp. 67-84, 2002.
- [10] F. Dupont and C. A. Lin, "The adaptive spectral element method and comparisons with more traditional formulations for ocean modeling", *Journal of Atmospheric and Oceanic Technology*, vol. 21, pp. 135-147, 2004.

- [11] C. Eskilsson and S. J. Sherwin, "A triangular spectral / hp discontinuous Galerkin method for modeling 2D shallow water equations", *International Journal for Numerical Methods in Fluids*, vol. 45, pp. 605-623, 2004.
- [12] J. F. Remacle, S. S. Frazao, X. G. Li, and M.S. Shephard, "An adaptive discretization of shallow-water equations based on discontinuous Galerkin methods", *International Journal for Numerical Methods in Fluids*, vol. 52, pp. 903-923, 2006.
- [13] E. J. Kubatko, J. J. Westerink, and C. Dawson, "hp discontinuous Galerkin methods for advection dominated problems in shallow water flow", *Computer Methods in Applied Mechanics and Engineering*, vol. 196, pp. 437-451, 2006.
- [14] F. X. Giraldo, J. S. Hesthaven, and T. Warburton, "Nodal high-order discontinuous Galerkin methods for the spherical shallow water equations", *Journal of Computational Physics*, vol. 181, pp. 499-525, 2002.
- [15] F. X. Giraldo, "High-order triangle-based discontinuous Galerkin methods for hyperbolic equations on a rotating sphere", *Journal of Computational Physics*, vol. 214, pp. 447-465, 2006.
- [16] V. Titov and F. I. Gonzalez, "Implementation and testing of the method of splitting tsunami (MOST) model", *NOAA Technical Memorandum ERL PMEL-112*, 1997.
- [17] Z. Kowalik, W. Knight, T. Logan, and P. Whitmore, "Numerical Modeling of the Global Tsunami: Indonesian tsunami of 26 December 2004", *Science of Tsunami Hazards*, vol. 23, pp. 40-56, 2005.
- [18] Y. Okada, "Surface deformation due to shear and tensile faults in a half space", *Bulletin of the Seismological Society of America*, vol. 75, pp. 1135-1154, 1985.
- [19] L. H. Kantha and C. A. Clayson, "Numerical Models of Oceans and Oceanic Processes", *International Geophysics Series*, vol. 66, pp. 80-81, 2000.
- [20] J. R. Shewchuk, "Triangle: Engineering a 2d quality mesh generator and delaunay triangulator", *Applied Computational Geometry: Towards Geometric Engineering*, pp. 203-222, 1996.
- [21] R. Pawlowicz, "m\_map A Mapping package for Matlab", University of British Columbia Earth and Ocean Sciences. [Online]. Available: <http://www.eos.ubc.ca/rich/map.html>. [Accessed: 01-05-2009].
- [22] A. B. Rabinovich and R. E. Thomson, "The 26 December 2004 Sumatra Tsunami: Analysis of Tide Gauge Data from the World Ocean Part 1. Indian Ocean and South Africa", *Pure and Applied Geophysics*, vol. 164, pp. 261-308, 2007.

- [23] Survey of India and National Institute of Oceanography, "Tide-gauge observations of the 2004 Indian Ocean tsunami", National Institute of Oceanography. [Online]. Available: <http://www.nio.org/datainfo/tidegauge.htm>. [Accessed: 01-05-2009].
- [24] B. Nagarajan, I. Suresh, D. Sundar, R. Sharma, A. K. Lal, S. Neetu, S. S. C. Shennoi, S. R. Shetye, and D. Shankar, "The great tsunami of 26 December 2004: A description based on tide gauge data from Indian subcontinent and surrounding areas", *Earth Planets Space*, vol. 58, pp. 211-215, 2006.
- [25] University of Hawaii Sea Level Center - Global Sea Level Observing System, University of Hawaii. [Online]. Available: <http://uhslc.soest.hawaii.edu/>. [Accessed: 01-05-2009].
- [26] Y. Hayashi, "Extracting the 2004 Indian Ocean tsunami signals from sea surface height data observed by satellite altimetry", *Journal of Geophysical Research*, vol. 113, pp. 1001, 2008.
- [27] NOAA, "Tsunami event - December 26, 2004 Indonesia (Sumatra)", National Oceanic and Atmospheric Administration. [Online] Available: <http://nctr.pmel.noaa.gov/indo1204.html>. [Accessed: 01-05-2009].
- [28] T. Siffer, "Mercator depth gauge recording of 26 December 2004 tsunami", *KNMI (Royal Netherlands Meteorological Institute)*. [Online]. Available: <http://www.knmi.nl>. [Accessed: 01-05-2009].
- [29] R. Pawlowicz, B. Beardsley, and S. Lentz, "Classical tidal harmonic analysis including error estimates in MATLAB using *t\_tide*", *Computers and Geosciences*, vol. 28, pp. 929-937, 2002.
- [30] R. Pawlowicz, "*t\_tide* Harmonic Analysis Toolbox", University of British Columbia Earth and Ocean Sciences [Online] Available: <http://www.eos.ubc.ca/rich/ttide.html>. [Accessed: 01-05-2009].
- [31] S. T. Grilli, M. Ioualalen, J. Asavanant, F. Shi, J. T. Kirby, and P. Watts, "Source constrains and model simulation of the December 26, 2004 Indian Ocean tsunami", *Journal of Waterways, Port, Ocean and Coastal Engineering*, vol. 133, pp. 414-428, 2007.

THIS PAGE INTENTIONALLY LEFT BLANK

## **INITIAL DISTRIBUTION LIST**

1. Defense Technical Information Center  
Fort Belvoir, Virginia
2. Dudley Knox Library  
Naval Postgraduate School  
Monterey, California
3. Professor Francis X. Giraldo, Co-Advisor  
Associate Professor and Associate Chair for Research  
Department of Applied Mathematics  
Naval Postgraduate School  
Monterey, California
4. Professor Timour Radko, Co-Advisor  
Associate Professor  
Department of Oceanography  
Naval Postgraduate School  
Monterey, California
5. U.S. Naval Research Laboratory,  
Stennis Space Center, MS
6. Alfred-Wegener Institute,  
Bremerhaven, Germany
7. Randall J. Le Veque,  
University of Washington, Seattle